

Fabian Camillo Eitzen

# Investigation of a Francis turbine during start-stop

Master's thesis in Produktutvikling og produksjon

Supervisor: Chirag Trivedi

June 2022



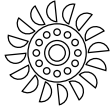
Fabian Camillo Eitzen

# **Investigation of a Francis turbine during start-stop**

Master's thesis in Produktutvikling og produksjon  
Supervisor: Chirag Trivedi  
June 2022

Norwegian University of Science and Technology  
Faculty of Engineering  
Department of Energy and Process Engineering





---

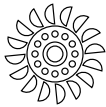
## Abstract

A numerical study of a Francis turbine during off-design operation has been conducted investigating the blade loading caused by turbulence phenomena near interfaces and pressure pulsations. The aim of the present work was to identify vortex development and flow dynamics in the stator, runner blade channel and draft tube inlet during simulation of a complete shutdown sequence. In recent years, turbines are more often used under varying operating conditions and start-stop operations. This leads to challenges in terms of turbine lifetime, cost, maintenance, and safety.

The investigation was made using computational fluid dynamics with a simplified three-dimensional scale model of a Francis turbine. A continuous simulation of a shutdown from Best Efficiency Point to Minimum Load was performed using a dynamic mesh for the stator system. To ensure numerical accuracy when using dynamic mesh, a Python-based automatic remeshing system was developed. The turbulence model selected was the Scale-Adaptive Simulation of the Shear Stress Transport  $k-\omega$  model with sufficiently refined mesh to be able to analyse the vortical structures in the flow field.

The results showed periodic vortex structures entering the blade channel causing dynamic pressure loads on the blades close to runner inlet during the first part of shutdown. At the end of the shutdown, the periodic vortex structures decayed while large stochastic vortical structures appeared around main blades trailing edge. Additional stochastic vortices were formed at runner inlet on pressure side due to flow separation at Minimum Load. Results in the draft tube showed that the rotating vortex rope propagates upstream along runner cone as a result of recirculation pockets on the runner cone side. These recirculation pockets are formed due to production of flow gates underneath the runner cone and the results indicate a strong correlation between the flow gate and the formation of the rotating vortex rope.

Overall, the findings in the present work implies that in the first phase, a low level oscillating pressure force acts on the upper part of the blades. During the final stage, large stochastic pressure forces act on the lower part. Loads are greatest at the trailing edge, where the blades are thinnest. Therefore, it was be concluded that blade loading will eventually cause fatigue damage after a certain number of shutdowns, and failure will most likely occur at the runner blades trailing edge before the leading edge.



---

## Sammendrag

En numerisk studie av en Francis-turbin under off-design drift har blitt utført for å undersøke bladbelastningen forårsaket av turbulensfenomener nært grensesnitt og trykkpulseringer. Målet med arbeidet var å identifisere virvelutvikling og strømningsdynamikk i ladeapparatet, skovl kanalen og innløpet av sugerør under simulering av en komplett avslutningssekvens. De siste årene brukes turbiner oftere under varierende driftsforhold og start-stoppoperasjoner. Dette fører til utfordringer når det gjelder turbinlevetid, kostnader, vedlikehold og sikkerhet.

Undersøkelsen ble gjort ved hjelp av numerisk strømningsanalyse med en forenklet tredimensjonal skala modell av en Francis turbin. En kontinuerlig simulering av en avslutning fra Beste effektivitetspunkt til Minimumsbelastning ble utført ved hjelp av dynamisk bevegelse av ladeapparatet. For å sikre tilstrekkelig numerisk nøyaktighet er det laget et automatisert system ved hjelp av Python koder for å generere nytt diskritiseringsdomene for ledeskovlene. Turbulensmodellen som er benyttet er Scale-Adaptive Simulation av den tidligere Shear Stress Transport  $k-\omega$ -modellen med tilstrekkelig diskritiseringsoppløsning for å kunne analysere virvel strukturene i strømningsfeltet.

Resultatene viste periodiske virvelstrukturer som kom inn i skovlkanalen og forårsaket dynamiske trykkbelastninger på bladene nær løpehjulinntaket under den første delen av avstengningen. På slutten av nedstengningen avtok de periodiske virvelstrukturene, mens store stokastiske virvelstrukturer dukket opp rundt hovedskovlenes forkant. Ytterligere stokastiske virvler ble dannet ved løpehjulsinntaket på trykksiden på grunn av strømningsseparasjon ved minimumsbelastning. Resultater i sugerøret viser at det roterende virvel strukturen forplanter seg oppstrøms som følge av resirkuleringslommer på siden av løpehjulskjeglen. Disse resirkuleringslommene dannes på grunn

av produksjon av strømningsgater under løpehjulskjeglen, og resultatene indikerer en sterk sammenheng mellom strømningsgaten og formen på det roterende virvelen.

Samlet sett innebærer funnene i det nåværende arbeidet at i første fase virker et lavnivå og oscillerende trykkbelastning på den øvre delen av skovlene. Mens det i slutfasen virker store stokastiske trykkrefter på den nedre delen av hovedskovlene. Lastene er størst på den bakre kanten, hvor bladet er tynneste. Derfor ble det konkludert med at skovl belastningen til slutt vil forårsake tretthetsbrudd etter et visst antall avstengninger, og bruddpunktet vil mest sannsynlig oppstå ved skovlenes bakkant.



---

## **Acknowledgments**

This work was done at the Waterpower Laboratory, Department of Energy and Process Engineering at Norwegian University of Science and Technology (NTNU) in Trondheim during fall of 2022.

I would like to give my sincere thank you to my supervisor Chirag Trivedi for guiding me through the thesis work in the field of research on dynamic simulations on a Francis turbine. To be able to develop knowledge and experience with computational fluid dynamics, hydraulic turbo machinery and work strategies which I can apply in future work. I would also like to express my gratitude to NTNU HPC Group for the access to IDUN computing cluster during the work and for all the support.

At last, I would like to thank all my fellow students for their motivation and help at the Waterpower Laboratory.



---

# Contents

<b>Abstract</b>	<b>i</b>
<b>Sammendrag</b>	<b>iii</b>
<b>Acknowledgment</b>	<b>i</b>
<b>Contents</b>	<b>v</b>
<b>List of tables</b>	<b>vii</b>
<b>List of figures</b>	<b>xii</b>
<b>Nomenclature</b>	<b>xiii</b>
<b>1 Introduction</b>	<b>1</b>
1.1 Background . . . . .	1
1.2 Case description . . . . .	2
1.3 The objective . . . . .	4
1.4 Referencing . . . . .	4
<b>2 Literature review</b>	<b>5</b>

<b>3</b>	<b>Theory</b>	<b>11</b>
3.1	Vorticity and vortex dynamics . . . . .	11
3.2	Rotor stator interaction . . . . .	16
3.3	Mathematical foundation . . . . .	19
<b>4</b>	<b>Numerical methodology</b>	<b>25</b>
4.1	Case overview . . . . .	25
4.2	Mesh overview . . . . .	30
4.3	Verification . . . . .	32
4.4	Validation . . . . .	33
4.5	Computational setup . . . . .	35
<b>5</b>	<b>Remesh architecture</b>	<b>39</b>
5.1	Mesh motion strategy . . . . .	39
5.2	Dynamic mesh . . . . .	40
5.3	Automated remeshing . . . . .	41
5.4	Remesh interpolation . . . . .	42
<b>6</b>	<b>Results and discussions</b>	<b>45</b>
6.1	Dynamic pressure loading . . . . .	45
6.2	Vortex development and dynamics: Stator . . . . .	49
6.3	Vortex development and dynamics: Rotor . . . . .	52
6.4	Vortex development and dynamics: Draft Tube . . . . .	60
<b>7</b>	<b>Conclusions</b>	<b>67</b>
<b>8</b>	<b>Future work</b>	<b>69</b>
	<b>References</b>	<b>71</b>

<b>A</b>	<b>Appendix A</b>	<b>77</b>
<b>B</b>	<b>Appendix B – Overview of monitor point locations</b>	<b>79</b>
<b>C</b>	<b>Appendix C – Mesh and interface setup</b>	<b>83</b>
<b>D</b>	<b>Appendix D – Remesh script</b>	<b>93</b>
	D.1 - Geometry Modification Script . . . . .	93
	D.2 - Mesh Replay Script . . . . .	95
<b>E</b>	<b>Appendix E – Results</b>	<b>103</b>
	E.1 Vortex Structures . . . . .	103
	E.2 Velocity Contour - Draft Tube . . . . .	103
<b>F</b>	<b>Appendix F - Master agreement</b>	<b>111</b>



---

## List of tables

4.1	Operating conditions from experiments conducted in workshop 2 [1]. . . . .	26
4.2	Mesh statistics and quality at BEP . . . . .	30
4.3	Mesh $y^+$ values measured at BEP . . . . .	31
4.4	Grid convergence index study of discretization error for stator and rotor domains. . . . .	33
4.5	Validation of pressure and turbine performance at BEP . . . .	34
B.1	Monitor point and velocity line coordinates . . . . .	79





---

## List of figures

1.1	Model geometry of the Francis turbine system at Waterpower Laboratory at NTNU. . . . .	3
1.2	Section view of spiral casing with 14 stay vanes, stay ring with 28 guide vanes and runner with 15 main blades and 15 splitter blades. . . . .	4
2.1	Program architecture for remeshing [2] . . . . .	6
2.2	Vector velocity field from case study. (a) SA, (b) SARC, (c) SA DES, (d) $\kappa - \omega$ SST DES . . . . .	8
3.1	Sketch of boundary layer with profiles of (a) Velocity and (b) Vorticity. . . . .	12
3.2	2D sketch of blade tip vortex caused by free shear layer and Kelvin-Helmholtz instabilities. Note, the illustration is exaggerated. . . . .	13
3.3	Illustration of a single structured horseshoe vortex at blade leading edge. . . . .	13
3.4	Horseshoe vortex structure for different leading edge radii [3].	14
3.5	Secondary flow structures in a blade channel [4]. . . . .	15
3.6	Illustration of 1st and 2nd harmonics of fluctuating pressure field from four runner blades. . . . .	17

3.7	Energy cascade for turbulent kinetic energy as a function of wave length, $\lambda$ . . . . .	20
4.1	Guide vane angle (left) and volume flow rate (right) based on experimental setup in workshop 2 . . . . .	26
4.2	Overview of monitor point position in stator domain. . . . .	27
4.3	Solution output frequency time line shown by red lines. Shaded regions in light green shows possible time for remeshing. . . . .	27
4.4	Overview of stator domain with guide vanes and rotor domain with main blades and splitter blades of the Francis-99 used in the present work. . . . .	28
4.5	Three dimensional model of the Francis-99 used in the present work. . . . .	29
4.6	Progress of Orthogonal Angle during simulation with and without remeshing. . . . .	31
4.7	Numerical validation of horizontal ( $\tilde{U}$ ) and axial ( $\tilde{V}$ ) velocity components against experimental PIV measurements at BEP. . . . .	35
5.1	System architecture for automatic remeshing with ANSYS CFX <sup>®</sup> and ICEM CFD <sup>™</sup> . . . . .	41
5.2	Orthogonality Progress during full shutdown simulation . . . . .	42
5.3	Three locations at upper and lower ring with reduced orthogonal quality during dynamic mesh motion. . . . .	43
6.1	Pressure Gradient on Main Blade for all operating points. . . . .	47
6.2	Pressure Gradient on Splitter Blade for all operating points. . . . .	48
6.3	Streamlines of HSV near GV LE at BEP. . . . .	50
6.4	Dominant vortex structures from guide vanes in the vaneless space. . . . .	51
6.5	Dynamics of horizontal vortex structures from guide vane passage vortex, on 95% of blade span at BEP. . . . .	53
6.6	Dynamics of vertical vortex structures from guide vane vortex shedding, on 50% of blade span at BEP. . . . .	54

6.7	Time development of runner blade stagnation point with streamlines showing flow path at each operating points. (a) best efficiency point, (b) part load, (c) deep part load, (d) minimum load and, (e) total time overview. . . . .	56
6.8	Pressure gradient around main blade trailing edge at ML with pressure isolines, on 5% blade span. . . . .	58
6.9	Flow condition near main blade trailing edge at ML. Here $c_1$ is the absolute runner outlet velocity, $c_{u1}$ is the whirl velocity component and $c_{m1}$ is the axial component. . . . .	59
6.10	Overview of flow separation on main blade and splitter blade leading edge at ML. . . . .	60
6.11	Frequency analysis of monitor point, DTF1, in draft tube by the use of spectrogram during the entire shutdown sequence. . . . .	61
6.12	Rotating vortex rope in the draft tube at PL. . . . .	62
6.13	Comparison of flow condition around the runner cone for different timestamps . . . . .	63
6.14	Unsymmetrical RVR observed at $t = 2.0$ s showing one recirculation pocket on runner cone side. . . . .	64
B.1	Overview of monitor point position in rotor domain. . . . .	80
B.2	Overview of monitor point position in draft tube domain. . . . .	81
C.1	Guide vane passage mesh and mesh interface. . . . .	83
C.2	Guide vane trailing edge before remeshing at BEP. . . . .	84
C.3	Guide vane Mesh. . . . .	85
C.4	Runner main blade and splitter blade mesh. . . . .	85
C.5	Runner passage mesh. . . . .	86
C.6	Draft tube mesh. . . . .	87
C.7	Close up of runner cone mesh. . . . .	88
C.8	Draft tube inlet mesh. . . . .	89
C.9	Draft tube outlet mesh. . . . .	90

C.10	Overview of interface models used in simulation setup . . . . .	91
D.1	Mesh Replay Script - Continuation . . . . .	96
D.2	Mesh Replay Script - Continuation . . . . .	97
D.3	Mesh Replay Script - Continuation . . . . .	98
D.4	Mesh Replay Script - Continuation . . . . .	99
D.5	Mesh Replay Script - Continuation . . . . .	100
D.6	Mesh Replay Script - Continuation . . . . .	101
E.1	Primary and secondary vortex pairs along main blade suction side at BEP. . . . .	103
E.2	Horizontal vortex structures between main and splitter blade, along Hub at BEP. . . . .	104
E.3	Guide vane Passage vortex and vortex shedding at BEP. . . . .	105
E.4	Runner Passage vortex with near mid span merging found at PL. . . . .	106
E.5	Runner main blade spiral vortex and stationary vortices found at DPL. . . . .	107
E.6	Local vortices interacting with Horseshoe vortex at runner blades leading edge near Shroud, found at ML. . . . .	108
E.7	Velocity field in draft tube after 1 second of shutdown showing vortex shedding pattern from runner blades. . . . .	109
E.8	Velocity field in draft tube after 2 second of shutdown showing vortex shedding pattern from runner blades. . . . .	110

---

## Nomenclature

### Abbreviation

BEP	Best efficiency point
CFD	Computational fluid dynamic
DT	Draft tube
DES	Detached eddy simulation
DPL	Deep part load
DNS	Direct numerical simulation
FFT	Fast Fourier transform
FSI	Fluid structure interaction
GGI	General Grid Interface
GCI	Grid convergence index
GV	Guide vane
HSV	Horseshoe vortex
LE	Leading edge
LES	Large eddy simulation
ML	Minimum load
MB	Main blade

NTNU	Norwegian University of Science and Technology
PL	Part load
RN	Runner
RVR	Rotating vortex rope
RSM	Reynolds stress model
RANS	Reynolds-averaged Navier-Stokes equation
SAS	Scale adaptive simulation
SA	Spalart-Allmaras
STFT	Short-time Fourier transform
ST	Stay vane
SST	Shear stress transport
SB	Splitter blade
SRS	Scale resolved simulation
TE	Trailing edge
URANS	Unsteady Reynolds-Averaged Navier-Stokes equation

**Latin symbols**

$c$	Chord length (m)
$D_{r1}$	Runner inlet diameter (m)
$D_{r2}$	Runner outlet diameter (m)
$d$	Boundary distance
$E$	Specific hydraulic energy ( $\text{J kg}^{-1}$ ), $E = gH$
$f$	Frequency (Hz)
$f_r$	Runner passing frequency (Hz)
$f_s$	Guide vane passing frequency (Hz)
$g$	Gravity acceleration ( $\text{m s}^{-2}$ )

$H$	Head (m)
$k$	Turbulent kinetic energy ( $\text{m}^2 \text{s}^{-2}$ )
$l$	Length (m)
$L$	Blade pitch (m), $L = \pi D_{r1}/z_r$
$n$	Runner angular speed ( $\text{s}^{-1}$ )
$p$	Pressure (Pa)
$\tilde{p}_E$	Factor of pressure fluctuation, $\tilde{p}_E = \tilde{p}/(\rho E)$
$Q$	Flow rate ( $\text{m}^3 \text{s}^{-1}$ )
$R_{G1}$	Guide vane leading edge radius (m)
R	Residual
$T$	Torque (N m)
$t$	Time (s)
$u_\tau$	Frictional velocity ( $\text{m s}^{-1}$ )
$u'$	Time-varying fluctuating component of velocity ( $\text{m s}^{-1}$ )
$\tilde{U}$	Horizontal velocity component in PIV plane ( $\text{m s}^{-1}$ )
$\tilde{V}$	Axial velocity component in PIV plane ( $\text{m s}^{-1}$ )
$\mathcal{V}$	Cell element volume ( $\text{m}^3$ )
$\forall$	Local control volume ( $\text{m}^3$ )
$y$	Absolute distance (m)
$z_r$	Number of runner blades
$z_s$	Number of stator blades

### Greek symbols

$\alpha$	Guide vane angle ( $^\circ$ )
$\beta$	Blade angle ( $^\circ$ )
$\delta$	Boundary layer thickness (m)

$\Delta$	Cell element size (m)
$\eta$	Efficiency
$\epsilon$	Rate of dissipation of turbulent kinetic energy ( $\text{m}^2 \text{s}^{-3}$ )
$\lambda$	Wave length (m)
$\mu$	Dynamic viscosity (Pa s)
$\nu$	Kinematic viscosity (Pa s)
$\nu_t$	Eddy viscosity (Pa s)
$\Phi$	Phase angle (rad)
$\phi$	Central angle
$\rho$	Density ( $\text{m}^2 \text{s}^{-1}$ )
$\omega$	Angular speed ( $\text{rad s}^{-1}$ )

#### **Superscripts and subscripts**

1,2,...	Indices
ave	Average
disp	Displacement
dis	Distance
eq	Equivalent
i	Initial time
n	Previous time step
n+1	Current time step
ref	Reference
r	Rotor
rms	Root-mean-square
SAS	Scale-Adaptive Simulation
s	Stator
vol	Volume



## Introduction

### 1.1 Background

In recent years, increased intermittent renewable energy resources, such as wind and solar energy, is connected to the powergrid resulting in undesired power fluctuations. The power-electric market is therefore demanding more flexibility and stability to the powergrid. By use of hydraulic turbines, one can store energy through water reservoir and is seen as a controllable energy resource which can fulfill the demands within a wide range of time scales [5,6]. The turbines are therefore used more often under varying operational conditions. This leads to challenges within turbine lifetime, cost, maintenance and safety.

There are two classifications of turbine operations, namely steady and transient operations. Steady operations involves a fixed flow rate, runner speed and guide vane angle, whereas in transient operations, one or more of these are changing with time [7]. The Francis turbine is design to run in a specific steady operational condition, called best efficiency point (BEP). However, to meet the demand mentioned, turbines are more often operated in transient modes, also referred to as off-design operations [8]. Some examples to off-design operations are load acceptance, load rejections, startup and shutdown. With respect to startup and shutdown, the turbines are initially designed for 1-10 start-stop cycles per year [9]. This is estimated to increase up to 500 cycles each year to mitigate powergrid stabilisation [10]. Meaning, a wide range of transient operations has to be taken into account in future designs and turbine refurbishment.

There are three main area of concern regarding the Francis turbine, 1) the vaneless space between the guide vanes (stator) and the runner blades (rotor), 2) runner blade channel and 3) draft tube inlet area. In the vane-

less space, pressure pulsations from rotor stator interaction (RSI) propagates through the entire turbine with frequencies close to the runner natural frequency [8, 11]. This may induce resonance effects leading to unacceptable pressure amplitudes [8]. Especially for high head Francis turbine which have large number of blades and guide vanes with small gap between rotor and stator. The result is high RSI frequency amplitudes which influences the operating lifetime [11–13]. In a study by Trivedi et al. [14] shows that the angular speed of the guide vanes during transient events have significant effect on the pressure pulsations. Unsteady vortex shedding from the guide vanes in combinations with the pressure field from the runner blades leading edge, creates a complex flow in the vaneless space [13]. New pressure waves develops before the previous is dampened, creating high amplitude waves expected to propagate far upstream and downstream of the vaneless space [11].

During shutdown, the flow rate decreases while the runner angular speed is fixed, leading to strong boundary layer separation from the blade leading edge [13]. Secondary flow structures are generated, making the flow in the runner highly complex with deterministic and stochastic pressure pulsations leading to dynamic stresses on the blades [12].

## 1.2 Case description

The Waterpower Laboratory located at Norwegian University of Science and Technology (NTNU) in Norway is a well known hydraulic turbine laboratory and combines hundreds of years of experience. The laboratory have been an active role in research and development of hydraulic turbines since 1917. The Francis-99 is a series containing three workshops organized at NTNU. A turbine model in the scale of 1:5.1 of a Francis turbine have been produced, where the prototype turbine is located at Tokke power plant in Norway [15]. The full test rig configuration can be viewed from the Francis-99 website [1]. Workshop 1 was first organized back in December, 2014 and aims to run steady state operations.

The second workshop covers transient operations and was organized two years after the first workshop. The third and final one is a fluid structure interaction (FSI) study and was organized during May 2019. All workshops are related to the test model either through experiment or numerical simulations using CFD, and the main objective is to aid the hydraulic researches open access to experimental and numerical data to increase knowledge in

the field [1].

### 1.2.1 Model description

In this present study, the high-head Francis turbine model with the Francis-99 runner is used. The turbine model consist of a spiral casing with 14 stay vanes (ST), 28 guide vanes (GV), a runner (RN) with 15 blades and 15 splitter blades, and a draft tube (DT) which is connected to a downstream tank. The inlet and outlet diameters are  $D_{r1} = 0.648$  m and  $D_{r2} = 0.349$  m, respectively, and the net head of the model at best efficiency point is  $H = 12$  m [1]. See Fig. 1.1 of model geometry.

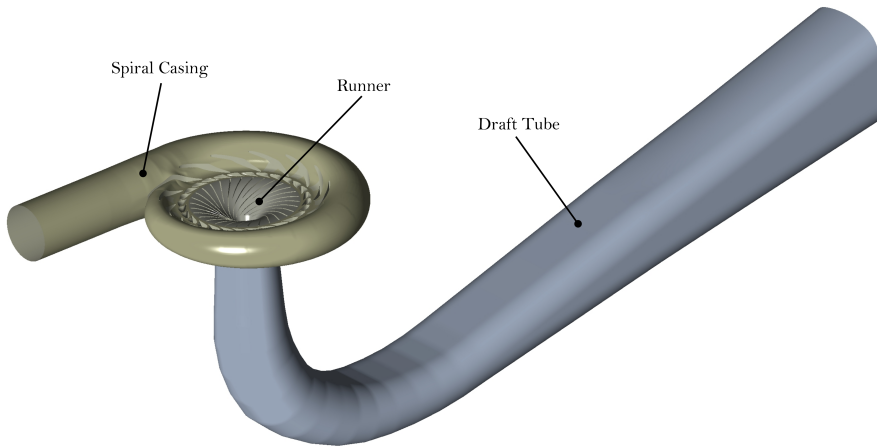


**Figure 1.1:** Model geometry of the Francis turbine system at Waterpower Laboratory at NTNU.

### 1.2.2 Available model and experimental data

The geometry of the entire system and experimental data was found on the Francis-99 website [1]. This data will be used to validate this present study. See section 4.3 and 4.4 for verification and validation, respectively.

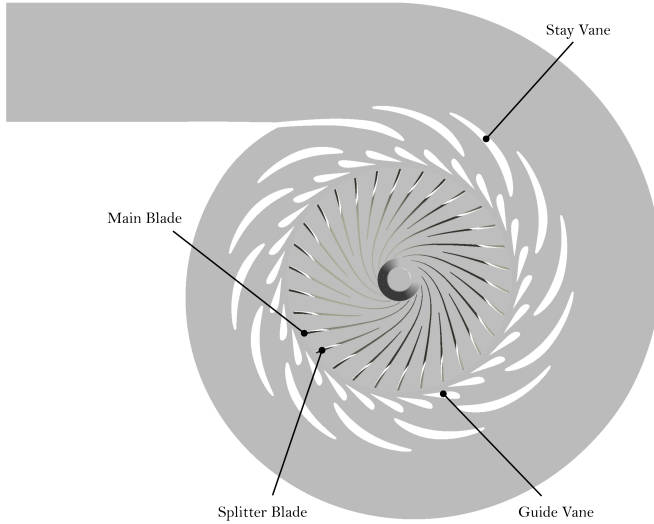


**Figure 1.2:** Section view of spiral casing with 14 stay vanes, stay ring with 28 guide vanes and runner with 15 main blades and 15 splitter blades.

### 1.3 The objective

A three dimensional Francis turbine model of with the Francis-99 runner is to be numerically investigated during start-stop operation using computational fluid dynamics (CFD). The objective is investigate the blade loading caused by turbulence phenomena near interfaces and pressure pulsations. The focus of this present work will be blade loading and vortex development and dynamics in the stator, runner blade channel and draft tube inlet under complete shutdown sequence from BEP to minimum load (ML).

The thesis limitations on completion are as follows; Available computational resources entails limited time and the use of complex turbulence method, e.i Large Eddy Simulation (LES) was not feasible.

### 1.4 Referencing

Part of Chapter 2 and 5, and Sec. 3.3, 4.2 and 4.5 is partly modified and reused from the previous project work during autumn 2021.

## Literature review

*The literature study conducted in the present work will be presented in this chapter. The software usage in the field of research of complex flows in Francis turbines have been mapped closely. In relations to transient operations of the Francis turbine such as shutdown, methods of dynamic mesh motion and remeshing have been studied and an overview is presented. Then, turbulence numerics and solution strategy was reviewed to find the appropriate method related to the purpose of the thesis. Finally, literatures on transient flow field in Francis turbines and related challenges regarding runner failures is presented.*

Mössinger et al. [16] and Salehi et al. [15] have both done transient CFD simulations on a Francis turbine during shutdown. In both cases, the Francis-99 test case were used. Salehi et al. [15] uses the open-source CFD code called OpenFOAM to solve the problem. Mössinger et al. [16] on the other side, uses the commercial program called ANSYS CFX<sup>®</sup>. However, both uses "in-house" programs in ANSYS<sup>®</sup> for meshing. Here, Salehi et al. [15] are more specific. They used ICEM CFD<sup>™</sup> for meshing of SC, DT and RN, and TurboGrid for meshing of GV. Using ICEM CFD<sup>™</sup> makes the user have full control of the grid creation. One other important aspect is the in-build function called replay script. This records the users input and store the commands in a Iron python script. It can then be used in a program architecture to automatically generate new mesh files to be replaced with dynamic meshes with reduced quality. In this way, one assures that the quality of the mesh is at an acceptable level throughout the simulation. This specific method is described in the research study by Unterluggauer et al. [2], and can be viewed in Fig. 2.1, and are briefly covered in the report by Mössinger et al. [16]. In these cases, some predetermined interruption

condition is specified which will initiate the solver to pause for remeshing and then the solver continues with the new mesh.

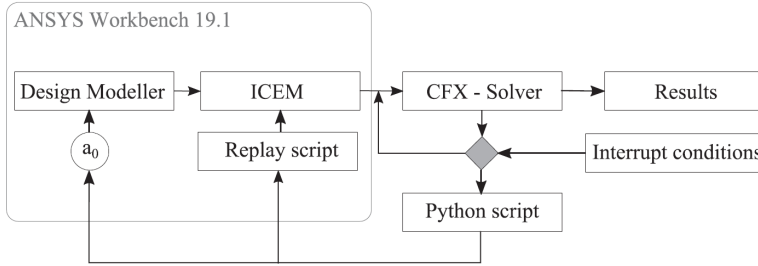


**Figure 2.1:** Program architecture for remeshing [2]

The method presented by Mössinger et al. [16] are as following: After a predetermined logical expression (interrupt condition in CFX) is true, the CFX solver is paused. Which interrupt condition that has been used is unclear, however, maximum runtime, minimum cell angle and maximum aspect ration is mentioned as examples. Then continues by mentioning that a new mesh, dependent on new values for the GV angle is created with the help of an in-house mesher. Comparing this method with the one presented by Unterluggauer et al. [2] one can witness some similarities, however, in the latter case the method is more described. From Fig 2.1 the CFX-Solver is connected to the Design Modeller which is connected to the ICEM CFD™. The solver pauses due to Interrupt conditions. Unterluggauer et al. [2] used minimum orthogonal angle ( $>12^\circ$ ) and average  $y^+$  ( $< 35$ ) as interrupt conditions. Then the Python scrip feeds the opening angle to Design Modeller which alters the geometry file. Then the ICEM CFD™ initiates remeshing by the use of a replay script. The whole process takes place inside ANSYS® Workbench 19.1 as can be seen from Fig. 2.1. The solver is given the new mesh-file and continues the cycle until it finishes.

A case study done by Giroux et al. [17] presents a similar method as the ones described above. However, instead of using a interrupt condition, the remeshing process updates the GV mesh after each time step. Giroux et al. [17] states that this takes up large amount of disk space which is the downside of using this method. To solve this, they had to use a additional companion script to clean up old mesh files.

Comparing the methods presented above, one can see that they have, to some degree, similar architecture. However, the method presented by

---

Unterluggauer et al. [2] is efficient and less complicated compared to the method presented by Giroux et al. [17]. This is likely to do with the time and available resources, as programs are becoming more advanced with time.

For the GV rotation, Mössinger et al. [16] states that this is doable through transient node motion. The ANSYS CFX<sup>®</sup> software has an in-built function called Mesh Deformation. This allows the user to specify translation and rotation to boundaries or sub domains. As the boundary is moving, the nodes in the grid will shift according to a Displacement Diffusion Equation and the nodes location will be updated at the start of each outer iterations or for each time step [16, 18]. See the report by Mössinger et al. [16] or the ANSYS<sup>®</sup> manual [18] for more information.

Using Mesh Deformations, the user have to determine a Mesh Stiffness method and constants defined by the selected method. Mössinger et al. [16] uses the Mesh Stiffness method called, **increase near small volumes**. This is a volume approach where the Mesh Stiffness is increased near small volumes where larger control volumes will absorb more of the motion. The method depends on the initial node distribution in the mesh. It is therefore important to have finer mesh in regions with significant motion [18]. The Mesh Stiffness is defined as a ratio between the reference volume and the control volume size, and a Model Exponent,  $C_{stiff}$  determines how abrupt the stiffness variation occurs. Mössinger et al. [16] selected a Model Exponent of 15 as this resulted in desirable mesh quality during GV movement. Unterluggauer et al. [2] uses the same method, however, the specified value for the Model Exponent is 8. Research done by Melot et al. [19], Dewan et al. [20] and Giroux et al. [17] uses mesh deformation during simulation. However, no methods or parameters are specified. Regardless of previous research, ANSYS<sup>®</sup> thoroughly covers the theory around various methods. Secondly, the variation in values selected for the Model Exponent will depend on the individual mesh. Therefore, a examination of proper value for the Model Exponent should be made during mesh verification study.

To accurately model the transient flow field inside the turbine, sophisticated turbulence models is needed. Minakov et al. [21] have done research on unsteady turbulent flow in a Francis turbine. From there, it was found that pressure pulsations are mainly caused by the precessing vortex rope downstream of the runner. Meaning, the dynamics of the vortex rope determines the pulsations characteristics during turbine operations. A study done by Trivedi et al. [14] found through experimental study of 6 different transient operations, the GV speed variations have great impact on the pressure fluctuations. It was also found that vortical flow structures leaving the GV and

into the vaneless space was observed, which affected the streamlined flow in the runner. Therefore, resolving the turbulent flow field is highly important to get accurate results. The majority of research on transient flow field inside the Francis turbine uses either Menter's Shear Stress Transport (SST) model of the  $\kappa - \omega$  or the SST based Scale-Adaptive Simulation (SAS-SST). Salehi et al. [15] states that the chosen SAS-SST turbulence model are commonly used for simulations of practical transient flows. Moreover, the turbulence model have successfully been tested and verified for the characteristic flow fields in hydraulic turbines and are applied in many industrial cases [15]. In a numerical study done by Trivedi et al. [22] carried out three different unsteady simulations using the standard  $\kappa - \epsilon$  and the  $\kappa - \omega$  SST model. Both turbulence models showed good agreement with experimental results at BEP, however, at operating points away from BEP, the models had difficulties in capturing the flow separation and other flow features. Additionally, the models also had difficulties in resolving the vortex breakdown in the draft tube which led to highest deviations compared to experimental results [22]. So is the RANS (Reynolds-averaged Navier-Stokes) equation models,  $\kappa - \epsilon$ ,  $\kappa - \omega$  or  $\kappa - \omega$  SST, sufficient models to accurately predict the flow structures during transient operations in the Francis turbine. Or is there other more appropriate models that should be used instead, such as a Detached Eddy Simulation (DES) method approach or LES.

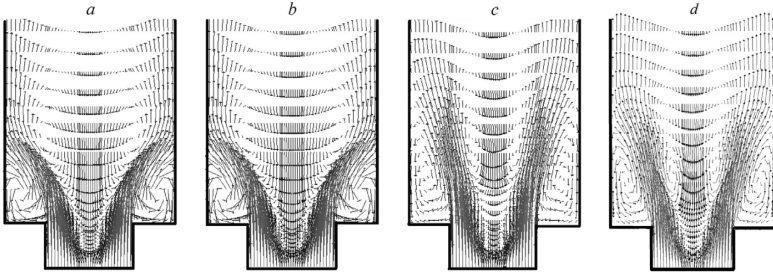


**Figure 2.2:** Vector velocity field from case study. (a) SA, (b) SARC, (c) SA DES, (d)  $\kappa - \omega$  SST DES

A numerical study on a Francis turbine with the use of both a Reynolds Stress Model (RSM) turbulence model and DES method based on  $\kappa - \omega$  SST, showed that the calculated flow field inside the draft tube was in close agreement with experimental data. Here, the averaged velocity components from RMS and DES simulations are rather similar. However, the RMS model underestimated the velocity pulsations in the draft tube during part load (PL) operations. The average velocity components in the bottom cross



---

section of the draft tube using DES method, agrees well with experimental results. Finally, both simulations underestimated the velocity pulsations in top cross section, where the authors concluded that this may be due to insufficiently fine mesh in the runner [23]. Another numerical study which had a integrated test case of strong swirling flow in a abrupt expansion casing, compared different turbulence models. This test case was in review of a numerical study of the Francis turbine. The Spalart Allmaras (SA), SARC model, SA DES and  $\kappa - \omega$  SST DES was investigated. The results from the case study are shown in Fig. 2.2. Figure 2.2(a) and Fig. 2.2(b) shows similar results and the recirculation pocket is not captured well compared to the results shown in Fig. 2.2(c) and Fig. 2.2(d). Here, the DES method gave longer recirculation zones in the axial direction as well as behind the back step, and by that, aids more accurate calculations compared to the RANS models [24]. One can also see that the magnitude of the velocity components downstream of the back step dissipates more rapidly with the RANS models compared to the DES models, which is a downside of using RANS. To put this in perspective, using a DES method to resolve the eddies produced by the GVs could be a more accurate way of solving the transients inside the Francis turbine. This is also one of the conclusions from this numerical study by Minakov et al. [24] where the final selected turbulence models used in the study was the DES models.

The study of transient effects on a Francis turbine runner life has been conducted by Trivedi [25]. As the turbine operates under off-design operating points, it was found that unsteady vortical flow structures develops from the guide vane passage and propagates into the vaneless space. Vortex breakdown, cavitation and high pressure pulsations is causing system vibrations leading to ware of the turbine runner. A recent study by Trivedi [12] of interaction between trailing edge wake and vortex rings in the Francis turbine during runaway conditions also states that vortex break downs and stochastic fluctuations are present inside the blade channel due to unsteady vortex flow during off-design operations.

The experimental study presented in Trivedi [25] showed that during shutdown, the vortex formation and dissipation occurs as the guide vanes moves, and by reducing the discharge, vortex instabilities increases. Additionally, as the guide vanes are closing, the tangential velocity component increases while reducing the discharge causing the flow to separate at the runner inlet. Furthermore, it was found that for small guide vane openings, the flow in the vaneless space stabilizes, blocking the flow at runner inlet. Additional observations during shutdown unveiled pressure pulsations with strength of up to 1.7 times normal operating pressure head, of which the tur-

bine system is not designed for. It is stated as well that mechanical stresses and fatigue failures due to cracks is reported by the manufactures due to asymmetric and dynamic forces on the upper part of the runner blades [25]. At last, it was pointed out dynamic effects of which should be considered further, which is guide vane movement, draft tube vortex and Rotor Stator Interaction.

---

## Chapter 3

---

### Theory

*This chapter presents the theoretical aspect of the present work. The first section covers the mathematical outline of vorticity and relevant aspects of vortex dynamics with vortex characteristic and types. Then, a section on Rotor Stator Interaction will provide mathematical and theoretical knowledge on discrete pressure fields and excitation frequencies. The chapter ends with a detailed presentation of the mathematics behind CFD and turbulence numerics with near wall modeling.*

#### 3.1 Vorticity and vortex dynamics

A vortex is commonly associated as a region of fluid rotating around a shared center line. It is defined by the vorticity,  $\vec{\omega}$ , which is a measure of the rotation of a fluid element moving in the flow field,  $\mathbf{u}$ , expressed by Eq. 3.1 [26].

$$\vec{\omega} = \nabla \times \mathbf{u} \tag{3.1}$$

A vorticity concentration of arbitrary shape takes the form of a layer-like or axial structure in one or two spatial dimensions, respectively. Boundary layer (attached vortex layer) and free shear layer (free vortex layer) are two examples of layer-like structures. The two structures are closely related as stages in the temporal evolution and/or in spatial positions of a single vortical structure, of which the axial structure being the strongest form [26].

From the Navier-Stokes Equations, the evolution equation can be derived for the fluids vorticity field as

$$\frac{D\vec{\omega}}{Dt} = \vec{\omega} \cdot \mathbf{u} + \nu \Delta \vec{\omega} \quad (3.2)$$

where  $D/Dt = \partial/\partial t + \mathbf{u} \cdot \nabla$  is the material derivative. The first term in Eq. 3.2 accounts for the vorticity to be transported by the fluid velocity. The second and third terms states the vorticity being stretched, and diffused by the viscosity,  $\nu$ , respectively [27].

### 3.1.1 Vortex generation

Generation of vorticity can be caused by different mechanism in the flow. One example is density variations as a result of temperature variations in the flow. Another example is boundary layer formations. The velocity varies from zero at the wall to free stream velocity far from the wall. With small variations normal to the wall compared to large tangential variations causes vorticity with large and negative values [27, 28]. This is illustrated in Fig. 3.1.

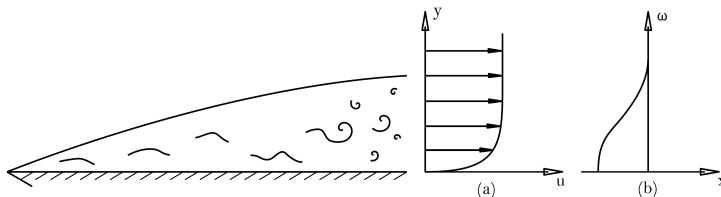


**Figure 3.1:** Sketch of boundary layer with profiles of (a) Velocity and (b) Vorticity.

Vorticity is also generated by boundary layer separations which occurs at corners or surfaces with relatively high curvature [27]. As the flow separates, the vorticity in the boundary layer transitions into a free shear layer of which spirals into a concentrated vortex [26]. If the separated flow reattaches, a vortex bubble is created.

Shear layer vortices is formed due to instabilities in two or more interacting layers of fluid. They can have different velocities, or different densities, or both. As an example, taking the same fluid with different velocity profiles, after a certain time of interaction, the two layers starts to become unstable. Also referred to as Kelvin-Helmholtz instabilities and an example of this is presented in Fig. 3.2.

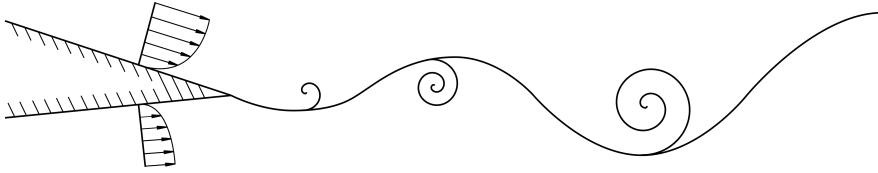


**Figure 3.2:** 2D sketch of blade tip vortex caused by free shear layer and Kelvin-Helmholtz instabilities. Note, the illustration is exaggerated.

### 3.1.2 Secondary flow

A flow can be broken down into a primary flow and a secondary flow. Primary flow is chosen as an approximation to the governing equations by neglecting any viscous effects. The secondary flow on the other end accounts for viscous effects such as boundary layer development due to no slip conditions at surfaces.

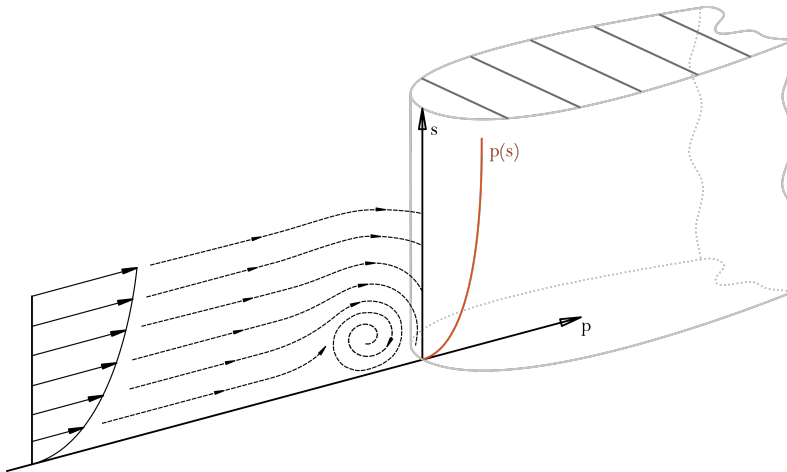


**Figure 3.3:** Illustration of a single structured horseshoe vortex at blade leading edge.

#### *Horseshoe vortex*

Horseshoe vortex is produced between the blade leading edge (LE) and the hub or shroud wall. It develops as the incoming flows boundary layer interacts with an increasing pressure field along the leading edge (spanwise

direction) as the blades radius increases [29]. The spanwise pressure gradient drives the local flow towards the walls boundary layer forming the horseshoe vortex. See Fig. 3.3 for a closer presentation.

The structure and strength is dependent on the leading edge radius which is shown in Fig. 3.4. A large single vortex is formed if the radius is greater than the boundary layer thickness,  $\delta$  (Fig. 3.4a). In the opposite case, the horseshoe vortex is then made up of smaller vortices varying in size and strength (Fig. 3.4b). Here, the large single vortex is the strongest and will therefore lead to higher losses during turbine operations [29].

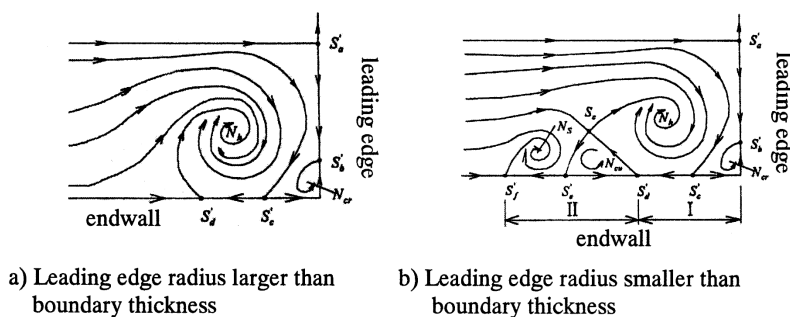


**Figure 3.4:** Horseshoe vortex structure for different leading edge radii [3].

From the leading edge, the horseshoe vortex develops into two new vortices, called counter vortex and passage vortex. The counter vortex travels along the suction side of the blade while the passage vortex travels along the pressure side. A full overview of vortex structures in the turbine channel is given in Fig. 3.5.

#### *Passage and counter vortex*

The passage vortex is the strongest and most dominant structure in the blade channel, considering that there is no tip leakage vortex presence. This has to do with the effect of cross flow from the hub/shroud wall moving relative to the flow direction, amplifying the circulation strength of the vortex. As seen in Fig. 3.5, the vortex path is towards the incoming blade and could alternatively be interacting with low pressure vortices on the suction side, such as counter vortex or Corner vortex. Regarding the Corner vortex, there is no agreement in the field of research on the existence of the Corner vortex and its trajectory [29]. Meaning, the development of the vortex could be case sensitive.

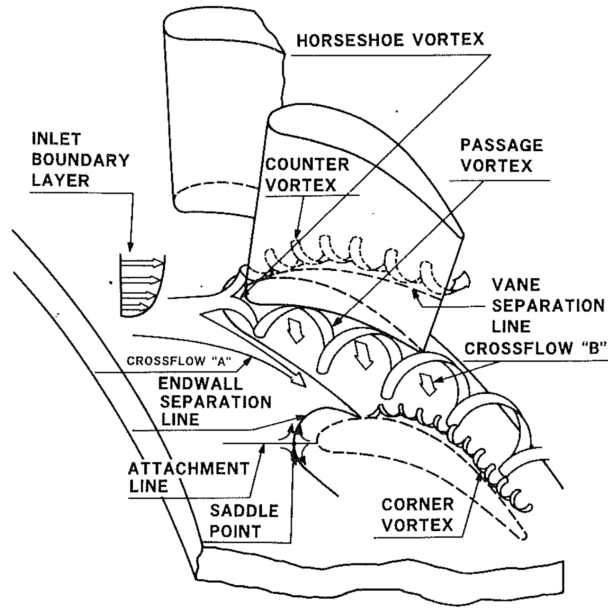


**Figure 3.5:** Secondary flow structures in a blade channel [4].

The counter vortex is found along the suction side leg of the rotor blade and has less strength compared to the passage vortex. However, the vortex can, in some cases, interact in a co-rotational structure with the passage vortex. Otherwise, the vortex will transition in the spanwise direction towards the wall on the opposite side, or take the path underneath the passage vortex [29].

#### *Vortex breakdown*

Vortex breakdown is characterized by an internal stagnation point along the vortical axis, leading to locally reversed flow. There are two forms of vortex breakdown which is predominant, one called "near-axisymmetric" which takes the form of a "bubble" shape, and the other one is called "spiral" [30]. A vortex breakdown can occur in the draft tube of a Francis turbine as the discharge is reduced, e.g. during shutdown. The vortex breakdown is created as the swirling velocity components produces an internal stagnant region along the turbines center axis, and a central quasi stagnant region in the flow is developed as a result of the vortex breakdown [31].

### 3.2 Rotor stator interaction

Rotor stator interaction is pressure pulsations with discrete frequency spectra due to variations in pressure field from interactions of rotating runner blades and stationary guide vanes. Another excitation mechanism is the stochastic pressure fluctuations with continuous frequency spectra as a result of vortex formations, transient pressure variations from turbulence generation and system vibrations. Therefore, the pressure waves caused by the interference is due to two reasons [32]:

1. Impulses is generated as the rotating runner blades interacts with the vortex path caused by the wake from the guide vanes.
2. The rotating pressure field from the runner blades interferes with the guide vanes and reflects pressure waves into the system.

Pressure pulsations from the runner is caused by inhomogeneous stationary pressure waves due to pressure differences over each runner blades and from local pressure variations inside the blade channel. This pressure field will move with the runner angular speed,  $n$ , with respect to the stationary frame of reference as seen in Fig. 3.6. Pressure field function is therefore a function of time and runner position relative to the guide vanes as  $p(\phi - nt)$  [32]. Here,  $\phi$  is the central angle and  $n$  is the runner angular speed in  $\text{rad s}^{-1}$ .

The mathematical expression for a periodic function of pressure pulsations from the runner blade and its harmonics can be expressed using a Fourier series in the real form as [32],

$$p(\phi, t) = \sum_{k=0}^{\infty} \alpha_k \cos[kz_r(\phi - nt) + \Phi_k] \quad (3.3)$$

where  $k$  is the harmonic number, for 0 being the fundamental harmonic,  $\alpha_k$  is the amplitude,  $\Phi_k$  denotes the phase angle and  $z_r$  is number of runner blades. The pressure field at a point in time is therefore represented by a superposition of harmonic functions. For each harmonic pressure wave, the number of complete waves with wave length,  $\lambda$ , equals the integer,  $k$ , multiplied by the number of vanes [32].

From a stationary point in the vaneless space, the excitation frequency due to pressure pulsations from the runner alone can be expressed as follows,



$$f_r = z_r f_n \quad (3.4)$$

where  $f_n = n/60$  is the runner rotational frequency.

The pressure pulsations due to the guide vanes alone follows the same equation as presented by Eq. 3.3, the only difference is number of blades. In addition, the same equation holds for the guide vane excitation frequency as [32],

$$f_s = z_s f_n \quad (3.5)$$

where  $z_s$  is number of guide vanes.

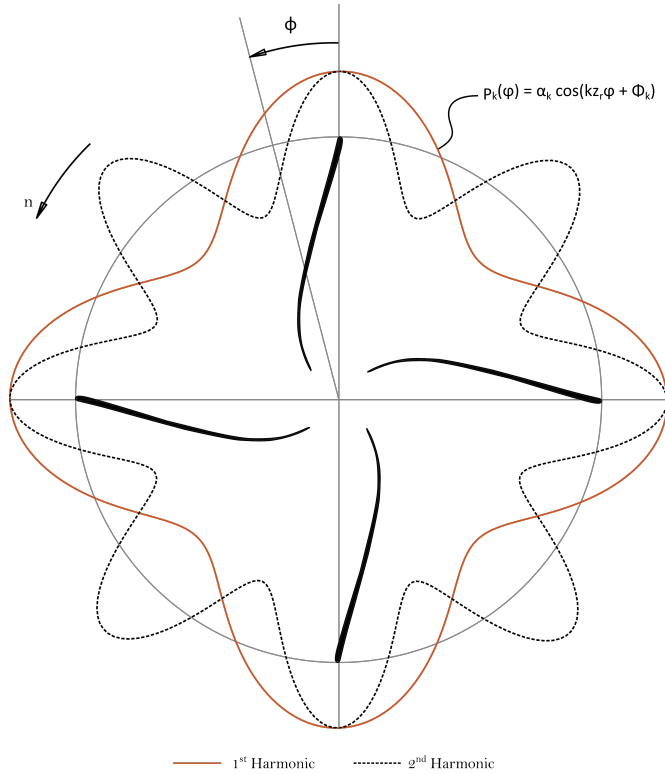


**Figure 3.6:** Illustration of 1st and 2nd harmonics of fluctuating pressure field from four runner blades.

Now the mathematical representation of RSI can be derived by defining a stationary point in the vaneless space with respect to the pressure field characterized by Eq. 3.3. By assuming,  $z_r$  number of runner blades and  $z_s$  number of guide vanes, the following equation for the pressure pulsations for each position and time due to RSI is [32],

$$p(\phi, t) = \sum_{k=0}^{\infty} \sum_m z_s \alpha_{m,k} \cos[m\phi - k \cdot z_r \cdot n \cdot t + \Phi_{m,k}] \quad (3.6)$$

where  $m = kz_r + iz_s$ , for  $k = 1, 2, 3, \dots$  and  $i = 0, \pm 1, \pm 2, \dots$ . For positive and negative values of  $m$  defines a pressure wave rotating with or against the direction of runner rotation, respectively. As seen from Eq. 3.6, the interference pressure field consists of a superposition of an infinite number of rotating pressure curves for a given harmonic  $k$ -value. Here, the wave number in each pressure curve is defined by the numerical value of  $m$  [32].

As the function for RSI is describe through a Fourier series, the analytical approach when handling large data sets is Fast Fourier Transform (FFT). This is a mathematical algorithm of which computes the discrete Fourier transform of a signal consisting of noise or multiple frequencies. By converting the signal from its original domain into a frequency domain, one can point out the different frequencies and their amplitudes. It should be noted that there is limitations and drawback of using FFT on signals retrieved from a CFD analysis. The frequency resolution is the distance between bins defined by the energy from the signal at certain frequencies. Here, the resolution is restricted to the sampling frequency divided by the size of signal [33]. Therefore, given that most CFD simulations have relatively short time frames means that the resolution of the FFT plot will be significantly reduced compared to experimental signals taken over a longer time frame.

Another method based on the FFT is called Short-Time Fourier Transform (STFT). This method uses the FFT algorithm on small sections of the signal, called windows, as the signal changes in time. A Fourier spectrum on each section is presented in a time-frequency domain, known as a spectrogram. In recent year, different window functions has been proposed, each conformed for a specific type of signal. The details of these window functions will not be covered due to the simplicity of this thesis.

### 3.3 Mathematical foundation

The mathematical foundation in any research and engineering cases involving fluid mechanics are the Navier-Stokes equations which describes the laws of conservation of mass, momentum and energy. These equations are four dimensional non-linear partial differential equations in the time-space domain. In most engineering cases, there are no analytical solutions, hence the use of CFD to solve the equations numerically. ANSYS CFX<sup>®</sup> solves the unsteady Navier-Stokes equations through finite volume method, which is the most common solution method [34]. The mathematical outline of the governing equations and solution methods will not be covered as this is readily available in the literature.

#### 3.3.1 Turbulence models

The rotating fluid structures are referred to as turbulent eddies which varies in different time and length scales. The turbulent energy cascade, seen in Fig. 3.7, describes the transfer of turbulent energy from larger eddies to smaller eddies of which is eventually dissipated into heat through molecular viscosity [35]. Turbulence models are typically divided into three regions based on the amount of turbulent eddies resolved by the model. Direct Numerical Simulations (DNS) resolves the entire range of wave length where as Reynolds-Averaged Navier-Stokes (RANS) models the entire region by solving additional sets of transport equations. There are hybrid models available of which both resolves a set range of wave length, and models the rest. This is referred to as Scale-Resolving Simulaion (SRS) methods where LES is an example of a SRS method. However, DNS and LES methods are highly time and computational demanding. Therefore, recent hybrid models have been developed that mixes between LES and RANS resulting in less computational time and resources. One example of such model is the SAS-SST  $k - \omega$ , which stands for Scale-Adaptive Simulation (SAS) of the Shear Stress Transport  $k - \omega$  equations. The mathematics behind the model will be covered in details during the following section starting with a short introduction to the Unsteady RANS equations (URANS) and the related Closure Problem. For a more general overview of the SAS-SST model, see Menter and Egorov [36] and Egorov et al. [37].

The URANS equations for mass and momentum are expressed in tensor form as,

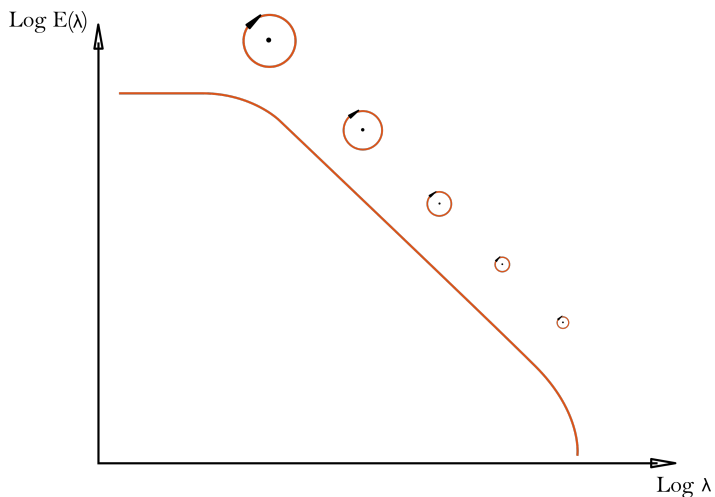


**Figure 3.7:** Energy cascade for turbulent kinetic energy as a function of wave length,  $\lambda$ .

$$\frac{\partial U_k}{\partial x_k} = 0, \quad (3.7)$$

where  $U_k$  is the mean velocity in the  $k$ 'th direction, and

$$\frac{\partial U_i}{\partial t} + \frac{\partial U_i U_j}{\partial x_j} = -\frac{1}{\rho} \frac{\partial p}{\partial x_i} + \frac{\partial}{\partial x_j} \left( \nu \frac{\partial U_i}{\partial x_j} - R_{ij} \right), \quad (3.8)$$

where  $p$  is the mean pressure,  $\rho$  is the density and  $\nu$  is the kinematic viscosity [34]. Here,  $R_{ij}$  is the Reynolds Stress tensor which is the unknown term and has to be resolved by a turbulence model to close the system. The Reynolds Stress tensor is obtained using the Boussinesq turbulent viscosity hypothesis [38]:

$$R_{ij} = -\overline{u'_i u'_j} = \nu_t \left( \frac{\partial U_i}{\partial x_j} + \frac{\partial U_j}{\partial x_i} \right) - \frac{2}{3} \delta_{ij} \left( k + \nu_t \frac{\partial U_n}{\partial x_n} \right) \quad (3.9)$$

Here  $\nu_t$  is the turbulent eddy viscosity,  $k$  is the turbulent kinetic energy.  $\delta_{ij}$  is the Kronecker delta which is 1 for  $i = j$ , otherwise 0.  $u'$  is the time-varying, fluctuating component of the velocity. Last term involves the divergence of the velocity field and are usually neglected for flows with incompressible

fluid [34]. The unknown quantity is the turbulent eddy viscosity which has to be solved for, and is referred to as the closure problem in the literature.

The SAS-SST  $k - \omega$ , hereby termed SAS-SST, is based on the older turbulence model by Menter, namely the SST  $k - \omega$ , only the difference is the additional source term,  $Q_{SAS}$  which is added to the transport equation for turbulent eddy frequency,  $\omega$ . It introduces the von Kármán length-scale which allows the initial URANS model to dynamically adjust to resolve turbulent structures [34]. Formally, the SST  $k - \omega$  model is based on the Baseline (BSL)  $k - \omega$  model presented by Menter [39] and are solving for two additional transport equations which is the turbulent kinetic energy,  $k$ , and the turbulent eddy frequency.

The two transport equations for the SAS-SST model are as following [40]:

$$\frac{\partial(\rho k)}{\partial t} + \frac{\partial}{\partial x_j} (\rho U_j k) = \frac{\partial}{\partial x_j} \left[ \left( \mu + \frac{\mu_t}{\sigma_{k3}} \right) \frac{\partial k}{\partial x_j} \right] + P_k - \beta' \rho k \omega + P_{kb}, \quad (3.10)$$

$$\begin{aligned} \frac{\partial(\rho \omega)}{\partial t} + \frac{\partial}{\partial x_j} (\rho U_j \omega) &= \frac{\partial}{\partial x_j} \left[ \left( \mu + \frac{\mu_t}{\sigma_{\omega 3}} \right) \frac{\partial \omega}{\partial x_j} \right] \\ + (1 - F_1) \frac{2\rho}{\sigma_{\omega 2} \omega} \frac{\partial k}{\partial x_j} \frac{\partial \omega}{\partial x_j} &+ Q_{SAS} + \alpha_3 \frac{\omega}{k} P_k - \beta_3 \rho \omega^2 + P_{\omega b}, \end{aligned} \quad (3.11)$$

where  $\mu$  is the dynamic viscosity and  $\mu_t$  is derived from  $\nu_t = \mu_t / \rho$ .  $P_k$  is turbulence production due to viscous forces and,  $P_{kb}$  and  $P_{\omega b}$  represents the influence from buoyancy forces [34].

The additional  $Q_{SAS}$  term is mathematically expressed from the latest model version as follows [40],

$$\begin{aligned} Q_{SAS} = \max \left[ \rho \zeta_2 \kappa S^2 \left( \frac{L}{L_{vK}} \right)^2 \right. \\ \left. - C \cdot \frac{2\rho k}{\sigma_\Phi} \max \left( \frac{1}{\omega^2} \frac{\partial \omega}{\partial x_j} \frac{\partial \omega}{\partial x_j}, \frac{1}{k^2} \frac{\partial k}{\partial x_j} \frac{\partial k}{\partial x_j} \right), 0 \right] \end{aligned} \quad (3.12)$$

where,  $\zeta_2 = 3.51$ ,  $\sigma_\Phi = 2/3$  and  $C = 2$ , is model parameters, and  $L$  is the length-scale of the modeled turbulence given as [40],

$$L = \frac{\sqrt{k}}{C_\mu^{\frac{1}{4}} \omega} \quad (3.13)$$

where the constant,  $C_\mu = 0.09$ .

The von Kármán length-scale,  $L_{vK}$  is based on the three-dimensional generalization of the classic boundary layer definition  $\kappa U'(y)/U''(y)$ . Here,  $\kappa = 0.41$  is the von Kármán constant. The first velocity derivative is defined as  $S = \sqrt{S_{ij}S_{ij}}$ , based on the scalar invariant of the strain rate tensor,  $S_{ij}$ , given by Eq. 3.14. The second velocity derivative is represented by the magnitude of the velocity Laplacian and is given by Eq. 3.15 [40].

$$S_{ij} = \frac{1}{2} \left[ \frac{\partial U_i}{\partial x_j} + \frac{\partial U_j}{\partial x_i} \right] \quad (3.14)$$

$$\|\nabla^2 U\| = \sqrt{(\nabla^2 u)^2 + (\nabla^2 v)^2 + (\nabla^2 w)^2} \quad (3.15)$$

By substitution, the final equation for the von Kármán length-scale can be expressed as follow [40],

$$L_{vK} = \frac{\kappa S}{\|\nabla^2 U\|} \quad (3.16)$$

However, it should be noted that, the latest version of the SAS-SST model introduces a new formulation for  $L_{vK}$  of which provides a direct control of the high wave number damping. The new formulation adds a limiter of which is proportional to the grid size,  $\Delta = \mathcal{V}^{1/3}$ , where  $\mathcal{V}$  is the cell volume. This function is added to control the damping of the finest resolved turbulent fluctuations [40]. Hence, by refining the mesh sufficiently, one can obtain LES like resolution for turbulent structures. For a complete derivation of the SAS-SST model, see Egorov and Menter [40].

Finally, to be able to close the set of equations, the eddy viscosity can be derived by assuming equilibrium state between production and destruction of the turbulent kinetic energy, through the source term in both transport equations. Then the following relation between the equilibrium eddy viscosity,  $\nu_t^{eq}$ ,  $L_{vK}$  and  $S$  can be derived as [40],

$$\nu_t^{eq} = \left( L_{vK} \sqrt{\frac{\frac{\beta}{C_\mu} - \alpha}{\kappa \zeta}} \right) S \quad (3.17)$$

Where  $\beta$ ,  $\alpha$  and  $\zeta$  is closure coefficients.

Note that the SAS-SST model integrated in to ANSYS CFX<sup>®</sup> has two options for defining the eddy viscosity. Here, the method presented above is the default option, where as the second option limits the eddy viscosity directly. For more information on the second option, see ANSYS CFX<sup>®</sup> manual [34].

### 3.3.2 Near wall physics

To successfully predict the turbulent flow bounded to the wall, one need to predict the large gradients due to viscous effects. The two main effects of a wall, especially in turbomachinery, are [41]:

1. Damping the wall normal components, making the turbulent flow anisotropic
2. Increasing the production of turbulence through the shearing mechanism in the flow.

Here, the  $y^+$  value is the non-dimensional distance from the wall to the first node of which scales with the boundary layer thickness. The mathematical expression is,

$$y^+ = \frac{y u_\tau}{\nu}, \quad (3.18)$$

where  $y$  is the absolute distance from the wall and  $u_\tau$  us the frictional velocity.

The near wall region can be divided into three regions by turbulence physics, which is [41]:

- ❖ Viscous sub-layer:  $0 \leq y^+ \leq 5$
- ❖ Buffer layer:  $5 \leq y^+ \leq 30$
- ❖ Inertial sub-layer:  $30 \leq y^+ \leq 200$

The flow condition in the viscous sub-layer is laminar, hence the turbulence can be neglected. For the inertial sub-layer, the viscous effects are small as the flow is not affected by the wall. Now, the buffer layer is the region where the turbulence and viscous effects are significant.

There are two computational approaches, either fully resolve the viscous sub-layer near the wall, or using a wall function. Using the first approach, one has to ensure that the first node are within the viscous sub-layer, following the recommended  $y^+$  value by the selected turbulence model. One such turbulence model is the SAS-SST presented in Sec. 3.3.1 which resolves the viscous effects for all near wall cells. However, the computational cost is high compared to the use of a wall function, as the number of nodes in the boundary layer scales significantly with higher Reynolds number.

The latter method uses a standard wall function to predict the solution gradients. Then the first element node needs to be placed outside the buffer layer with a restrictive  $y^+$  value within the inertial sub-layer. Failing to be within this range could lead to numerical instabilities [42]. However, in recent year, some CFD software are using automated wall treatment with scalable wall function. This enables less restriction on the  $y^+$  value compared to the use of a standard wall function [18].



## Numerical methodology

*In this chapter the numerical methodology will be presented. Starting with an overview of the case setup including software and operating conditions for the project case followed by a presentation of mesh details with quality aspects. Then a section on verification with results from GCI study will be given, followed by a section covering two methods of validation. Finally, an overview of the computational setup is provided, ending with an outline of the developed remeshing architecture.*

### 4.1 Case overview

The shutdown sequence of the Francis turbine is numerically modelled. The software used for meshing is ANSYS<sup>®</sup> ICEM CFD<sup>™</sup> and TurboGrid. For the numerical calculations, ANSYS CFX<sup>®</sup> has been used which includes CFX Pre, CFX Solver and CFX Post for case setup, calculations and post processing, respectively. Matlab is used as an additional post processing tool for large data sets and visual presentation. Experimental data at each steady state operating conditions listed in Table 4.1 are available. Some transient operating sequences are also available, such as shutdown which is relevant in this case.

A complete simulation from BEP to ML was selected as the shutdown sequence. The transient simulation is initiated from a steady state simulation at BEP. The guide vane angle,  $\alpha$  is measured from closed position, zeroing at  $0^\circ$ . A linear change in guide vane angle and volume flow rate is assumed from  $\alpha = 9.84^\circ$  and  $Q = 0.19959 \text{ m}^3 \text{ s}^{-1}$  at BEP to  $\alpha = 1^\circ$  and  $Q = 0.02 \text{ m}^3 \text{ s}^{-1}$  at ML. For the flow to settle, time of two runner rotations, i.e.  $t = 0.36 \text{ s}$ , was added before and after the shutdown sequence, see Fig. 4.1.

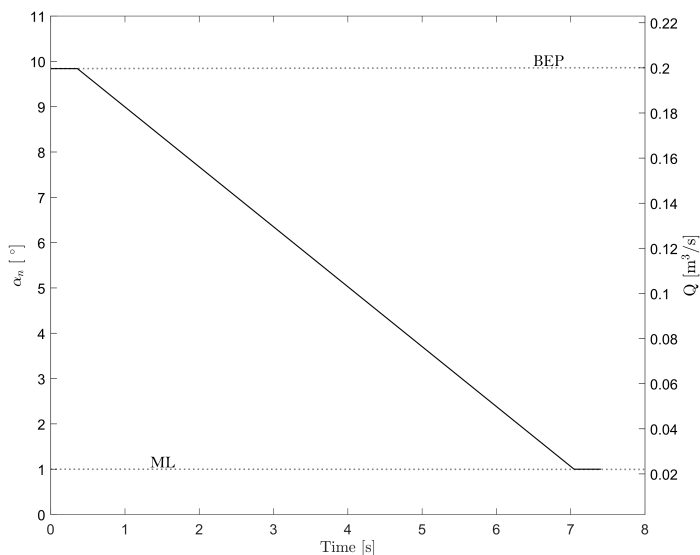


**Figure 4.1:** Guide vane angle (left) and volume flow rate (right) based on experimental setup in workshop 2

The runner angular speed is maintained constant throughout the sequence at  $\omega = 34.8 \text{ rad s}^{-1}$ . A water temperature of  $25 \text{ }^\circ\text{C}$  was set and a density equal the experimental setup of  $999.8 \text{ kg m}^{-3}$ . A downstream pressure of  $101\,325 \text{ Pa}$  was used based on measurements from earlier simulations.

**Table 4.1:** Operating conditions from experiments conducted in workshop 2 [1].

Parameter	BEP	PL	ML
Guide Vane Opening Angle [ $^\circ$ ]	9.84	6.72	1
Discharge [ $\text{m}^3 \text{ s}^{-1}$ ]	0.19959	0.13962	0.022
Net Head [m]	11.94	11.87	12.14
Torque [Nm]	621	421	16
Hydraulic Efficiency [%]	92	90	21

Several monitoring points were created throughout the system to monitor pressure fluctuations. Monitor points DT1 and DT2 in the draft tube includes velocity measurements. In the stator domain, there are 8 monitor points which can be viewed in Fig. 4.2. The location of VL2 is positioned relative to the test rig. It should be noted that SF1 and SF2 is positioned

in the mid span, where the rest is positioned at the lower wall. For the two other domains, there are four monitor points in the runner and five in the draft tube. There are three velocity lines in the draft tube, two horizontal and one vertical line. An overview can be found in Appendix-B for the two last domains, including global coordinate for all points and lines.

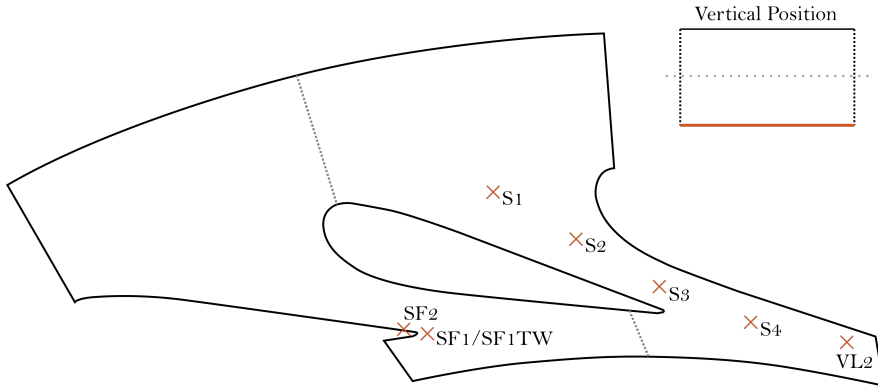


**Figure 4.2:** Overview of monitor point position in stator domain.

The solution output frequency used during simulation was defined with a time list which is writing a solution file for each specified time. The selected times can be seen in Fig. 4.3. The main time is set at PL, deep part load (DPL) and ML including six or four output files centered around each main time. The difference in time between two solution output was selected to be one runner revolution. The region of light green indicates possible remeshing governed by interrupt condition. More on interrupt condition in Sec. 4.5.

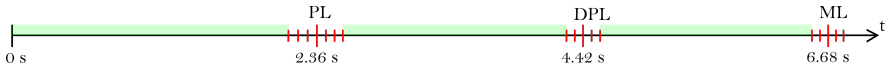


**Figure 4.3:** Solution output frequency time line shown by red lines. Shaded regions in light green shows possible time for remeshing.

The computational domain considered in this study is two periodic guide vane passage, one periodic runner passage and a simplified draft tube domain, presented in Fig. 4.4 and Fig. 4.5. Note, due to the initial projects complexity regarding LES simulation, the draft tube domain was reduced to save computational resources. As the project changed, the time left was limited - resulting in using the same domain for the draft tube. The outlets position was selected as a minimum distance from runner outlet without af-

fecting the RVR in the draft tube. The runner domain consists of a splitter blade and one main blade. Since one periodic section of runner accounts to  $24^\circ$ , two guide vane domains is added yielding a total pitch angle of  $25.71^\circ$ . Note, the change in pitch results in an interface overlap of 7.1%, however, this is covered by the general grid interface (GGI) and Transient Rotor Stator interface by specifying a pitch ratio. For more information, see Sec. 4.5 on computational setup.

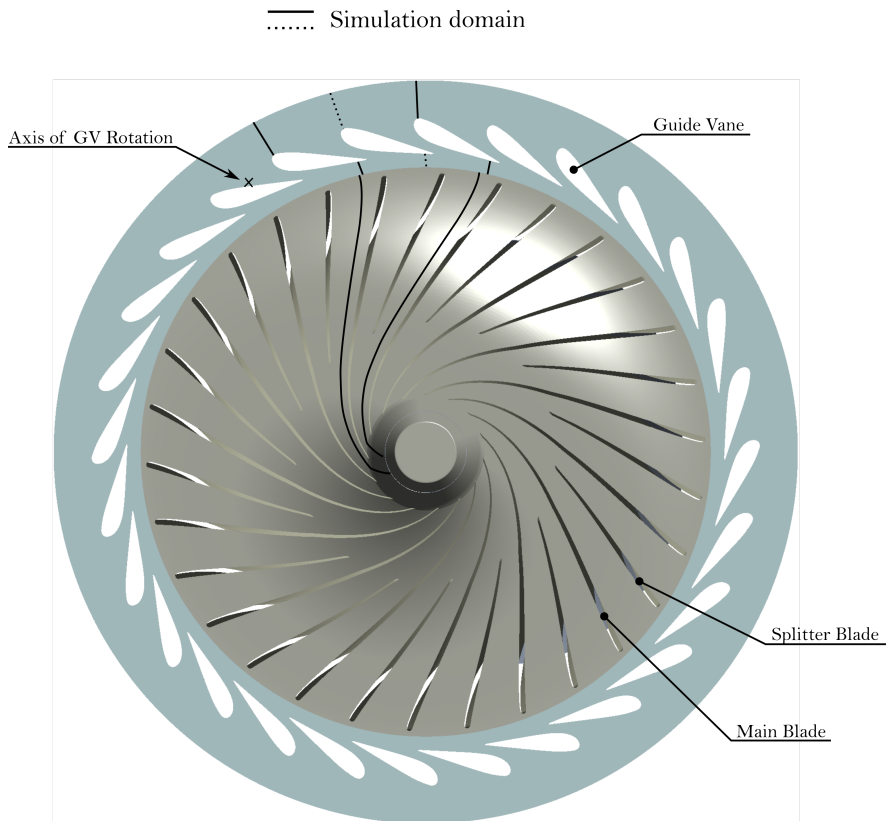


**Figure 4.4:** Overview of stator domain with guide vanes and rotor domain with main blades and splitter blades of the Francis-99 used in the present work.

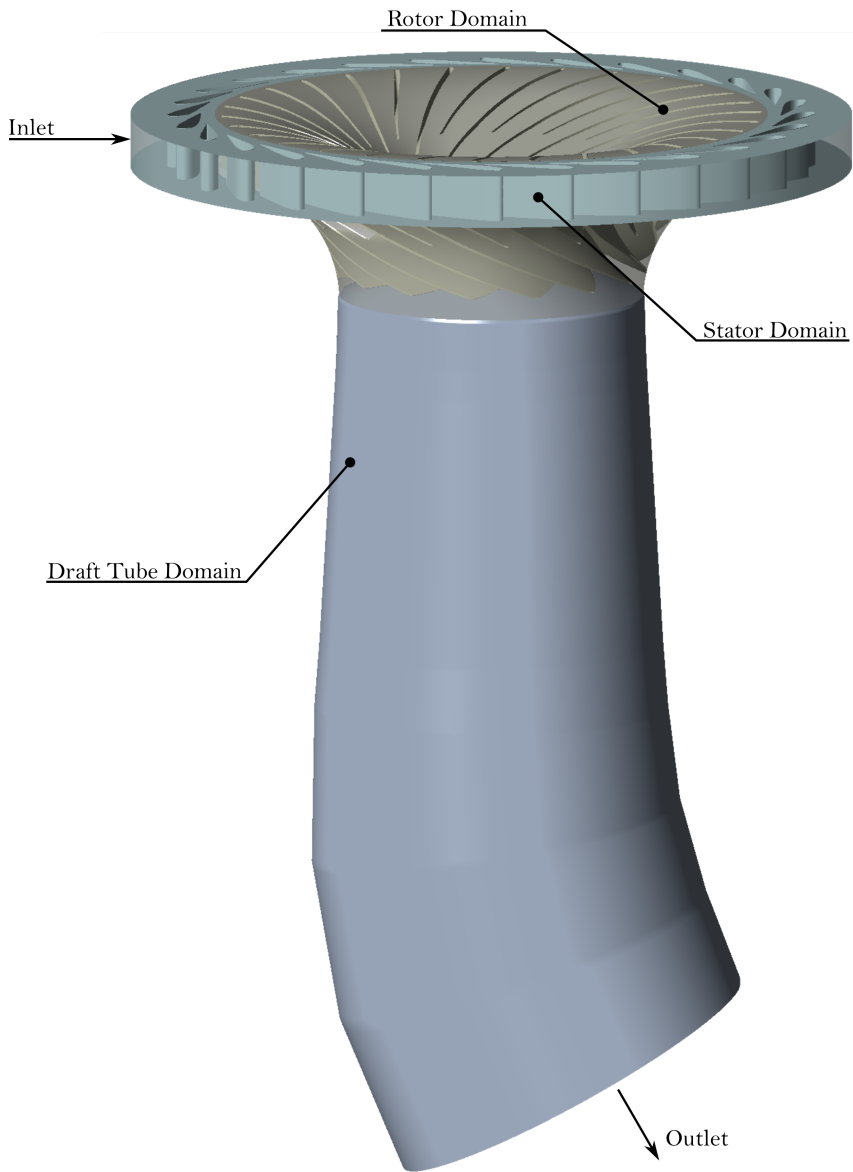


**Figure 4.5:** Three dimensional model of the Francis-99 used in the present work.

## 4.2 Mesh overview

The mesh for each domain was created separately. For GV and DT domain, a three-dimensional structured multi-block mesh was created in ICEM CFD™. For the runner domain, a automated topology based mesh for complex blade geometry was created in ANSYS TurboGrid™. The total fluid domain consists of around 14.4 million elements with a total volume of 0.122 m<sup>3</sup> resulting in an average cell size of 2 mm. To the best of the authors' knowledge, the average cell size accomplished is relatively fine compared to available literature, and will be of importance when solving the turbulent field in the turbine. An overview of mesh quality is given in Table 4.2.

**Table 4.2:** Mesh statistics and quality at BEP

	Criteria	GV	RN	DT
# of elements		1 956 310	6 066 000	3 996 576
Min. Face Angle	>10°	31.8	21.1	39.8
Aspect Ratio	≈ 1	≥1.03	≥1.09	≥1.00
Element Volume Ratio	<5	5	4.1	5
Connectivity Number	<24	10	10	12

The overall mesh quality for all domains are within the limits. The low value of minimum face angle in the runner domain is located at the main blade trailing edge, while the rest of the elements yields the same values as for the other domains. Element Volume Ratio describes the change in element volume from one cell to neighboring cells, and has great influence on the accuracy of the numerical solution. Here, the values for GV and DT are at the boarder, yet within acceptable value. All the given criteria is software based and is given in ANSYS® user manual [43].

In this present work, the target average and max  $y^+$  values was chosen to be 1 and 3, respectively. The low  $y^+$  value was selected so that the gradients are accurately resolved which is important to impose boundary layer separation. Table 4.3 presents the final results for  $y^+$  on all walls. During dynamic mesh motion, thin prism cells at the upper and lower ring would deform and cause negative element volume. Therefore, it was chosen to use adaptive wall functions on these surface, hence the high numbers. Here, both max and mean values for each surface are within the limit of  $30 < y^+ < 200$ .

A complete overview of generated mesh for all domains are presented in App C. It should be noted that the quality values presented above for GV

**Table 4.3:** Mesh  $y^+$  values measured at BEP

	Max $\leq 5$	Mean $\leq 1$
Upper Ring	145.5	94.1
Lower Ring	147.0	94.5
Hub	2.7	1.1
Shroud	2.8	1.0
Main Blade	2.9	1.4
Splitter Blade	3.0	1.1
Runner Cone	2.9	1.7
Draft Tube Wall	3.1	1.1

domain is measured at BEP and will vary throughout the simulation. As the guide vanes are closing, the mesh quality will degrade. To counteract this, a remeshing architecture has been created and will ensure good quality during simulation. Orthogonality angle has here been used as a measure of quality during shutdown and the results of remeshing can be seen in Fig. 4.6.

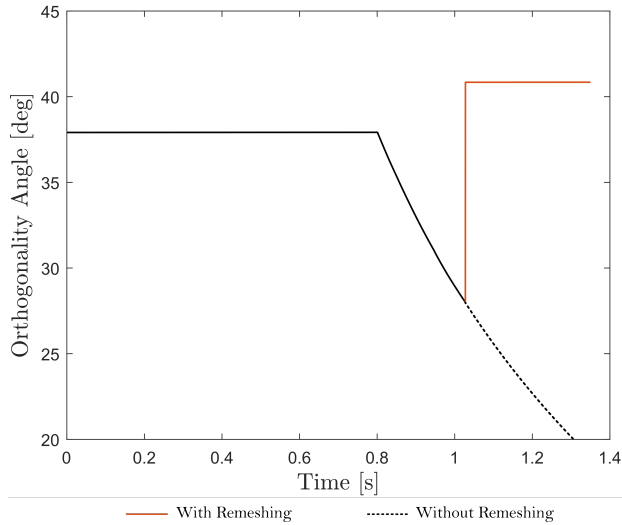


**Figure 4.6:** Progress of Orthogonal Angle during simulation with and without remeshing.

Here it is evident that without remeshing, the orthogonal quality would reach below  $20^\circ$  before reaching  $t = 1.4$  s. The value of  $20^\circ$  is the software

recommended minimum, as lower values will result in inaccurate solutions. More on remeshing can be found in Sec. 4.5 and Sec. 5.3.

### 4.3 Verification

A verification assessment is used to quantify the numerical accuracy of the mathematical programming and implementation of numerical models. The assessment compares the programs mathematical code to exact analytical solutions to find the level of uncertainty and error. The objective is to ensure that the numerical solution is accurate, thrust worthy, and for the results to be considered credible. In addition to the solution code, models used in CFD analysis can consist of complex shapes, making topological verification important regarding numerical accuracy. Here, the topology tolerance should be checked and verified, and if possible, the user should adjust the tolerance accordingly to reduce the error of the model.

The commercial software used in this present work is ANSYS CFX<sup>®</sup> which has well documented verification cases found in the customer manual [44]. In addition to the verification assessment, the program runs a physics verification sequence checking the numerical setup before exporting the definition file to the solver. In this way, the user is ensured that there is no error related to incorrect setup. In creation of the 3 dimensional geometry files, both TurboGrid and ICEM CFD<sup>™</sup> was used. TurboGrid uses program controlled topology tolerance where no value is specified in the documentation. In ICEM CFD<sup>™</sup>, the user can specify a topology tolerance or use the program default tolerance of 0.001 m. It was found that high tolerance was needed with respect to the use of dynamic mesh. Therefore a user specified topology tolerance of 1E-20 m was set.

A GCI study was made for the stator and rotor domains. For each domain, a total of three grids,  $M_1$ ,  $M_2$  and  $M_3$ , were created. The pressure was used as a local parameter for both domains, and torque as a global parameter for the runner domain only. The results from GCI is presented in Table 4.4 where the numerical uncertainty for the finest grid solution is 0.023%, 0.084%, 0.098% and 0.031% for VL01, R1, R4 and torque, respectively. It should be noted that the stator grid is dynamically changed during the simulation, meaning the results from the GCI study in this domain will be of limited use. However, it will serve as an indication for the discretization error and uncertainty. Moreover, the discretization error does not account for any modeling error [45], hence, this is covered in Sec. 4.4.



**Table 4.4:** Grid convergence index study of discretization error for stator and rotor domains.

	Stator:	Rotor:		
	$\phi = \text{VL01}$ Pressure [kPa]	$\phi = \text{R1}$ Pressure [kPa]	$\phi = \text{R4}$ Pressure [kPa]	$\phi = \text{Torque}$ [Nm]
$M_1, M_2, M_3$	1 942 864, 697 004, 276 342	6 066 000, 1 854 480, 607 240	(")	(")
$r_{21}$	1.4074	1.4844	1.4844	1.4844
$r_{32}$	1.3612	1.4508	1.4508	1.4508
$\phi_1$	167.47	153.31	105.41	617.59
$\phi_2$	167.56	153.49	105.53	617.24
$\phi_3$	167.88	153.91	105.79	617.19
p	4.10	2.51	2.22	3.03
$\phi_{ext}^{21}$	167.44	153.21	105.33	617.74
$e_{st}^{21}$	0.06 %	0.11 %	0.11 %	0.06 %
$e_{ext}^{21}$	0.02 %	0.07 %	0.08 %	0.03%
$GCJ_{M1}^{21}$	0.023 %	0.084 %	0.098 %	0.031 %

## 4.4 Validation

The validation assessment is a process of which the numerical solutions is checked against known physical values. The goal is to get the numerical results as close to the physical reality by comparing the solutions to experimental data. In this present work, two validation assessments were made. First, a validation of pressure monitor points and turbine performance characteristics. Second, a validation of the draft tube mesh using PIV measurements and velocity results.

One steady state and one transient simulation was made at BEP. The steady state simulation was ran until the monitor points converged. The total time for the transient simulation was two runner revolutions. The time selected was sufficient for all monitor points to stabilize. Simulation data is here compared with experimental data from workshop 1 and 2. No data was found on pressure readings in the runner, meaning the data from VL01, VL2, DT1 and DT2 sensors was used in comparison. See Fig. 4.2 in Sec. 4.1 and Fig. B.2 in Appendix-B for monitor locations. Note, VL01 is not prescribed in Fig.4.2, however its position is close to SF1.

From Table 4.5, the numerical results shows close agreement with experimental results. Here, VL2 has the highest relative error which is caused by the selected outlet pressure of 101 325 Pa. Therefore, the error is expected as the operating pressure for this simulation is closer to the experimental operating condition from workshop 1. Referring to results derived from previous project work where the relative error of 0.29 % for VL2 was found for adjusted outlet condition [46].

The horizontal and axial velocity components from the time averaged simulation was compared against experimental Particle Image Velocimetry (PIV) data. The PIV plane is constructed by two horizontal lines (Line 1 and 2) and a vertical line (Line 3). See Fig B.2 for reference. Line 1 and 2, and Line 3 follows a positive direction vector  $(i,j,k) = (-0.191,-0.982,0)$  and  $(i,j,k) = (0,0,1)$ , respectively. The overall characteristics presented in Fig. 4.7 shows close agreement with experimental PIV measurements. The largest deviations is for the axial velocity in all three lines. Deviation in axial velocity from Line 3 is caused by a lower outlet pressure resulting in higher velocity field in the draft tube. This is also the case for the axial velocity closer to the center of Line 1 and 2. The low velocity regions at each end of Line 1 and 2 is caused by the wake from the runner blades which has not fully dissipated.

**Table 4.5:** Validation of pressure and turbine performance at BEP

	Numerical	Experimental	Rel. Error
VL01 [kPa]	174.2	171.6	1.49%
VL2 [kPa]	163.9	173.2	-5.38%
DT1 [kPa]	100.3	101.4	-1.04%
DT2 [kPa]	100.3	101.2	-0.91%
Head [m]	11.97	11.94	0.25 %
Torque [Nm]	626.59	620.65	0.96 %
Hydraulic Efficiency [%]	93.00	92.39	0.70 %

By summarizing the verification and validation, the highest relative error found from the validation of pressure and turbine performance was 1.49% after taking the relative error of 0.29% for VL2 into account. Hence, the highest relative error is small and at an acceptable level. The validation of the velocity field in the draft tube was found reliable, as the only deviation found was caused by the chosen operating condition, which will change throughout the shutdown phase. The numerical uncertainty reported in the GCI study is at a satisfactory level with relatively small values. Therefore, the overall evaluation is that the numerical setup and the discretized domains are valid.

## 4.5. Computational setup

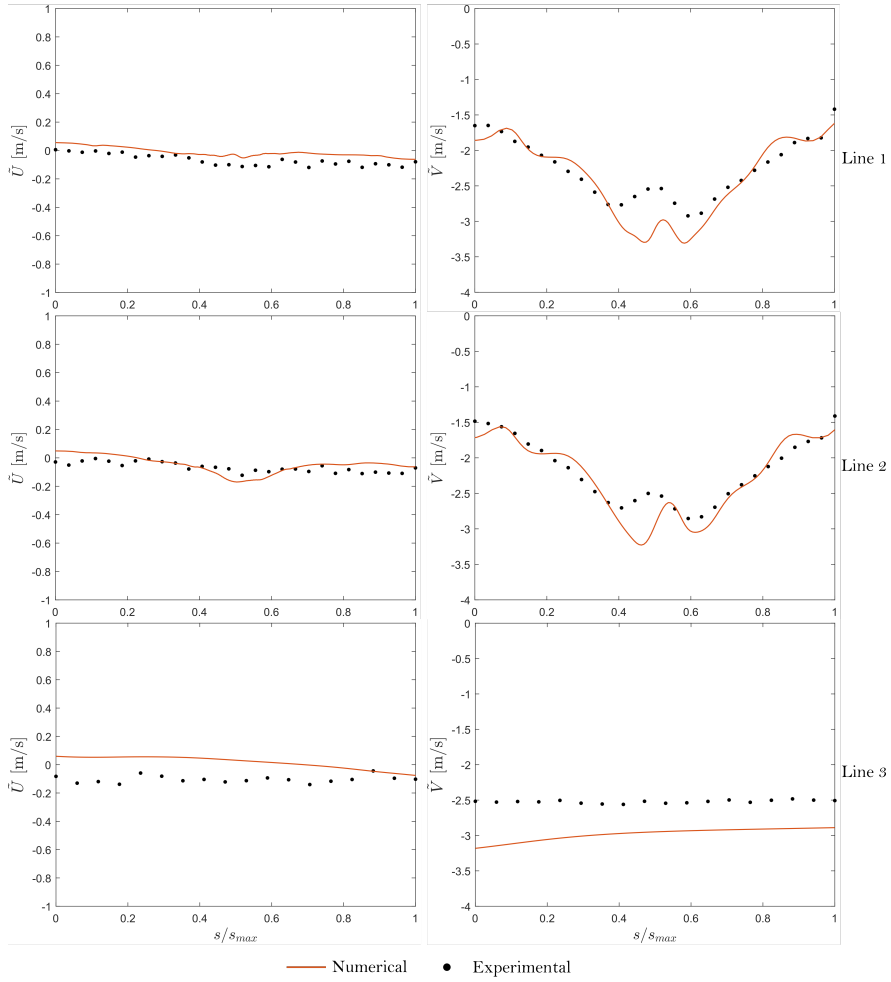


**Figure 4.7:** Numerical validation of horizontal ( $\tilde{U}$ ) and axial ( $\tilde{V}$ ) velocity components against experimental PIV measurements at BEP.

## 4.5 Computational setup

The CFD software used in this project is ANSYS<sup>®</sup> 2021 R1. ANSYS CFX<sup>®</sup> have been used to solve the governing equations. The CFX stand-alone program is divided into three sub programs, CFX-Pre, -Solver Manager

and -Post, which is case setup, calculation and post-processing respectively. Further in the text, these will be referred to as Pre, Solver and Post.

The CFD computations of the simulation cases are performed using a element-based finite volume method. The **High Resolution** is selected for the advection term and turbulence solver. This setting uses a spacial nonlinear recipe for  $\beta$  at every node based on the boundedness principles [34]. The value of  $\beta$  determines the mix of 1st Order Upwind Difference scheme ( $\beta=0$ ) and Central Difference scheme ( $\beta=1$ ), and will attempt to have  $\beta$  as close to one without introducing any unsteady oscillations. The **High Resolution** uses the following equation:

$$\phi_n = \phi_{n-1} + \beta \nabla \phi \cdot \Delta \vec{r} \quad (4.1)$$

where  $\phi_n$  is the scalar quantity value at the n node,  $\phi_{n-1}$  is the value at the upwind node, and  $\vec{r}$  is the position vector for the upwind node relative to the n'th node. By first computing  $\phi_{min}$  and  $\phi_{max}$  at each node, the algorithm will solve for  $\beta$  so that the value for  $\phi_n$  lays within the limit  $[\phi_{min}, \phi_{max}]$  [34].

For the transient term, a Second Order Backward Euler scheme was selected. A temporal analysis were made to check the sensitivity of different time steps on the turbulent time scales. Time step of  $\Delta t_1 = 1 \times 10^{-5}$  s and  $\Delta t_2 = 1 \times 10^{-4}$  s was used in the analysis. The analysis showed that the time step has significant effect on the resolution of the turbulent field. However, due to limited time, a fixed value of  $\Delta t = 2 \times 10^{-4}$  s had to be selected for the final simulations. This corresponds to  $0.4^\circ$  of runner rotation and a calculation frequency of 5 kHz. According to Salehi et al. [15], by comparing this time step frequency to the blade passing frequency of  $f_b = 166.3$  Hz calculated from Eq. 3.4, shows to be sufficient for resolving the most important flow structures and frequencies.

To reduce the calculation time, convergence control was set between 1 and 2 iterations with a residual convergence criteria of  $R_{rms} = 5 \times 10^{-4}$ . Convergence criteria set for mesh deformation was set between 1 and 5 iterations with a max residual value of  $R_{max} = 1 \times 10^{-4}$ .

Fluid properties was selected as Water for all domains, namely rotor (R), stator (S) and draft tube (DT), with a reference pressure of 0 Pa. The turbulence model was specified to SAS SST with wall function set to **Automatic**. This option uses an automatic near-wall treatment method. The method switches from wall function to a Low-Reynolds-Number method, for

resolving the details of the boundary layer profile, if the mesh is sufficiently refined near the wall. This option is recommended by ANSYS CFX<sup>®</sup> as it reduces the loss in accuracy compared to the earlier Standard Wall function model [18, 47]. More information is available in ANSYS<sup>®</sup> documentations.

The inlet boundary condition was set to **Mass Flow Rate** following a mathematical expression as described by Fig. 4.1. The flow direction, for radial and tangential velocity components only, was set to  $19.85^\circ$  relative to the tangential velocity component. Outlet boundary condition was set to opening with a total pressure of 101 325 Pa with flow direction normal to boundary. This type was selected to account for back flow due to recirculation formation/ mixing phenomena at the outlet.

For each connecting and periodic surfaces, the interface methods used were **General Connection** and **Rotational Periodicity** respectively. **Transient Rotor Stator** interface was selected for both Stator-Rotor and Rotor-DT surfaces with a specified pitch angle for each component relative to  $360^\circ$  for rotation. Connecting interfaces with equal node distribution uses 1:1 connection, where as the rest uses GGI. A complete overview of the interface setup is shown by Fig. C.10 in Appendix-C.



## Remesh architecture

*In this chapter, a transient method involving dynamic mesh and remeshing will be presented. First, the dynamic mesh method and the implementations in the software will be presented, followed by a presentation of the automatic remesh architecture designed to preserve mesh quality during simulation with dynamic mesh. At last, an overview of the remeshing performance from the shutdown simulation will be presented. This section will cover the number of remeshing that was necessary with information on interpolation error and highlighted regions with low element quality.*

### 5.1 Mesh motion strategy

During the shutdown sequence of the Francis turbine, the GVs are to be rotated from  $9.84^\circ$  at BEP to  $1^\circ$  at ML by the use of a dynamic mesh, described in Sec. 5.2. A total of four blade surfaces will rotate around three specified axis of rotation. Both the equation of motion and the coordinates for the three axis are specified through CEL expressions. For each time step, the GV will move according to the new set of coordinates,  $x_{n+1}$ ,  $y_{n+1}$  and  $z_{n+1}$ . The motion equations can be specified as following:

$$x_{n+1} = [(x_n - x_0) - \tilde{x}] \cos \alpha_n + [(y_n - y_0) - \tilde{y}] \sin \alpha_n + x_0, \quad (5.1)$$

$$y_{n+1} = [(x_n - x_0) - \tilde{x}] \sin \alpha_n + [(y_n - y_0) - \tilde{y}] \cos \alpha_n + y_0, \quad (5.2)$$

$$z_{n+1} = [(z_n - z_0) - \tilde{z}] + z_0, \quad (5.3)$$

where  $x_n, y_n, z_n$  is the surface nodes coordinate relative to the previous time step.  $x_0, y_0, z_0$  are the coordinates for the GVs individual axis of rotation, and  $\tilde{x}, \tilde{y}, \tilde{z}$  are the total mesh displacement of each surface nodes.  $\alpha_n$  is the GV angle which is calculated at each time step by the following CEL expression:

$$\alpha_n = \omega(t_n - t_i), \quad (5.4)$$

where  $t_n$  is the current simulation time and  $t_i$  is the initial simulation time.  $\omega$  is the angular velocity of the GV, which is  $1.3^\circ \text{ s}^{-1}$ .

## 5.2 Dynamic mesh

In this present study, the inbuilt function for mesh deformation in ANSYS CFX<sup>®</sup> has been used. This is activated through the domain settings were the option of **Region of Motion Specified** have been used. The mesh motion model used in ANSYS CFX<sup>®</sup> is based on the displacement diffusion equation expressed as following [18]:

$$\nabla \cdot (\Gamma_{disp} \nabla \delta) = 0, \quad (5.5)$$

where  $\delta$  is the displacement relative to previous node location and  $\Gamma_{disp}$  is the mesh stiffness which determines the magnitude of relative movement of the nodes and are derived through available methods specified by the user.

Thorough tests have been carried out with the aim of finding the correct mesh stiffness option and model exponent that preserves the mesh quality best during shutdown. Due to high mesh refinement, it was found that the elements in the inflation layer folded during mesh motion with the use of uniform models such as a boundary proximity model or a small volume model. The method called **Blended Distance and Small Volumes** was found to give sufficient solution to the displacement diffusion equation as it uses a blending function and was selected for the final simulation. The mesh stiffness from the given methods is calculated as follows [18]:

$$\Gamma_{disp} = A \left( \frac{\nabla_{ref}}{\nabla} \right)^{C_{vol}} + B \left( \frac{L_{ref}}{\max(d, d_{wall})} \right)^{C_{dis}}, \quad (5.6)$$



where  $\forall$  and  $d$  is the local control volume size and distance from the nearest boundary, respectively. Factor  $A$  and  $B$  are weighted variables which is either indicating dominance of one term over the other, or equality.  $C_{vol}$  and  $C_{dis}$  are constants and program controlled. The remaining parameters are reference values found from the properties of the local mesh domain [18].

### 5.3 Automated remeshing

To get accurate results during the transient operation, one need to ensure high quality mesh during the whole simulation. This was made possible through a automatic remeshing system which monitors the mesh quality. The system architecture is presented in Fig. 5.1. The basic setup is as follows; when a predefined limit is reached, the solver will stop and the geometry will be modified based on the last monitored GV angle,  $\alpha_n$ . A new mesh is generated based on the new geometry which is then automatically imported into the CFX solver. The solver continues in a cycle until the simulation has finished.

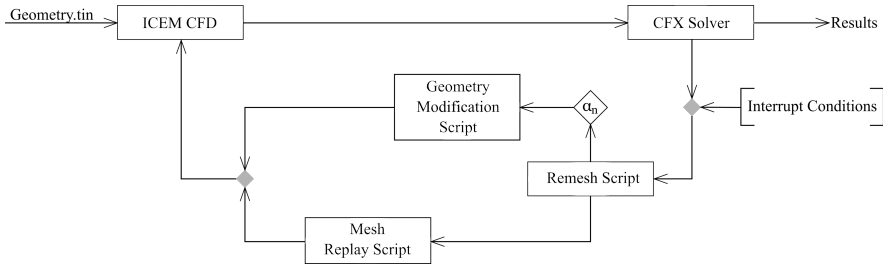


**Figure 5.1:** System architecture for automatic remeshing with ANSYS CFX<sup>®</sup> and ICEM CFD<sup>™</sup>

At first, the geometry file was imported in to ICEM CFD<sup>™</sup> as a .tin file. Then the first mesh was created using the already created replay script, and exported into CFX Pre. The option for remeshing is activated in control configuration. Then ICEM CFD<sup>™</sup> is specified with the need of three additional files. This is, the .tin file, a Mesh Replay script and a Geometry Modification script. The latter one is optional dependent on the users intention on geometry handling. Each script is presented in Appendix-D.1 and Appendix-D.2, respectively. In this present work, all files were given to the software as presented in Fig. 5.1. A monitor point for the GV angle was created and is read by the remesh script through scalar parameters extracted from the

solver. During remeshing, ICEM CFD™ is opened in batch mode and are given instructions from the two files, i.e. Geometry Modification script and Mesh Replay script. First, the GV blade surfaces are changed relative to the monitored angle,  $\alpha_n$ . Then the mesh replay file creates the mesh which is exported back to the solver. The interrupt condition criteria used is a logical expression based on the minimum value found from monitoring the orthogonal angle in the stator domain. The expression becomes true if the value of orthogonal angle is lower than the user defined minimum value. In this present work, this value was selected as  $28^\circ$  for the first five seconds of simulation, and  $22^\circ$  for the rest of the simulation. This was needed as the overall value of orthogonal angle decreased during the simulation run. The remeshing results from the final simulation is presented in Sec. 5.4.

## 5.4 Remesh interpolation

A total of 13 remeshing was necessary during the complete shutdown simulation. During the simulation, the orthogonal angle was measured as part of the mesh quality criteria used for remeshing. During remeshing, the node positions for the new mesh is compared to the old mesh. Here, unmapped nodes needs to be interpolated by using the surrounding node values.

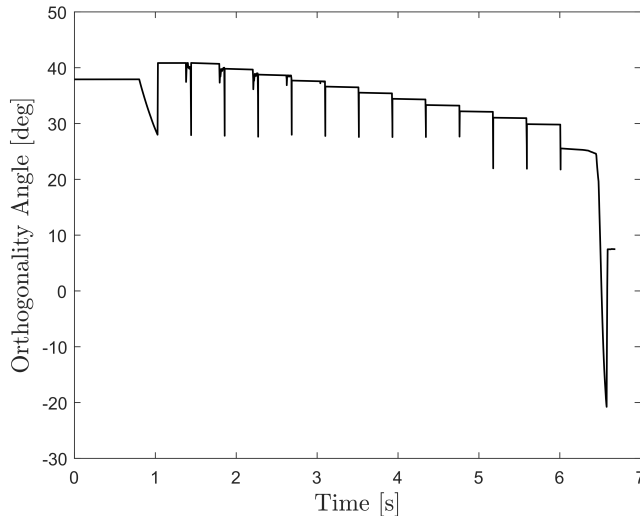


**Figure 5.2:** Orthogonality Progress during full shutdown simulation

The average percent of unmapped nodes from all remeshing was less than 1.3%, where the highest and lowest values was 1.5% and 1.1%, respectively. The two highest interpolation error was found to be 0.08133% and 0.00083%, each from monitored velocity at BEP close to guide vane LE. See complete overview from interpolation error analysis in Appendix-A.

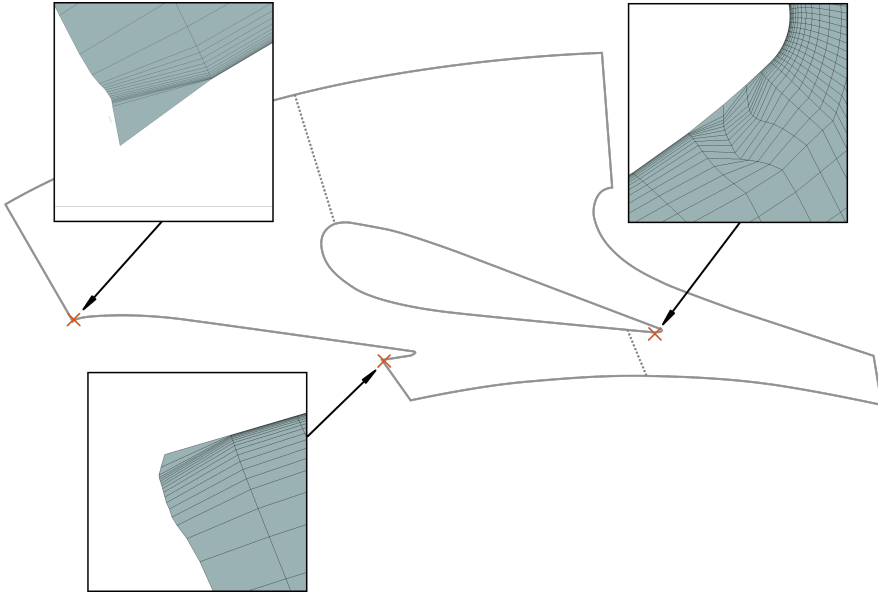


**Figure 5.3:** Three locations at upper and lower ring with reduced orthogonal quality during dynamic mesh motion.

The result for orthogonal angle is presented in Fig. 5.2 where each dip is recovered by remeshing, showing two different behaviors. For the first remeshing, a nonlinear decrease in orthogonal angle is visible which is expected during dynamic mesh motion. However, abnormal changes in the orthogonal angle can be seen for the rest. Small oscillating changes in the orthogonal angle is visible for the five proceeding sets of remeshing. A rapid decrease in orthogonal angle is observed for all cases except for the first remeshing. It was found to be caused by small number of elements in the inflation layer at both upper and lower ring boundary on three different locations shown in Fig. 5.3. Multiple tests was performed in advance to find a solution to the problem, e.g. by using other mesh stiffness method or change the mesh. The latter change reduced the likelihood of cell collapse by increasing the first cell height into the inertial sub-layer. However, it

is assumed that the cause of random node motion is due to the accumulation of numerical error from solving the displacement diffusion equation for every time iteration. Therefore, a suggested solution would be to solve the displacement diffusion equation for individual time steps independent of the selected time steps used for the fluid computations. This will reduce accumulated node position error on the expenses of solving the flow physics for a set of iterations with a fixed blade position. This is still viable as the difference in node position during, e.g. 10 coefficient loop iterations, results in only  $\Delta s = 4.6 \cdot 10^{-5}$ mm.

Due to great difficulties of remeshing for guide vane angles close to zero, it was necessary to disregard remeshing for  $\alpha < 1.5^\circ$ . This resulted in undesired levels of orthogonal angle, as low as  $-20^\circ$ , close to the end of simulation. The low value was caused by a mesh element folding of one cell near TE at upper ring boundary, shown in Fig. 5.3. At the end, the value increased back to a value of  $7^\circ$ . Orthogonality lower than  $10^\circ$  can impact the results, and will therefore not be considered in the present work.

## Results and discussions

*The results from the present work will be presented and discussed in this chapter, starting with the results on dynamic blade loading is presented for both main blade and splitter blade. Then, the vortex development and dynamics through time in the stator, rotor and draft tube domains, will be presented where the aim is to add context to the observations made on dynamic blade loading.*

### 6.1 Dynamic pressure loading

Part of the investigation of the blade loading during the shutdown sequence was to check the pressure gradient on each blade surface. Post-processing was conducted at each operating points (e.i. BEP, PL, DPL and ML) and in the time domain  $t \in [1,6]$  s. The results are presented in Fig. 6.1 and Fig. 6.2 for main blade (MB) and splitter blade (SB), respectively.

During the first four seconds, a periodic pressure gradient can be found on each blades suction side which moves towards the blades LE. At BEP, the periodic pattern on MB covers only the upper half of the blade surface, while the remaining 50% of chord length has a streamwise varying pressure gradient. Compared to SB, the periodic pattern covers the entire blade surface. These periodic pressure gradients is caused by vertical vortices which moves along the blades surface until they dissipates. More on this in Sec. 6.3. Meanwhile, a smooth streamwise pressure gradient from high levels close to LE to low levels near TE can be found on both blades pressure side.

Acquired pressure pulsations on the blades suction side is normalized using Eq. 6.1, where  $\frac{\partial p}{\partial s}$  is the measured pressure gradient in  $\text{kg m}^{-2} \text{s}^{-2}$ ,  $\rho$  is the water density at BEP in  $\text{kg m}^{-3}$ ,  $E$  is the specific hydraulic energy in J

$\text{kg}^{-1}$  at BEP, and  $L = \pi D_{r1}/z_r$  is the chosen length scale taken as the blade pitch at runner inlet,  $D_{r1}$ .

$$\tilde{p}_E = \frac{\frac{\partial p}{\partial s}}{(\rho \cdot E)_{BEP}} \cdot L \quad (6.1)$$

The highest periodic pressure gradient on the suction side was measured at PL to a value of  $5.41\text{E}+5 \text{ kg m}^{-2} \text{ s}^{-2}$ , compared to  $4.85\text{E}+5 \text{ kg m}^{-2} \text{ s}^{-2}$  at BEP. This results in pressure oscillations of  $\tilde{p}_E = 0.3$  at PL. The pressure difference on each side of the blade results in a net pressure force in runner rotational direction, of which in combination with the periodic pressure field will cause a local dynamic, oscillating load on each blade.

After four seconds of run time, large pressure gradients starts to form between 70-100% of chord length on the MB's suction side, leading to  $\tilde{p}_E = 0.63$  at ML. This is caused by stationary and oscillating vortices developed at the hub wall close to the MB's suction side as a result of flow leakage from suction side of upstream blade. Additionally, the MB pressure side is also affected by the same vortices due to the small gap between each blade. While, closer to the blades LE, smaller instantaneous stochastic vortex structures results in local regions with high pressure gradient. The pressure oscillations here was measured to  $\tilde{p}_E = 0.25$ . These vortex structures is formed due to significant flow separation from the blades LE. At PL and DPL, counter vortex from hub and shroud is causing streamlined pressure gradient in the first 30% of chord length for both MB and SB. For more information on vortex structures, see Sec. 6.3

Finally, the maximum pressure gradient is found at each blades LE and TE during the complete shutdown. This is a result of local flow acceleration and will cause significant pressure force as a result of the small area. Here the main concern would be at the TE where the blades are thin, especially during the end of shutdown with high levels of pressure gradient. However, it should be noted that part of the pressure force acting on the blades are transitioned into motion of the runner, rather than structural deformation. The amount of cyclic deformation is here unknown and Fluid-Solid Interaction simulations should be made in the future, covering the entire shutdown sequence.

## 6.1. Dynamic pressure loading

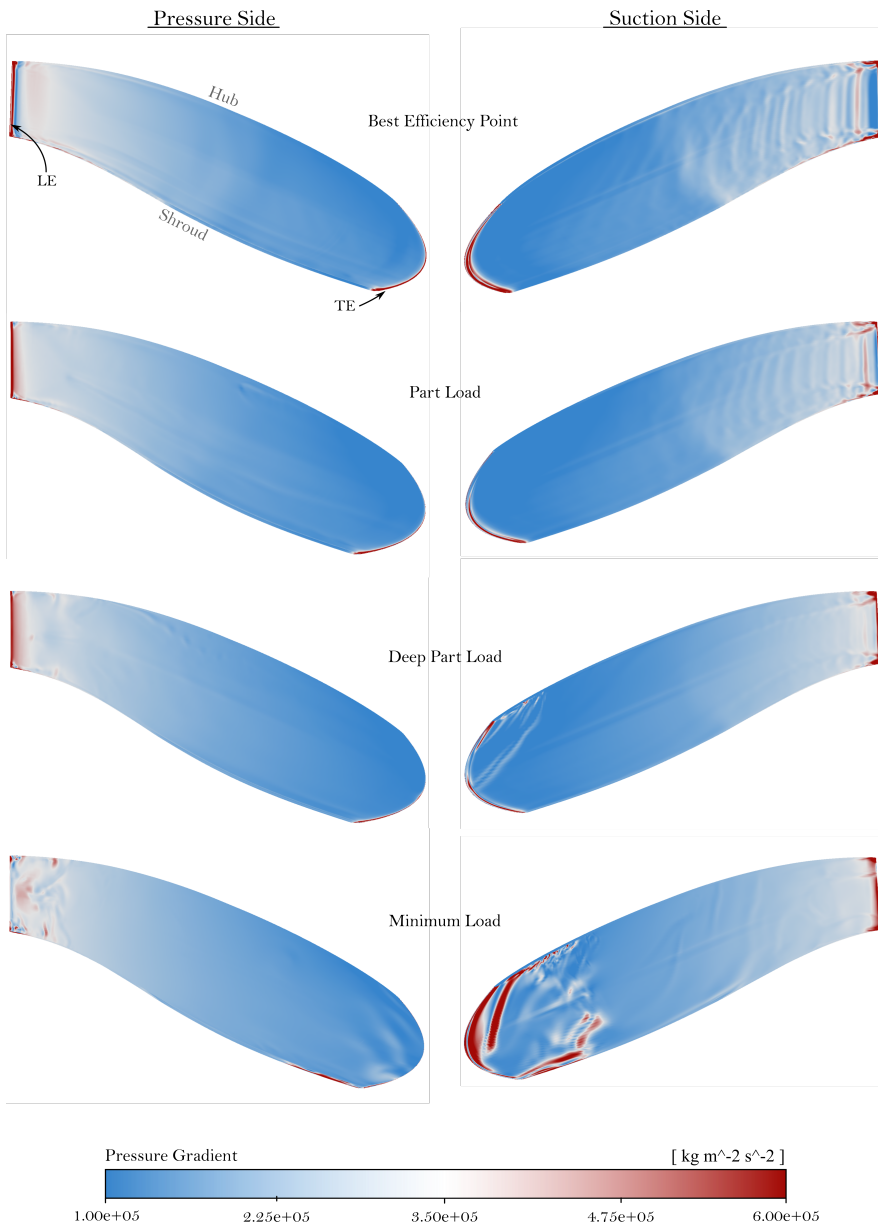


**Figure 6.1:** Pressure Gradient on Main Blade for all operating points.

## 6. Results and discussions

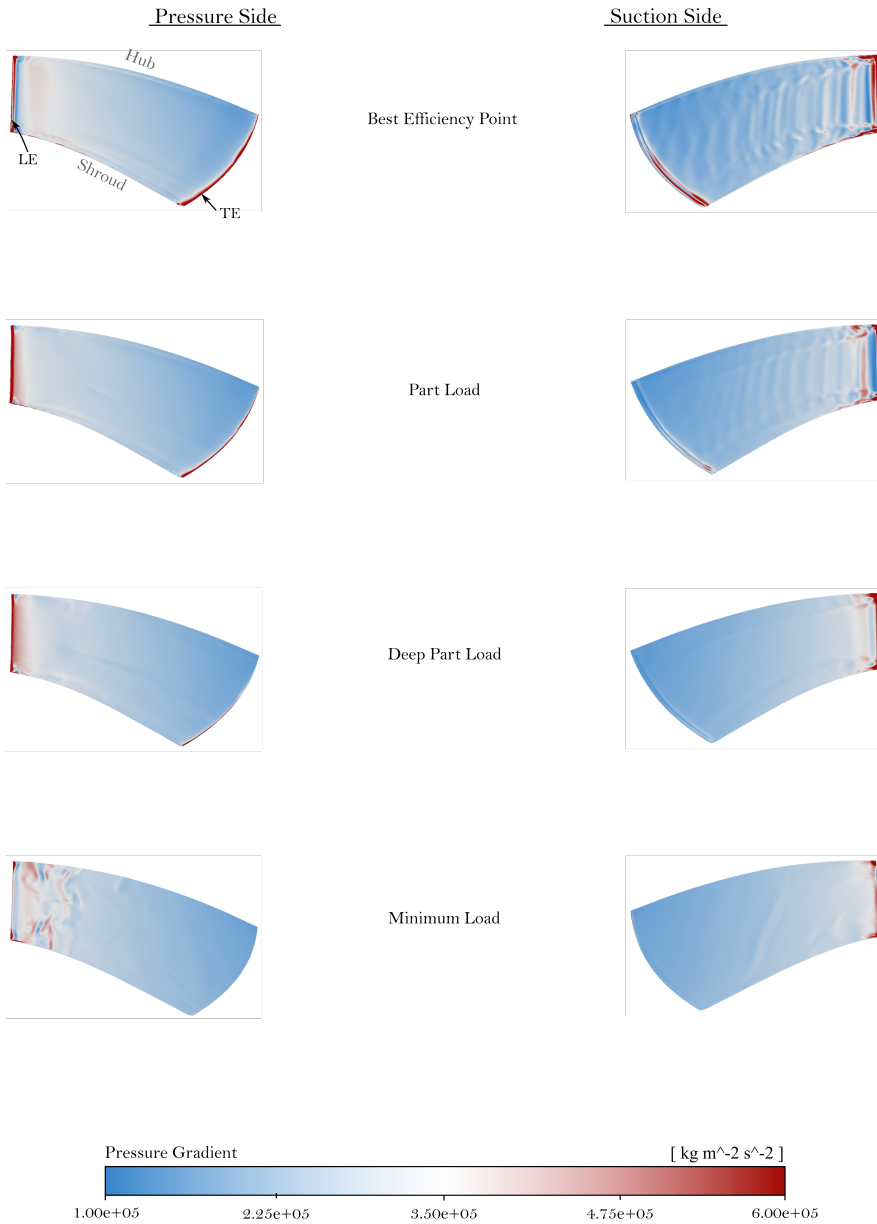


**Figure 6.2:** Pressure Gradient on Splitter Blade for all operating points.



The following sections covers in-depth analysis of vortex structure development and their dynamics during the whole shutdown sequence. The section is arranged in a structure, to the authors best, presenting important and relevant observations as time develops. A substantial amount of results have been used during post-processing to map the development and dynamics of vortex structures, of which not all can be covered in this present work. Some additional results, not presented in this section, can be found in the Appendix-E.

## 6.2 Vortex development and dynamics: Stator

This section focuses on development and dynamic of vortex structures in the stator domain. There are two regions in the domain of which produces dominant vortex structures. These are, the horseshoe vortex from GV LE, and secondary vortices from the GV TE. These dominant structures share most of the same structures during the initial four seconds. During the last four to six seconds, the small GV opening starts to impose significant changes of which affecting the characteristics of the vortices.

A single horseshoe vortex (HSV) developed between the upper/lower ring and the GV LE. Such vortex near the lower ring at BEP is presented in Fig. 6.3, of which is normalized by the guide vane leading edge radius,  $R_{G1}$ . Negligible difference in length scale and strength between the HSV at upper and lower ring was found. Therefore, the HSV near the upper ring will only be considered further on. The length scale of the HSV was roughly constant during the initial four seconds. At BEP and PL, the HSV was measured to be approximately  $d_{BEP} = 1.66$  mm and  $d_{PL} = 1.68$  mm.

The HSV developed into a passage vortex and a counter vortex. The counter vortex dissipated before reaching the GV passage during the entire shutdown sequence. On the other side, the passage vortex follows along GV suction side. It expands as it moves through the blade passage when the local pressure decreases in the streamwise direction due to flow acceleration. When the vortex reaches the GV TE, it then gets pulled towards the runner blades LE due to the low pressure field from flow accelerating near the suction side of the blade tip. The passage vortex then interacts with the runner blades, causing the vortex to split in to a new vortex segment positioned horizontally between two blades. More on this in Sec. 6.3.

The second dominant vortex structure in vaneless space is caused by vortex shedding from the GV TE. At BEP, a von Kármán vortex street

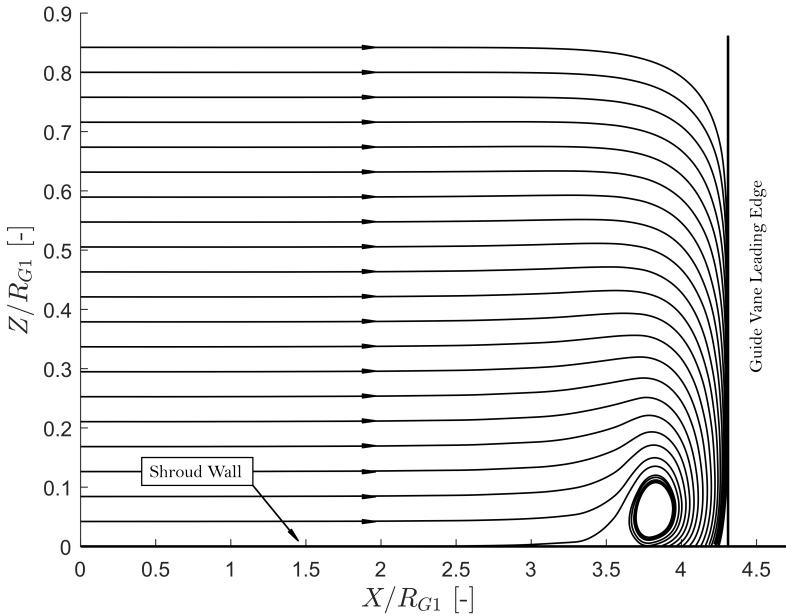


**Figure 6.3:** Streamlines of HSV near GV LE at BEP.

is formed in the wake of each GV. Results from this present work shows that the vortex street merge together a short distance behind TE, forming one long vertical structure. This merging is likely caused by low temporal resolution, as the vortex street persisted over a longer distance in earlier simulations with higher temporal resolution. Therefore, the behavior of the vortex street should be analysed closer with sufficient temporal resolution as the vortex structures are directly connected with structures developing on the runner blades suction side, causing the pressure gradient pattern shown in Fig. 6.1 and Fig. 6.2.

After one second, a line vortex develops from the GV LE and along upper and lower ring. These structures are growing as the guide vane moves and the flow accelerates, causing the local pressure to decrease. This is likely caused by the viscous wall effect from the three surfaces (GV pressure side, GV suction side and upper ring) and stagnant flow with high pressure, increasing the vorticity leading to a line vortex. However, this should be investigated further to verify, as this structure is the most dominant structure in the vaneless space and runner channel as time increases.

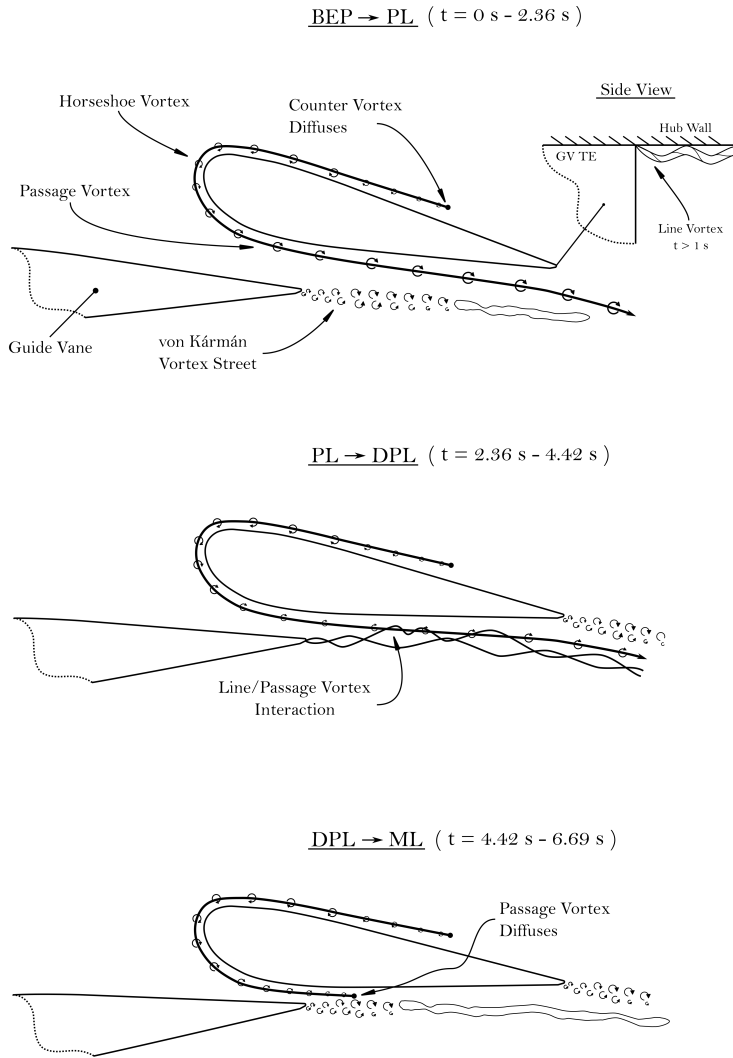


**Figure 6.4:** Dominant vortex structures from guide vanes in the vaneless space.

For time,  $t = 1-4 \text{ s}$ , the passage vortex decreases in size as it being stretched due to the small gap between each blade. The velocity of the flow in the blade passage increases, which causes the passage vortex to mix with

the line vortex developed at both upstream and downstream GV TE. The vortex street gets stretched, causing more merging and larger structures. At last, the line vortex near upper and lower ring expands as some of the kinetic energy from the passage vortex is transferred to the vortex during mixing.

The line vortex is more dominant than the passage vortex, during the last one to two seconds of the shutdown sequence. The horseshoe vortex at DPL and ML was measured to be  $d_{DPL} = 1.1$  mm and  $d_{ML} = 0.94$  mm, respectively. Meaning the HSV is about 34-43% smaller compared to the structure at BEP, and results in a smaller passage vortex. Moreover, the thin gap compresses the passage vortex, increasing the, translational kinetic energy of which eventually, near six seconds, leads to a rapid dissipation in the blade passage. Additionally, the long structures of the vortex street is merging with the line vortex, increasing the structural size of the line vortex.

As time progresses, the overall dynamic of all structures in the vaneless space can be summarized as follows; The mixing of all structures increases as the guide vanes are closing. Moreover, the structures are present in the vaneless space over a longer time as the flows angle of attack, relative to runner blades, decreases. Leading to smaller amount of each structures being extracted into the runner channels. This is evident from Fig. 6.1 and Fig. 6.2, as the periodic pattern of pressure gradient on suction side decays as time reaches four seconds.

### 6.3 Vortex development and dynamics: Rotor

This section focuses on the vortex path and dynamic of vortex structures in the runner. Major part of the structures found in the runner channel are structures developed from the stator domain. There are two dominant structures forming near the runner inlet during the initial four seconds. After three seconds, stationary vortices are forming near MB TE, of which grows into larger structures at ML. Additional stochastic structures are also formed close to the runner LE due to significant flow separation. The details of the each structure will be covered in the following way, in the preceding paragraphs.

As mentioned, two dominant structures are present in the blade channel during the initial four seconds. By observations, both structures are presented in Fig. 6.5 and Fig. 6.6.

A deterministic, horizontal channel vortex develops mainly from the GV

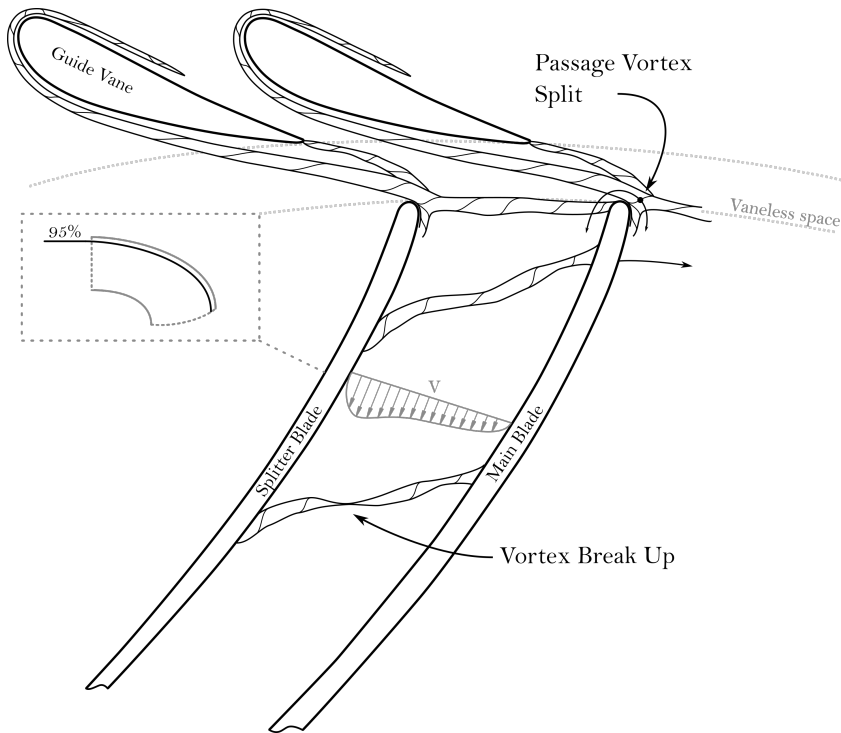


**Figure 6.5:** Dynamics of horizontal vortex structures from guide vane passage vortex, on 95% of blade span at BEP.

passage vortex, and a mix of line vortex from GV TE as seen by Fig. 6.5. The flow on each side of the RN blades splits the passage vortex, where the new horizontal vortex segment enters between two runner blades. A suction effect constrains the right part of the vortex to the pressure side of the blade, while the other end continues along the blades suction side.

These results show that a periodic vortex pattern develops in each blade channel with a frequency equal to the guide vane excitation frequency,  $f_s$ . Furthermore, the vortex segment moves downstream while being stretched due to the velocity gradient across the blade channel. Ultimately, the segment splits in two and dissipates due to viscous effects in the turbulent boundary layer close to hub and shroud. The average length scale decreases as time advances, producing large unstable and stochastic structures. This is caused by the GVs decreasing angle of attack, where smaller portions of the

upstream vortices enters the blade channel.

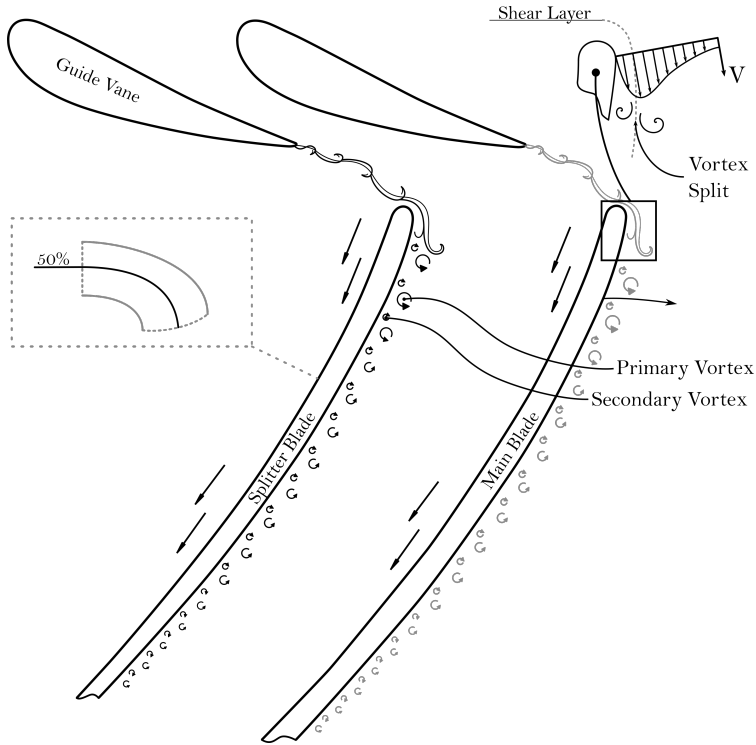


**Figure 6.6:** Dynamics of vertical vortex structures from guide vane vortex shedding, on 50% of blade span at BEP.

The second dominant structure is a set of vertical structures along the runner blades suction side. These are formed as the guide vane TE vortex street are interacting with runner blades LE. A shear layer is present due to the high velocity gradient near LE, causing the upstream vortex structure to split into two independent vortex pairs, here denoted as primary and secondary vortex. The primary vortex contains the bulk kinetic energy from the upstream initial vortex where as the secondary vortex is smaller and travels closer to the blade suction side. Due to the high velocity gradient near LE, the secondary vortex pair is shifted further downstream of the primary vortex pair. This is evident from the pattern of the pressure gradient, visible on the blade suction side (Fig. 6.1-6.2). Initially, both structures are continuous in shape over the blade span. The vortex pair, moving along

MB suction side, breaks up into smaller segments which ultimately interacts with the MB TE vortex street and moves into the draft tube. The vortex pair along SB suction side are still continuous as they mixes with the SB TE vortex street forming both larger and smaller vortices, which eventually enters the draft tube.

Meanwhile, on the pressure side of all blades during the initial four seconds, the flow in 50% of blade span is streamwise smooth with no periodic vortex structures. The RN passage vortex is insignificant in size during the first few seconds. This is due to the presence of the horizontal vortices. However, as the horizontal vortices abates over time, the passage vortex starts to grow into a dominant structure. This yields for both the main blade and the splitter blade. After three seconds, the passage vortex close to hub and shroud splits, forming an additional structure at 50% of blade span. See Fig. E.4 in Appendix-E. If observing closely at Fig. 6.1, the passage vortex at hub/shroud and the mix at mid-span, is shown by the pressure gradient on the pressure side of MB at PL. Additionally, the counter vortex starts to grow into a dominant structure between PL and DPL, which is visible from Fig. 6.1-6.2.

The horseshoe vortex generated at the runner blades LE is small compared to the GV HSV. The vortex was single in form during the entire time, and with a length scale of approximately  $d_{BEP} = 0.5$  mm and  $d_{PL} = 0.66$  mm at BEP and PL, respectively. The length scale at DPL was the same as at PL, however, the length scale at ML was measured to approximately  $d_{ML} = 0.89$  mm at the hub, which is larger compared to the other operating points. More specifically 48% and 78% larger compared to DPL and BEP, respectively. Additionally, it was found that the HSV structure at hub and shroud had different length scales. The structure at hub was larger as a result of changes in the local velocity field by the surrounding vortex structures as seen in Fig. E.6 in Appendix-E. Vortices with higher kinetic energy, extracts portions of the HSVs kinetic energy, changing their length scales in the instantaneous time frame.

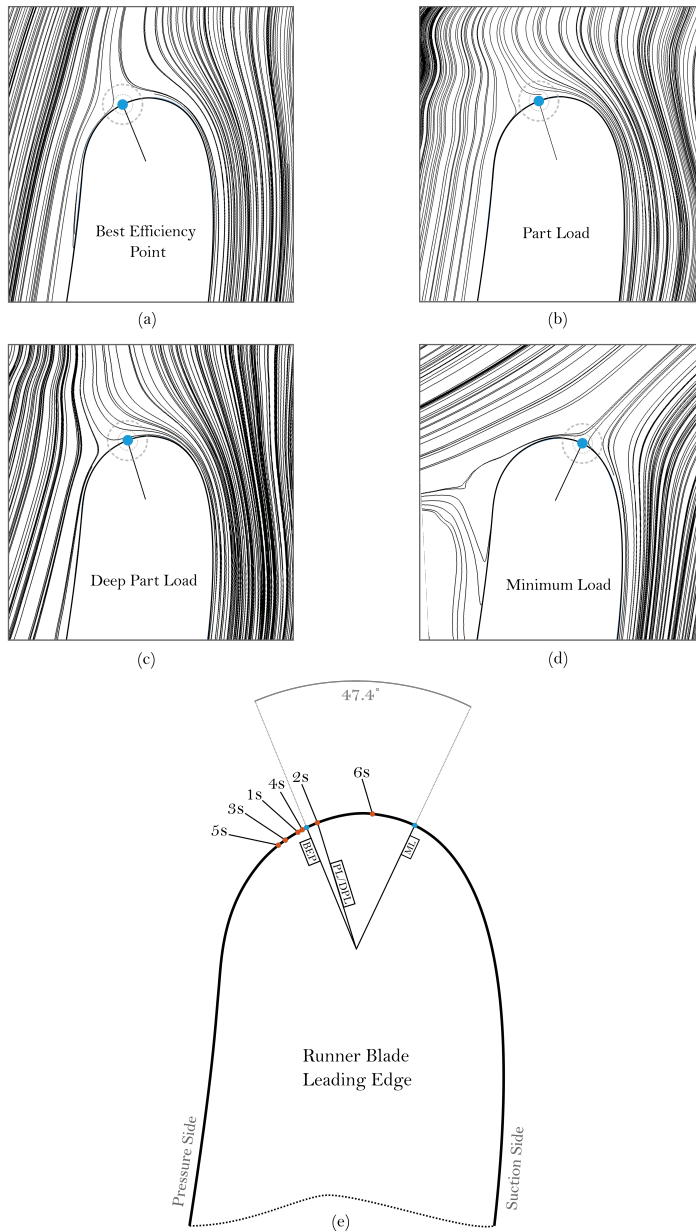


**Figure 6.7:** Time development of runner blade stagnation point with streamlines showing flow path at each operating points. (a) best efficiency point, (b) part load, (c) deep part load, (d) minimum load and, (e) total time overview.



The time development of the runner blade stagnation point was studied closer, and the results are shown in Fig. 6.7. As seen in Fig. 6.7(e), the stagnation point oscillates back and forth in the first five seconds. This is likely a result of transient effects in the flow field from the vortex street in the vaneless space, as a consequence of vortex shedding at the GV TE. After five seconds, the stagnation point moves from pressure side to suction side, which is expected when the guide vane angle reduces. The angle between initial and final stagnation point was around  $47.4^\circ$ . From Fig. 6.7(a)-(c), shows that a higher content of the incoming flow is transferred to the suction side due to the low pressure field. As a result, the vortex structures interacting with the blade tip will split in two, with a larger portion of the structures being transported to the suction side. Thus, in close agreement with the results found on the vertical vortex pair observed only along the suction side.

As seen from Fig. 6.1 and Fig. 6.2, large area with high pressure gradient near MB TE is formed between DPL and ML. These high values are caused by multiple vortex structures ranging in different length scales. At BEP the flows specific kinetic energy in the runner is in equilibrium with the angular kinetic energy of the runner. Meaning, the flow exiting the runner is largely axial. However, during shutdown, the discharge is decreased while maintaining constant flow area in the runner channel and angular rotation. The specific kinetic energy of the flow reduces, leading to an energy imbalance between the flow and the runner, causing a whirl velocity component,  $c_{u1}$  in the opposite of rotational direction relative to the stationary frame of reference. The increase in whirl velocity causes the pressure normal to the meridional plane to rise. A relatively high pressure gradient develops after DPL in the opposite flow direction at about 95% of blade span. This causes a change in flow direction from one suction side to the other, as seen in Fig. 6.8 and Fig. 6.9. Flow propagates upstream until the pressure reaches a higher magnitude, causing the flow to turn back again. This effect is initiated around DPL, as seen from the pressure gradients seen from Fig. 6.1 and Fig. 6.2, and for reduced discharge towards ML, the higher upstream the flow propagates.

As a consequence, a large spiral vortex is formed curling around the MB TE from hub to mid-span. See Fig. E.5 in Appendix-E. The velocity gradient along suction side, as described in Fig. 6.9 causes the spiral vortex to break into smaller stationary vortices situated along suction side. These structures are formed at the hub wall and propagates along the span length of each MB, before entering the draft tube. It was found that these structures was mixing with large accumulated vortex structures in the vicinity of runner outlet at ML. Whether these accumulated structure are a product of the spiral vortex

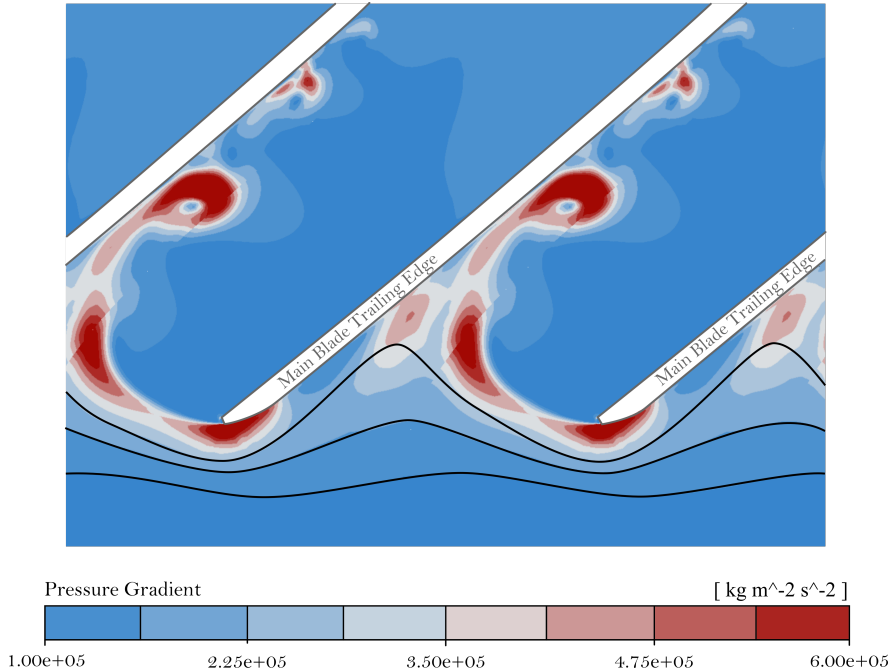


**Figure 6.8:** Pressure gradient around main blade trailing edge at ML with pressure isolines, on 5% blade span.

or structures from the RVR was difficult to judge from the available data. This should therefore be investigated closer, as the total amount of vortex structures causes the high level of pressure gradient around MB TE and eventually significant blade loading.

High values of pressure gradient was found near both blades LE at ML, caused by significant flow separation. The flow separation do not occur until after  $t = 4.5$  s, which is beyond DPL. At ML, the flow separated more from SB compared to MB. The onset of flow separation on MB takes place between 25-75% of blade span, where as for SB, the flow separates over the entire blade. The location of adverse pressure gradient was found a short distance from LE on the pressure side on both blade types. Through closer investigation, no connections could be drawn on flow separating more from the SB. Meaning, the amount of flow separation is likely to be dependent on local flow condition, such as near-field vorticity and angle of attack of incoming flows. Moreover, the separated flow develops into large stochastic

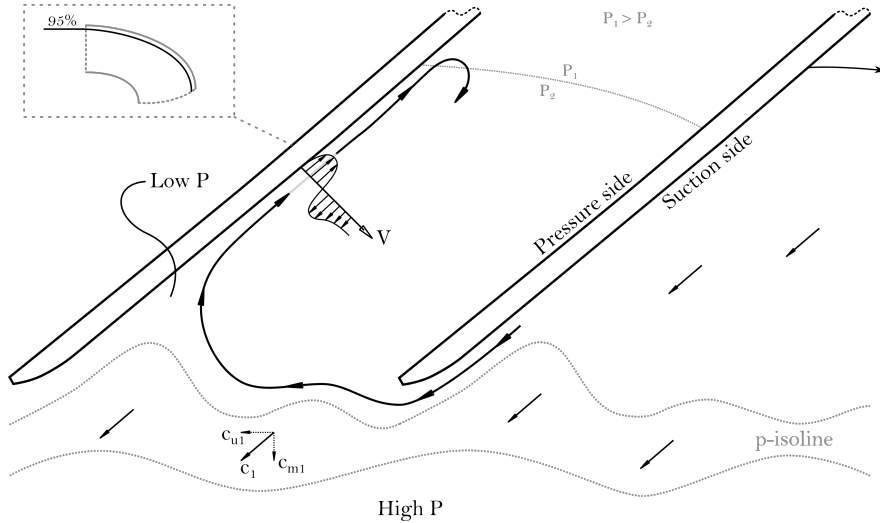


**Figure 6.9:** Flow condition near main blade trailing edge at ML. Here  $c_1$  is the absolute runner outlet velocity,  $c_{u1}$  is the whirl velocity component and  $c_{m1}$  is the axial component.

vortex structures which is the source of the high pressure gradient values found on the LE of runner blades. The fluctuating pressure gradient across the blade will cause dynamic blade loading, which over time, will result in fatigue mechanical failure of the blade.

Through the shutdown sequence, the overall dynamics of structures in the blade channel can be summarized as follows; during the initial four seconds, periodic vortex structures can be found in the upper part of the blade channel, on the suction side of both MB and SB. These are vertical structures spanning from hub to shroud and divides into a primary and secondary vortex. The frequency summation of primary and secondary vortices should add up to the vortex shedding frequency, neglecting any losses during vortex split. Additional horizontal vortices from mainly the GV passage vortex was found, spanning between two blades. The entry frequency of the vortices is equal the guide vane passing frequency,  $f_s$ , which breaks up and diffuses around 50% of MB chord length. Meanwhile, in the lower part of the blade channel around MB TE, the flow is streamwise smooth with increasing whirl velocity component as discharge reduces. Passing DPL, a large spiral vortex is forming at MB TE of which increasingly produces additional stationary vortices approaching ML. The stationary vortices are situated at hub near

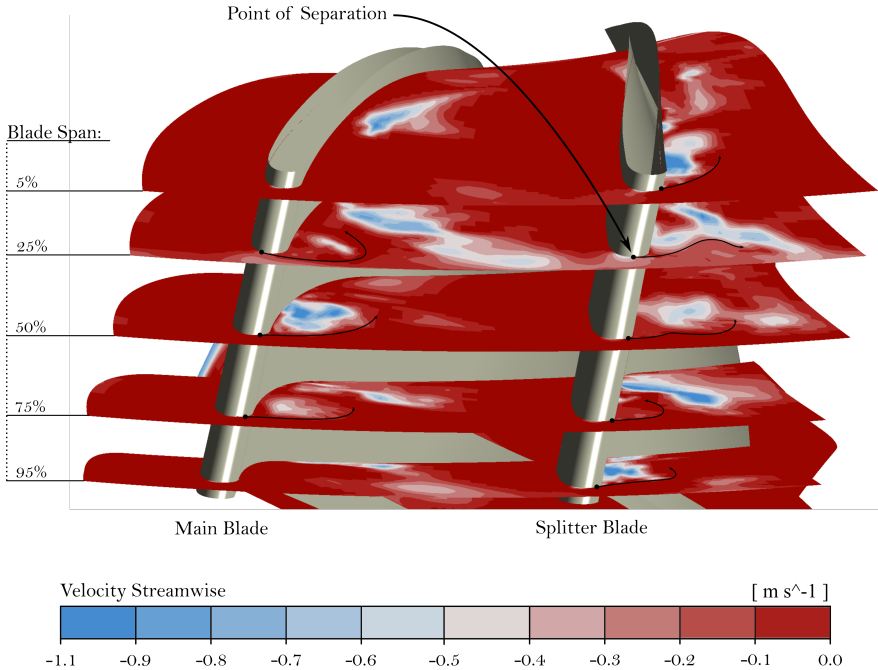


**Figure 6.10:** Overview of flow separation on main blade and splitter blade leading edge at ML.

MB suction side and propagates along side the blade surface, exiting into the draft tube at around 50% of blade span. At ML, large stochastic structures were found at the upper part of the blade channel on each blade's pressure side. These structures were caused by significant flow separation at the LE as a result of local flow conditions. These observations are in close agreement with visual observation of high pressure gradients on the blade's surface, with patterns indicating both deterministic and stochastic vortex structures.

#### 6.4 Vortex development and dynamics: Draft Tube

This section focuses specifically on the development of vortex structures around the runner cone and in the vicinity of runner blades due to the presence of a rotating vortex rope (RVR) in the draft tube. Much of the phenomena around the RVR is well covered in the literature [48, 49] and will

therefore not be included in the present work. However, some of the in-depth analysis presented in this section could shed light on new information regarding the development of the RVR during load reduction.

In previous literature, it has been found that structures in the draft tube in the vicinity of the runner blades can cause additional blade loading. Large vortical structures from each MB are mixing with structures found in the draft tube inlet, as mentioned in Sec. 6.3. Therefore, an in-depth analysis has been made to find out the cause of additional vortex structures in close proximity to the MB TE.

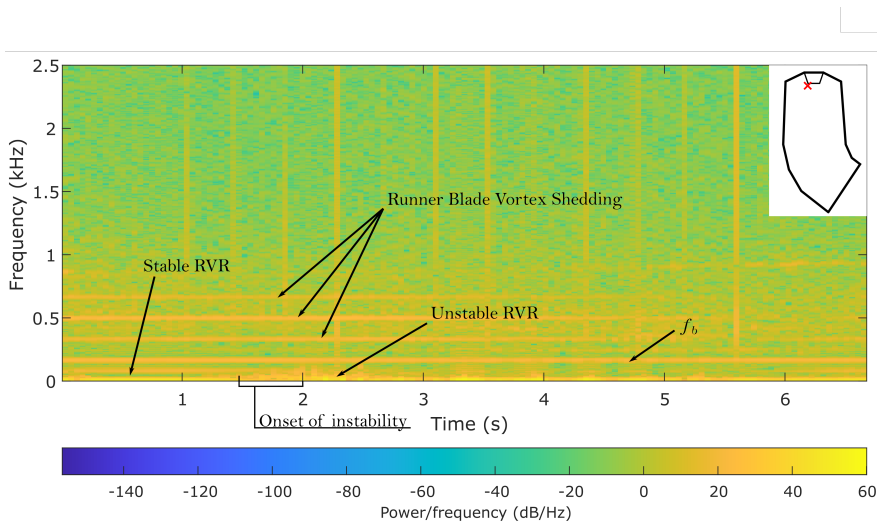


**Figure 6.11:** Frequency analysis of monitor point, DTF1, in draft tube by the use of spectrogram during the entire shutdown sequence.

As seen from Fig. 6.12, a large and unstable RVR has formed in the draft tube situated directly on the runner cone surface. Initially, at BEP, the RVR is stable and conformed underneath the runner cone due to what seems to be a near uniform axial flow field in the draft tube inlet area. This means that between BEP ( $t = 0$  s) and PL ( $t = 2.36$  s), the RVR is propagating upstream along side of the runner cone. From a STFT analysis, it was found that within  $t = 1.6 - 2$  s into the shutdown sequence, the RVR starts to become unstable. This is presented through a spectrogram in Fig. 6.11 in the marked region. The power spectra shows significant levels around  $t = 2.36$  s (PL) which indicates that the RVR has become unstable. These measurements are taken from the DTF1 monitor point which is situated

underneath the runner cone, close to its corner. See Fig. B.2 in Appendix-B for monitor point overview.

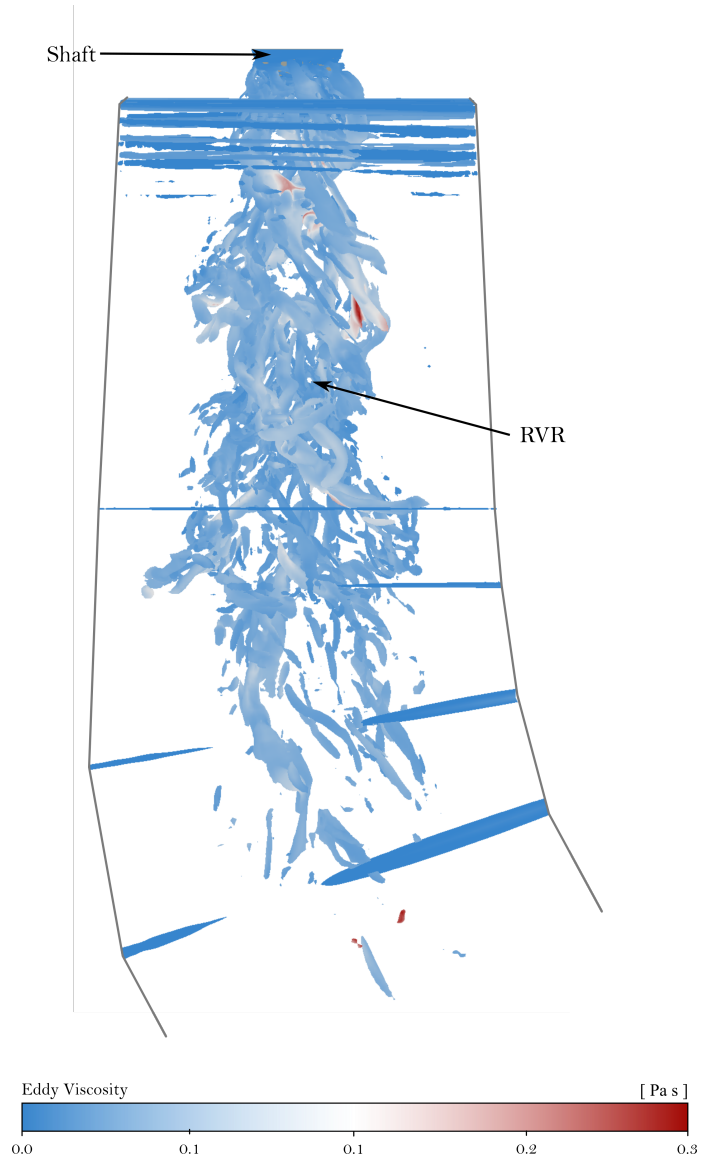


**Figure 6.12:** Rotating vortex rope in the draft tube at PL.

To understand why the RVR becomes unstable, an offset surface of 0.1 mm from the runner cone was made to analyse the flow field closer. The results are presented with streamlines in Fig. 6.13 (a)-(d), where the upper row is the runner cone from side view and the lower row is bottom view of the runner cone. Stable streamlines from the runner outlet and along the runner cone was found for  $t = 1.4$  s and  $t = 1.9$  s. However, at  $t = 2.0$  s, unstable streamlines indicates a positive axial flow component which ultimately led to a recirculation pocket. This recirculation pocket is the first sign of an unsymmetrical RVR, which is shown by Fig. 6.14. Moreover, for  $t = 2.2$  s, two unstable zones was observed, shown in Fig. 6.13(d). From these results, it has been found that the unstable streamline pattern is in strong correlation with the vortex formation underneath the runner cone.

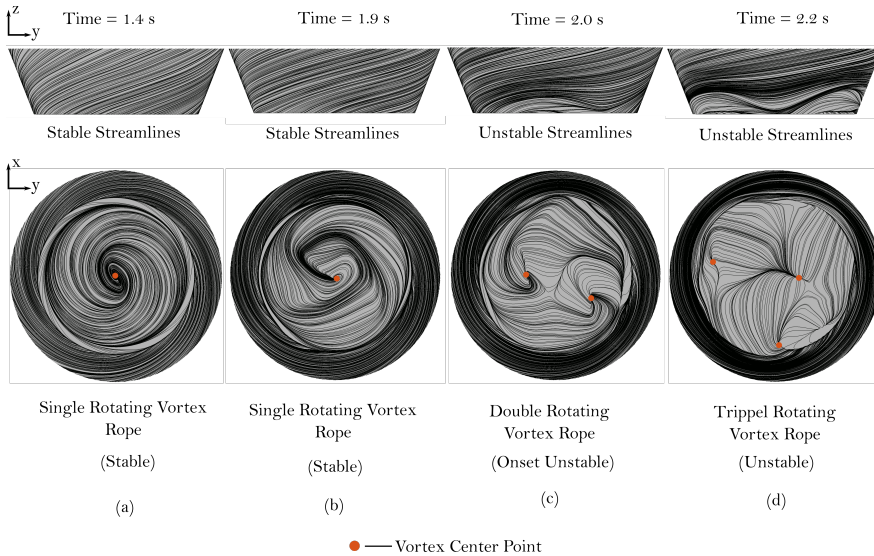


**Figure 6.13:** Comparison of flow condition around the runner cone for different timestamps

A single centered vortex rope can be found for  $t = 1.4$  s and  $t = 1.9$  s, which is shown by Fig. 6.13(a) and (b). The vortex center point is marked in orange. At  $t = 1.9$  s, the single vortex starts to move in small circles in the  $xy$ -plane as a result of higher centrifugal effect when reducing the discharge, and eventually the vortex rope break into two smaller vortex ropes at  $t = 2.0$  s. This can be seen from Fig.6.13(b) and (c). The double vortex rope has lower energy which causes them to alter positions in a chaotic dance. As one

of the vortices moves closer to the runner cone corner, leads to a reduction in the local pressure field, creating a small flow gate underneath the runner cone. Eventually, the flow through the gate mixes with the freestream on the other side, making the flow unstable and creates a recirculation pocket.

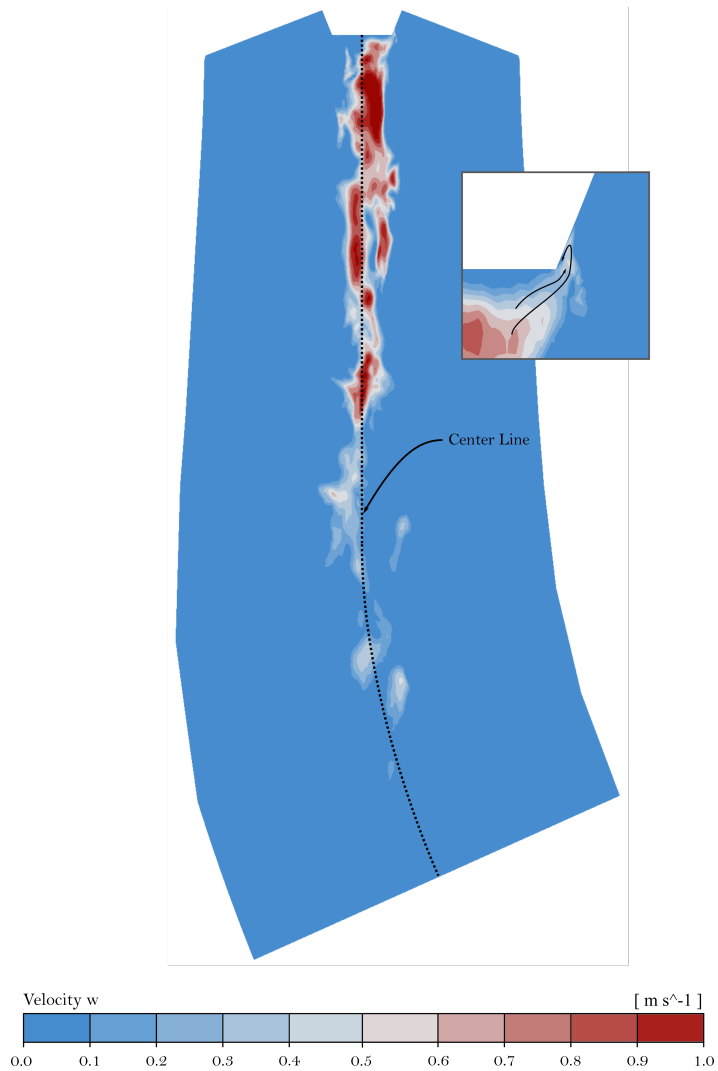


**Figure 6.14:** Unsymmetrical RVR observed at  $t = 2.0$  s showing one recirculation pocket on runner cone side.



At  $t = 2.2$  s, three vortex ropes can be observed from Fig. 6.13(d), where the vortices closest to the runner cone corner causes two unstable recirculation pockets. From this point on, towards ML, the vorticity along the runner cone side increases and the vortical structures from the RVR propagates upstream, closer to the MB TE.

Now the question is, what causes the single RVR to break into two smaller vortices. Unfortunately, the solution output frequency was not sufficient enough in this present work to be able to analyse the vortex breakup closer in time. The only data available was the timestamps presented in this section, meaning further investigation should be made. However, two suggestions to the break up is presented, as follows; the centrifugal force in the xy-plane becomes predominant compared to the axial momentum of the flow, causing the larger vortex rope to break up into smaller structures with additional energy losses. Or, the pressure oscillations from the runner blades vortex shedding causes an unstable pressure field of which is interfering with the rotational dynamics of the single, and somewhat unstable RVR, causing it to break up. There could also be a combination of both phenomena. With respect to the last suggestion, contours of the pressure oscillation is shown in Fig. E.7 and Fig. E.8. The three upper lines marked in the spectrogram, in Fig. 6.11, is likely the vortex shedding frequency of the runner blades as the lines fading out close to DPL where the main blade separation occurs. Here, the strongest line in the middle would be from the MB TE. However, this has yet been verified as there are no transient data available in the runner passage. Only the time averaged pressure field is covered from monitor point R1-R4. Therefore, a closer investigation should be made in the future.



## Conclusions

In this master thesis, a complete numerical simulation of a Francis turbine during start-stop operation was conducted using computational fluid dynamics. The aim was to investigate the dynamic blade loading of the Francis-99 runner with specific emphasize on turbulence phenomena near interfaces. The SAS SST  $k - \omega$  turbulence model was selected with sufficient mesh refinement to exploit the models potential to capture larger scale eddies.

A Grid convergence index study showed low values of discretization error, both locally and globally. Two validations methods were used to ensure credible results. Validation of pressure and turbine performance showed acceptable values of relative error. Second validation was through comparison of PIV measurement, showing close agreement with experimental data. The overall validation satisfies the level of accuracy for the present work. Automatic remesh architecture was designed to ensure adequate mesh quality during dynamic mesh motion. Interpolation error related to remeshing is at an acceptable level. Three critical mesh locations was found causing the need of 12 remeshing which is a result of small elements with high aspect ratio in the inflation layers. However, no solutions was found during testing which should be examined in future work to reduce the amount of remeshing, and hence the total error from interpolation.

The analysis of the blade loading leads to the following conclusions: In the beginning of the shutdown sequence, between best efficiency point and deep part load, dynamic blade loading is localized at the blades upper part as a result of periodic and oscillating pressure gradient moving along the blades suction side. The pressure pulsations are caused by deterministic vortex structures found in the upper part of blade channel. These structures are periodic in form and believed to be in strong correlation with the guide vane passing frequency and the vortex shedding frequency from the guide

vane trailing edge. However, this is yet to be confirmed, and need to be investigated in the future. Moreover, the highest pulsation was found on suction side close to the leading edge at part load.

During the shutdown, the blade loading is partly shifted to the blades lower part as a result of guide vane closing. The amount of periodic vortices present in the channel reduces while Passage and Counter vortex structures becomes predominant. Additional high levels of pressure gradient situates near leading edge on each blades pressure side as a result of flow separation formed around minimum load. However, the most substantial loading found during the shutdown was at minimum load close to main blade trailing edge. The high pressure gradient at suction side is caused by a large spiral vortex formed at each main blade trailing edge of which is divided into smaller stationary vortices, and possibly a mix of vortex structures propagating upstream from the rotating vortex rope. It is difficult to arrive at any conclusions with regard to additional structures from the rotating vortex rope due to the selected solution output frequency. However, it was found that recirculation pockets along the runner cone side causes the rotating vortex rope to propagate upstream closer to the blades trailing edge. Closer investigation revealed that the creation of recirculation pocket is in strong correlation with the rotating vortex rope formation underneath the runner cone. During the shutdown sequence, the rotating vortex rope splits into smaller unstable vortices of which produces a flow gate underneath the runner cone. This results in an unstable flow condition around the runner cone side, producing recirculation pockets. Detailed investigation on the additional vortex structures from the rotating vortex rope is needed.

Overall, these findings implies that low level oscillating pressure force acts on the blades upper part in the first phase. While, in the last phase, large stochastic pressure forces acts on the lower part. The loads are highest at trailing edge where the blades are at its thinnest. Therefore, it can be concluded that the blade loading will ultimately lead to fatigue damage after certain amount of shutdowns, and failure will most likely append at trailing edge before leading edge.

---

## Chapter 8

---

### **Future work**

For future work, one should investigate the cause of reduced element quality in the inflation layer during dynamic mesh motion. Here the goal is to reduce the amount of remeshing necessary during the shutdown simulation. This is to reduce the amount of error with respect to grid interpolations. One should also investigate the time-space resolution within reasonable time limits. Meaning, smaller time steps to increase the temporal resolution which will aid the purpose of getting better solutions to the turbulent flow field inside the turbine.

It was found through the present work that a line vortex develops from the guide vane trailing edge and the hub or shroud. A closer investigation into this vortex phenomena will be needed to try to mitigate the development in the future. This will reduce the overall vortex dynamics in the runner channel and interaction with other structures in the vaneless space, such as the passage vortex.

Another important aspect of the flow field is the horseshoe vortex developed from the guide vanes. Here, the goal is to either reduce the size of the horseshoe vortex, or completely remove it by implementing geometric or flow control solutions. This will reduce the size of the dominant passage vortex of which propagates into the runner channel.

With respect to the vortex shedding from the guide vane trailing edge, one should continue the research to reduce the amount of separated flow causing the vortex street. This will reduce the periodic pressure oscillations on the runner blades suction side and ultimately reduce the dynamic load on the blades over time. Here, it could be of interest to measure pressure pulsations along the suction side of both main blade and splitter blade separately. This to check if there are any correlations between the pulsation frequency from

the vortex pair and the vortex shedding frequency. And to find out the amount of energy loss due to the vortex split. It should be assumed that the sum of frequency of both primary and secondary vortex should add up to the vortex shedding frequency. However, this has to be investigated further.

In the present work, it was found additional structures close to the main blade trailing edge, mixing with the stationary vortices. These are believed to come from the RVR structure in the draft tube. Here, it will be interesting to investigate closer in time the formation of the RVR and its influence upstream with respect to additional blade loading. It will therefore be important with high temporal resolution as the structures are assumed to be small in both time and length scale.

The closer investigations into the flow leakage from the main blades trailing edges is necessary to be able to find solutions which will reduce the blade loading from production of large and stationary vortices. One need to study measures to reduce the possibility of the flow leakage into the second blade channel by maintaining the specific kinetic energy of the flow out of the blade channel while discharge is reduced. One such solution could be to adjust the cross sectional area of the runner blades outlet by closing the main blade trailing edge gap. This will maintain the specific kinetic energy of the flow while discharge is reduced and runner angular speed is constant.

---

## References

- [1] (NVKS), N. H. C., n.d., “Francis-99,” Norwegian Hydropower Centre, <https://www.ntnu.edu/nvks/francis-99>
- [2] Unterluggauer, J., Sulzgruber, V., Doujak, E., and Bauer, C., 2020, “Experimental and numerical study of a prototype Francis turbine startup,” *Renewable Energy*, pp. 1212–1221.
- [3] Xun, Z., Wanjin, H., and Zhiqiang, L., 2005, “Experimental investigation of energy loss in straight and bowed cascades with aft-loaded profiles,” *Heat Transfer—Asian Research*, **34**(2), pp. 108–119, Publisher: John Wiley & Sons, Ltd.
- [4] Takeishi, K., Matsuura, M., Aoki, S., and Sato, T., 1990, “An Experimental Study of Heat Transfer and Film Cooling on Low Aspect Ratio Turbine Nozzles,” *Journal of Turbomachinery*, **112**(3), pp. 488–496.
- [5] Sorknæs, P., Andersen, A. N., Tang, J., and Strøm, S., 2013, “Market integration of wind power in electricity system balancing,” *Future Energy Systems and Market Integration of Wind Power*, **1**(3), pp. 174–180.
- [6] Hell, J., 2017, “High flexible Hydropower Generation concepts for future grids,” *Journal of Physics: Conference Series*, **813**, p. 012007, Publisher: IOP Publishing.
- [7] Salehi, S., Nilsson, H., Lillberg, E., and Edh, N., 2021, “Numerical Simulation of Hydraulic Turbine During Transient Operation Using OpenFOAM,” *IOP Conference Series: Earth and Environmental Science*, **774**(1), p. 012060, Publisher: IOP Publishing.

- [8] Nicolet, C., 2007, “Hydroacoustic modelling and numerical simulation of unsteady operation of hydroelectric systems,” Ph.D. thesis, EPFL, doi:10.5075/epfl-thesis-3751, [https://infoscience.epfl.ch/record/98534/files/EPFL\\_TH3751.pdf](https://infoscience.epfl.ch/record/98534/files/EPFL_TH3751.pdf)
- [9] Huth, H.-J., 2005, “Fatigue Design of Hydraulic Turbine Runners,” <https://ntnuopen.ntnu.no/ntnu-xmlui/handle/11250/241313>
- [10] Deschênes, C., Fraser, R., and Fau, J.-P., 2002, “New trends in turbine modelling and new ways of partnership,” International group of hydraulic efficiency measurement (IGHM), pp. 1–12.
- [11] Solemslie, B. W., Trivedi, C., Agnalt, E., and Dahlhaug, O. G., 2019, “Pressure pulsations and fatigue loads in high head Francis turbines,” *IOP Conference Series: Earth and Environmental Science*, **240**, p. 022039, Publisher: IOP Publishing.
- [12] Trivedi, C. and Dahlhaug, O. G., 2018, “Interaction between trailing edge wake and vortex rings in a Francis turbine at runaway condition: Compressible large eddy simulation,” *Physics of Fluids*, **30**(7), p. 075101, \_eprint: <https://doi.org/10.1063/1.5030867>.
- [13] Trivedi, C., 2021, “Study of Pressure Pulsations in a Francis Turbine Designed for Frequent Start-Stop,” *Journal of Energy Resources Technology*, **143**(8), pp. 081302–1 – 081302–19.
- [14] Trivedi, C., Cervantes, M. J., Bhupendrakumar, G., and Dahlhaug, O. G., 2014, “Pressure measurements on a high-head Francis turbine during load acceptance and rejection,” *Journal of Hydraulic Research*, **52**(2), pp. 283–297, Publisher: Taylor & Francis \_eprint: <https://doi.org/10.1080/00221686.2013.854846>.
- [15] Salehi, S., Nilsson, H., Lillberg, E., and Edh, N., 2020, “An in-depth Numerical Analysis of Transient Flow Field in a Francis Turbine During Shutdown,” *Renewable Energy*, pp. 2322–2347.
- [16] Mössinger, P., Jester-Zürker, R., and Jung, A., 2017, “Francis-99: Transient CFD simulation of load changes and turbine shutdown in a model sized high-head Francis turbine,” *Journal of Physics: Conference Series*, **782**, p. 012001, Publisher: IOP Publishing.
- [17] Nicolle, J., Giroux, A., and Morissette, J., 2014, “CFD configurations for hydraulic turbine startup,” *Earth and Environmental Science*, pp. 1–10.



- [18] ANSYS, 2021, *ANSYS CFX-Solver Modeling Guide*, ANSYS.
- [19] Melot, M., Coulaud, M., Chamberland-Lauzon, J., Nennemann, B., and Deschênes, C., 2019, “Hydraulic turbine start-up: a fluid-structure simulation methodology,” *Earth and Environmental Science*, pp. 1–10.
- [20] Dewan, Y., Custer, C., and Ivashchenko, A., 2017, “Simulation of the Francis-99 Hydro Turbine During Steady and Transient Operation,” *Journal of Physics: Conference Series*, **782**, p. 012003, Publisher: IOP Publishing.
- [21] Minakov, A. V., Sentyabov, A. V., Platonov, D. V., Dekterev, A. A., and Gavrilov, A. A., 2015, “Numerical modeling of flow in the Francis-99 turbine with Reynolds stress model and detached eddy simulation method,” *Journal of Physics: Conference Series*, **579**, p. 012004, Publisher: IOP Publishing.
- [22] Trivedi, C., Cervantes, M. J., Gandhi, B. K., and Dahlhaug, O. G., 2013, “Experimental and Numerical Studies for a High Head Francis Turbine at Several Operating Points,” *Journal of Fluids Engineering*, **135**(11), pp. 111102–1 – 111102–17.
- [23] Minakov, A. V., Sentyabov, A. V., Platonov, D. V., Dekterev, A. A., and Gavrilov, A. A., 2015, “Numerical modeling of flow in the Francis-99 turbine with Reynolds stress model and detached eddy simulation method,” *Journal of Physics: Conference Series*, **579**, p. 012004, Publisher: IOP Publishing.
- [24] Minakov, A. V., Platonov, D. V., Dekterev, A. A., Sentyabov, A. V., and Zakharov, A. V., 2015, “The analysis of unsteady flow structure and low frequency pressure pulsations in the high-head Francis turbines,” *International Journal of Heat and Fluid Flow*, **53**, pp. 183–194.
- [25] Trivedi, C., Gandhi, B., and Michel, C. J., 2013, “Effect of transients on Francis turbine runner life: a review,” *Journal of Hydraulic Research*, **51**(2), pp. 121–132, Publisher: Taylor & Francis.
- [26] Wu, J.-Z., Ma, H.-Y., and Zhou, M.-D., 2006, *Vorticity and Vortex Dynamics*, Springer Berlin Heidelberg.
- [27] Nitsche, M., 2006, “Vortex Dynamics,” [10.1016/B0-12-512666-2/00254-6](https://doi.org/10.1016/B0-12-512666-2/00254-6)

- [28] Li, Q., Wu, H., Guo, M., and Wu, J.-Z., 2010, “Vorticity Dynamics in Axial Compressor Flow Diagnosis and Design—Part II: Methodology and Application of Boundary Vorticity Flux,” [Journal of Fluids Engineering-transactions of The Asme - J FLUID ENG](#), **132**, pp. 1–12.
- [29] Lastiwka, D., 2009, “Influence of Rotor Blade Scaling on the Numerical Simulation of a High Pressure Gas Turbine,” Ph.D. thesis, University of Ottawa.
- [30] Leibovich, S., 1978, “The Structure of Vortex Breakdown,” *Annual review of fluid mechanics*, **10**(1), pp. 221–246.
- [31] Susan-Resiga, R., Muntean, S., Hasmatuchi, V., Anton, I., and Avelan, F., 2010, “Analysis and Prevention of Vortex Breakdown in the Simplified Discharge Cone of a Francis Turbine,” [Journal of Fluids Engineering](#), **132**(5), pp. 1–15.
- [32] Lund, E., 1966, “Hydrauliske trykksvingninger i omdreiningshulrommet mellom ledeparat og løpehjul i en Francis turbin,” Ph.D. thesis, Norges Tekniske Høgskole.
- [33] Djupesland, A., 2020, “Numerical study of unsteady flow in slits and investigation of methods to reduce pressure pulsations in pipes,” Ph.D. thesis, Norwegian University of Science and Technology.
- [34] ANSYS, 2011, *ANSYS CFX Solver Theory Guide*, ANSYS.
- [35] Pope, S. B. and Pope, S. B., 2000, *Turbulent flows*, Cambridge university press.
- [36] Menter, F. R. and Egorov, Y., 2010, “The Scale-Adaptive Simulation Method for Unsteady Turbulent Flow Predictions. Part 1: Theory and Model Description,” [Flow, Turbulence and Combustion](#), **85**(1), pp. 113–138.
- [37] Egorov, Y., Menter, F. R., Lechner, R., and Cokljat, D., 2010, “The Scale-Adaptive Simulation Method for Unsteady Turbulent Flow Predictions. Part 2: Application to Complex Flows,” [Flow, Turbulence and Combustion](#), **85**(1), pp. 139–165.
- [38] Schmitt, F. G., 2007, “About Boussinesq’s turbulent viscosity hypothesis: historical remarks and a direct evaluation of its validity,” [Comptes Rendus Mécanique](#), **335**(9), pp. 617–627.

- [39] Menter, F. R., 1994, *Two-Equation Eddy-Viscosity Turbulence Models for Engineering Applications*, Vol. 32, AIAAJ.
- [40] Egorov, Y. and Menter, F., 2008, “Development and Application of SST-SAS Turbulence Model in the DESIDER Project,” [https://link.springer.com/chapter/10.1007/978-3-540-77815-8\\_27](https://link.springer.com/chapter/10.1007/978-3-540-77815-8_27)
- [41] Bredberg, J., 2000, “On the Wall Boundary Condition for Turbulence Models,” [http://www.tfd.chalmers.se/~lada/postscript\\_files/jonas\\_report\\_WF.pdf](http://www.tfd.chalmers.se/~lada/postscript_files/jonas_report_WF.pdf)
- [42] Jousef, M., 2018, “What is Yplus,” SimScale, accessed 06.11.2020, <https://www.simscale.com/forum/t/what-is-y-plus/82394>
- [43] ANSYS, 2013, *ANSYS CFD-Post User’s Guide*, ANSYS.
- [44] ANSYS, 2011, *ANSYS Fluid Dynamics Verification Manual*, ANSYS.
- [45] Celik, I. B., Ghia, U., Roache, P. J., Freitas, C. J., Coleman, H., and Raad, P. E., 2008, “Procedure for Estimation and Reporting of Uncertainty Due to Discretization in CFD Applications,” *Journal of Fluids Engineering*, **130**(7), pp. 1–4.
- [46] Eitzen, F. C., 2021, “Investigation of a Francis turbine during start-stop: A passage modelling approach,” .
- [47] ANSYS, 2013, *ANSYS CFX-Pre User’s Guide*, ANSYS.
- [48] Khozaei, M. H., Favrel, A., Masuko, T., Yamaguchi, N., and Miyagawa, K., 2021, “Generation of Twin Vortex Rope in the Draft-Tube Elbow of a Francis Turbine During Deep Part-Load Operation,” *Journal of Fluids Engineering*, **143**(10), pp. 1–14.
- [49] Vagnoni, E., Favrel, A., Andolfatto, L., and Avellan, F., 2018, “Experimental investigation of the sloshing motion of the water free surface in the draft tube of a Francis turbine operating in synchronous condenser mode,” *Experiments in Fluids*, **59**(6), p. 95.



---

## Appendices

### **Appendix A**

Interpolation calculation

Monitor Point	HI/BEP to BEP			BEP/PL to PL			Summary		
	Measures value	Velocity 1 [m/s]	Velocity 2 [m/s]	Pressure 1 [Pa]	Pressure 2 [Pa]	Velocity 1 [m/s]	Velocity 2 [m/s]	Pressure 1 [Pa]	Pressure 2 [Pa]
MP1	Measures value Delta Value Error	9.49231 0.00063 0.00007 %	9.49294 m/s	167990 3 Pa 0.00002 %	167987 Pa	9.08844 0.00509 0.00056 %	9.09353 m/s	167416 2 Pa 0.00001 %	167414 Pa
MP2	Measures value Delta Value Error	9.57251 0.00083 0.00009 %	9.57168 m/s	167065 0 Pa 0.00000 %	167065 Pa	9.61426 0.00633 0.00066 %	9.60793 m/s	167278 5 Pa 0.00003 %	167283 Pa
MP3	Measures value Delta Value Error	8.50863 0.00047 0.00005 %	8.50816 m/s	164983 0 Pa 0.00000 %	164983 Pa	10.22780 0.00980 0.00096 %	10.21800 m/s	165257 2 Pa 0.00001 %	165255 Pa
MP4	Measures value Delta Value Error	10.04840 0.00020 0.00002 %	10.04820 m/s	164119 0 Pa 0.00000 %	164119 Pa	9.85903 0.00161 0.00016 %	9.86064 m/s	164344 0 Pa 0.00000 %	164344 Pa
MP5	Measures value Delta Value Error	9.92558 0.00014 0.00001 %	9.92572 m/s	164488 0 Pa 0.00000 %	164488 Pa	9.37901 0.00853 0.00091 %	9.38754 m/s	164747 0 Pa 0.00000 %	164747 Pa
MP6	Measures value Delta Value Error	3.39259 0.00016 0.00005 %	3.39243 m/s	208976 1 Pa 0.00000 %	208977 Pa	2.26736 0.00038 0.00017 %	2.26698 m/s	214987 0 Pa 0.00000 %	214987 Pa
MP7	Measures value Delta Value Error	2.93039 0.23834 0.08133 %	2.69205 m/s	211210 86 Pa 0.00041 %	211124 Pa	1.72778 0.00048 0.00028 %	1.72730 m/s	215936 1 Pa 0.00000 %	215937 Pa
MP8	Measures value Delta Value Error	1.48323 0.00094 0.00063 %	1.48229 m/s	213150 2 Pa 0.00001 %	213148 Pa	1.28264 0.00020 0.00016 %	1.28244 m/s	216323 1 Pa 0.00000 %	216322 Pa
MP9	Measures value Delta Value Error	2.45309 0.00000 0.00000 %	2.45309 m/s	210318 1 Pa 0.00000 %	210319 Pa	1.41621 0.00028 0.00020 %	1.41649 m/s	215738 1 Pa 0.00000 %	215737 Pa
MP10	Measures value Delta Value Error	3.43722 0.00287 0.00083 %	3.43435 m/s	209427 1 Pa 0.00000 %	209428 Pa	2.16028 0.00113 0.00052 %	2.15915 m/s	215313 1 Pa 0.00000 %	215312 Pa

---

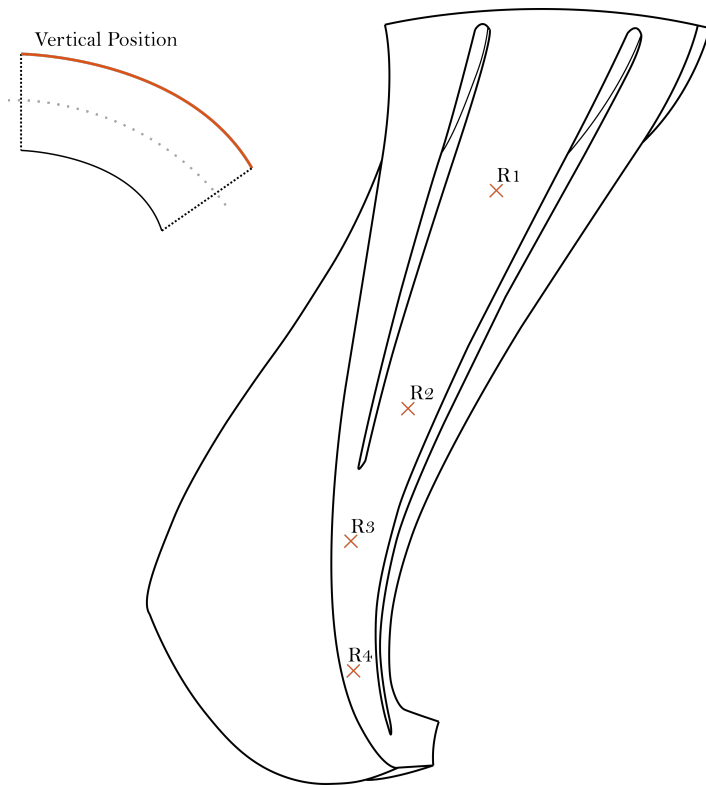
Appendices

---

## Appendix B – Overview of monitor point locations

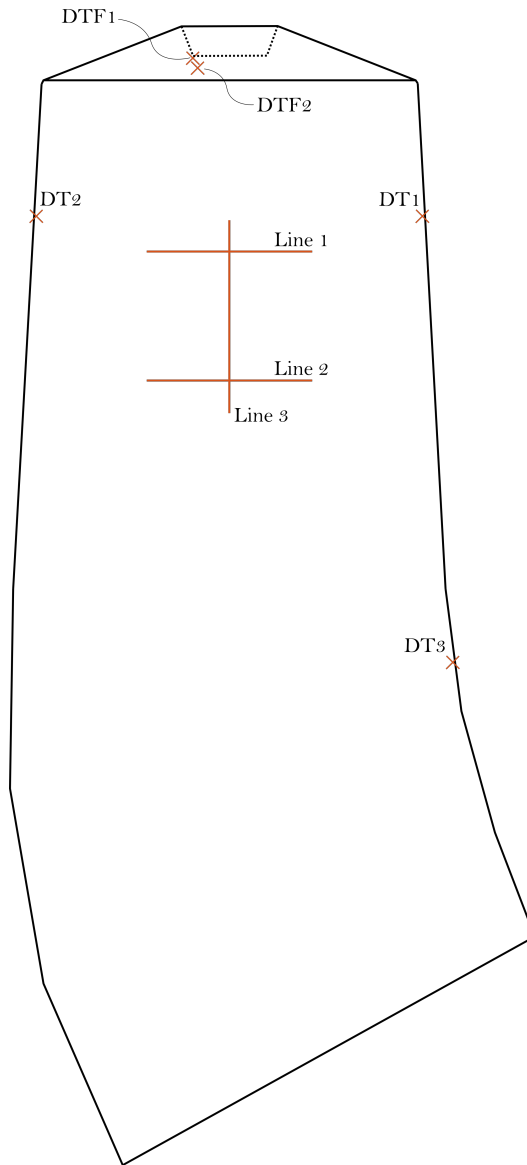
**Table B.1:** Monitor point and velocity line coordinates

Monitor Point	X	Y	Z
S1	-0.0431891	0.364558	-0.0298
S2	-0.0185776	0.350578	-0.0298
S3	0.00641376	0.336718	-0.0298
S4	0.0335927	0.326058	-0.0298
SF1	-0.0627649	0.322703	-0.0298
SF1TW	-0.0627649	0.322703	0
SF2	-0.0700102	0.323533	-0.0298
VL2	0.0622	0.32	-0.0294
R1	-0.0182	0.2397	0.02173
R2	-0.0554	0.1473	-0.0095
R3	-0.079445	0.092108	-0.03161
R4	-0.07851	0.03737	-0.05959
DT1	-0.1491	-0.1006	-0.3058
DT2	0.1491	0.1006	-0.3058
DT3	0.210062	0.000314951	-0.721355
DTF1	-0.0340065	0.00447705	-0.1576
DTF2	-0.0306206	0.00447705	-0.1665
Line	X	Y	Z
Line 1	0.02596	0.13355	-0.3386
	-0.02556	-0.13149	-0.3386
Line 2	0.02596	0.13355	-0.4586
	-0.02556	-0.13149	-0.4586
Line 3	0	0	-0.3086
	0	0	-0.4886



**Figure B.1:** Overview of monitor point position in rotor domain.

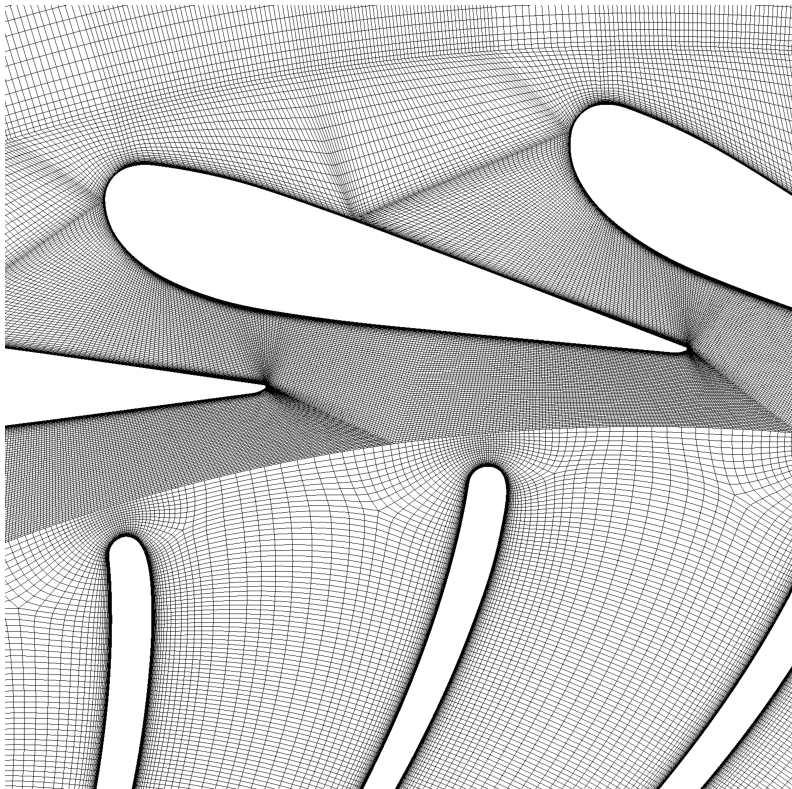




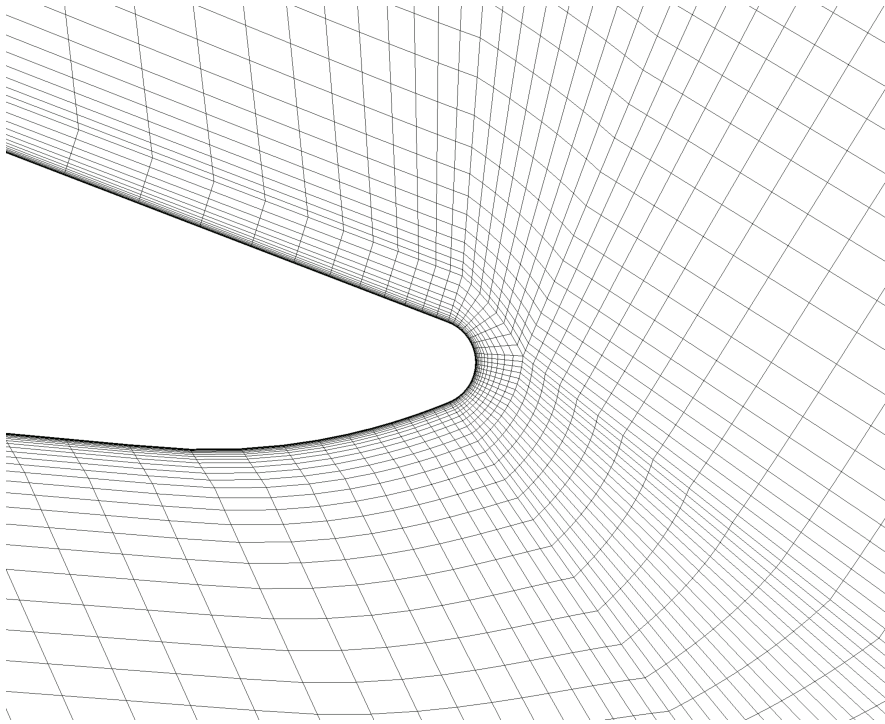
**Figure B.2:** Overview of monitor point position in draft tube domain.



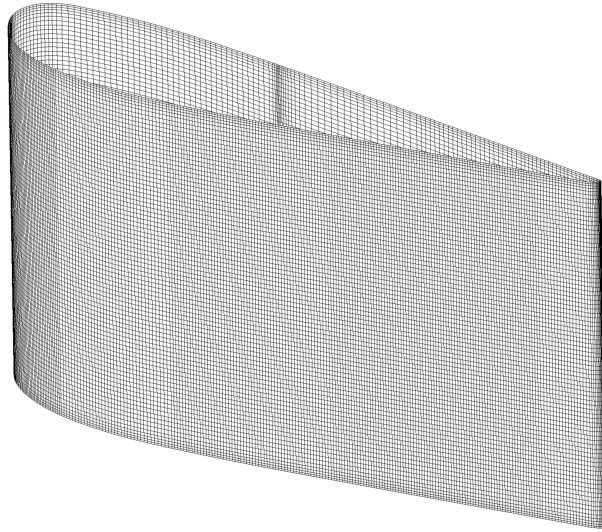
## Appendix C – Mesh and interface setup



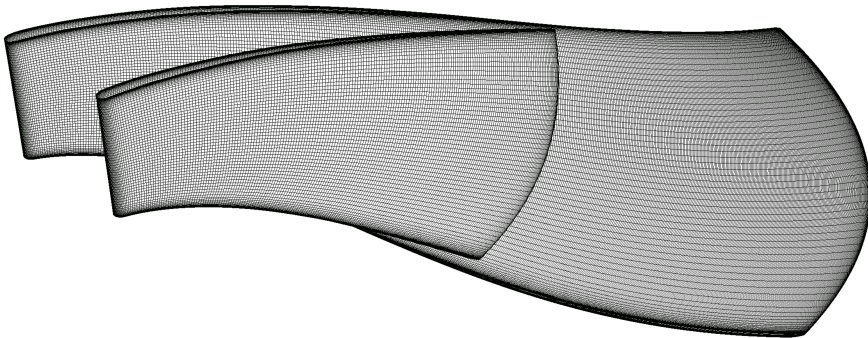
**Figure C.1:** Guide vane passage mesh and mesh interface.



**Figure C.2:** Guide vane trailing edge before remeshing at BEP.



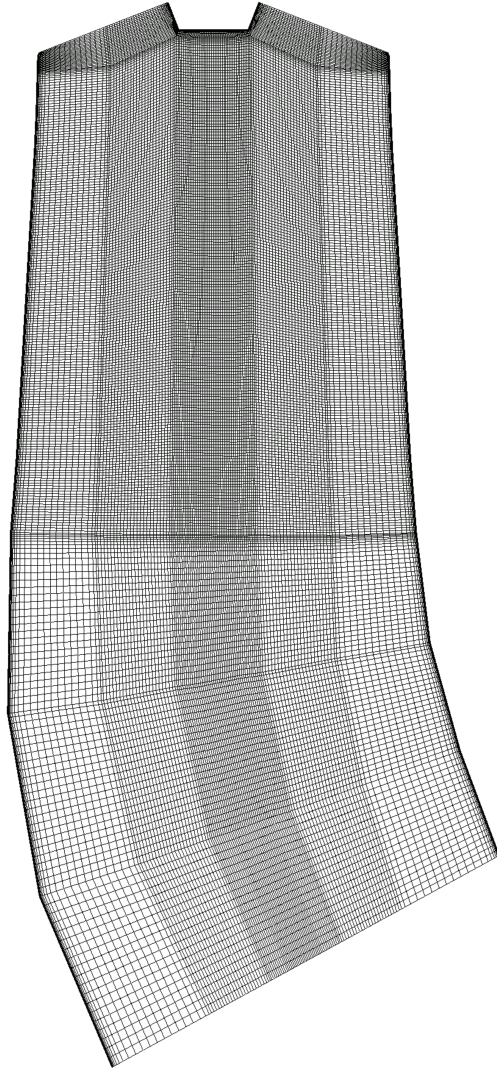
**Figure C.3:** Guide vane Mesh.



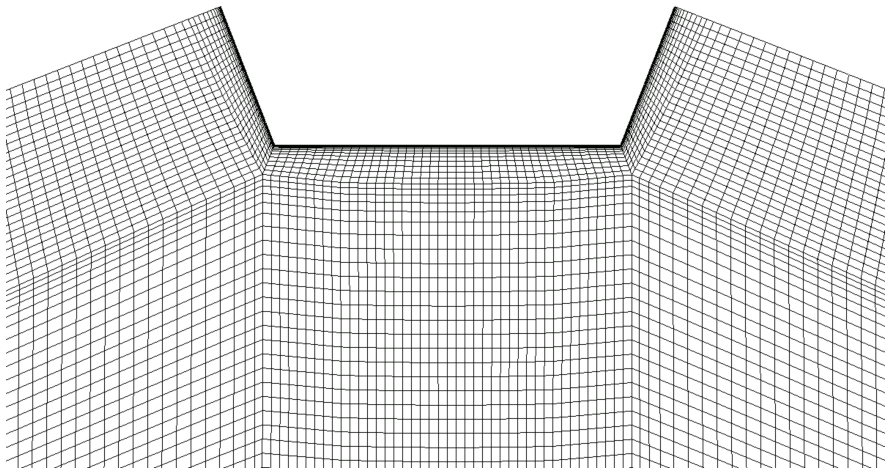
**Figure C.4:** Runner main blade and splitter blade mesh.



Figure C.5: Runner passage mesh.



**Figure C.6:** Draft tube mesh.



**Figure C.7:** Close up of runner cone mesh.



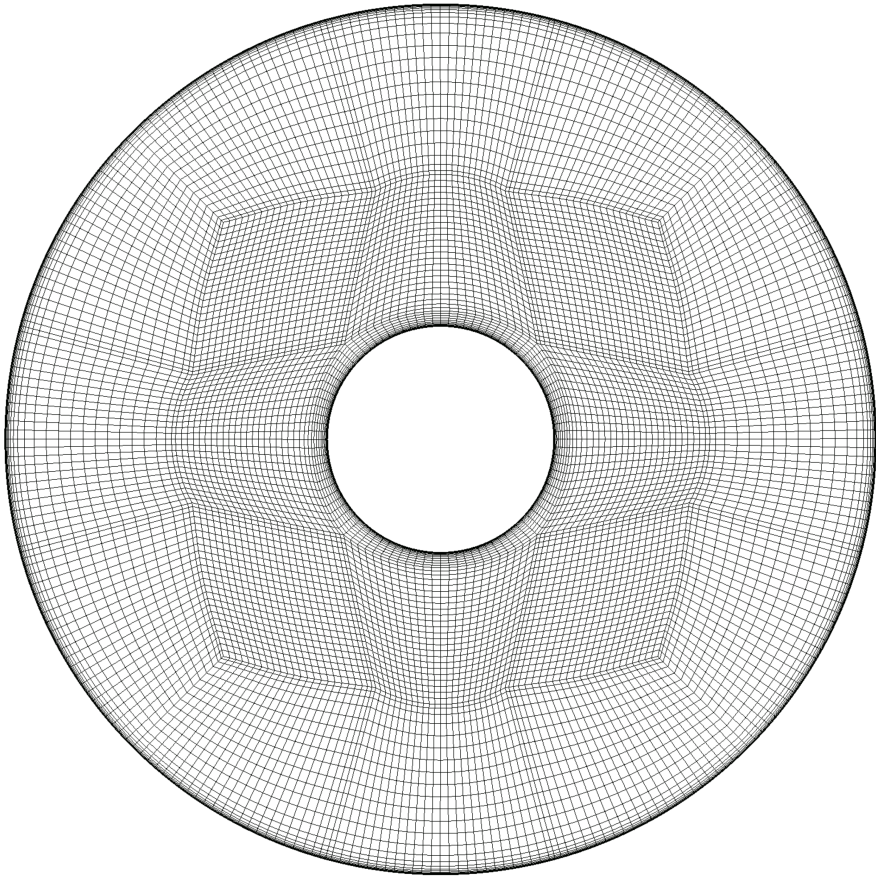


**Figure C.8:** Draft tube inlet mesh.

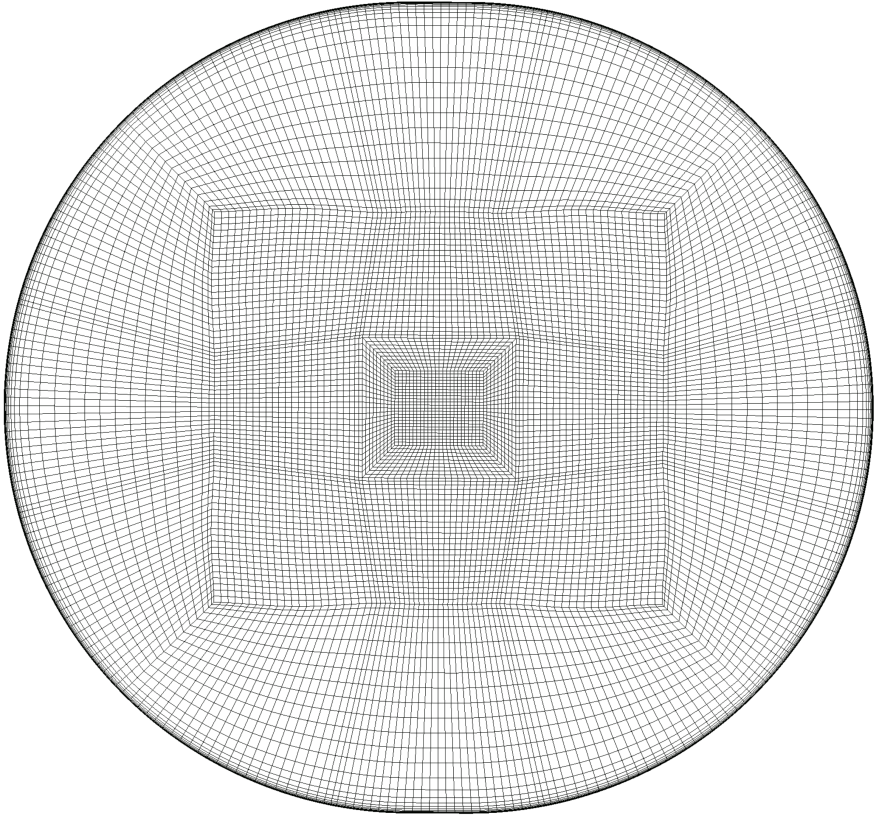


**Figure C.9:** Draft tube outlet mesh.

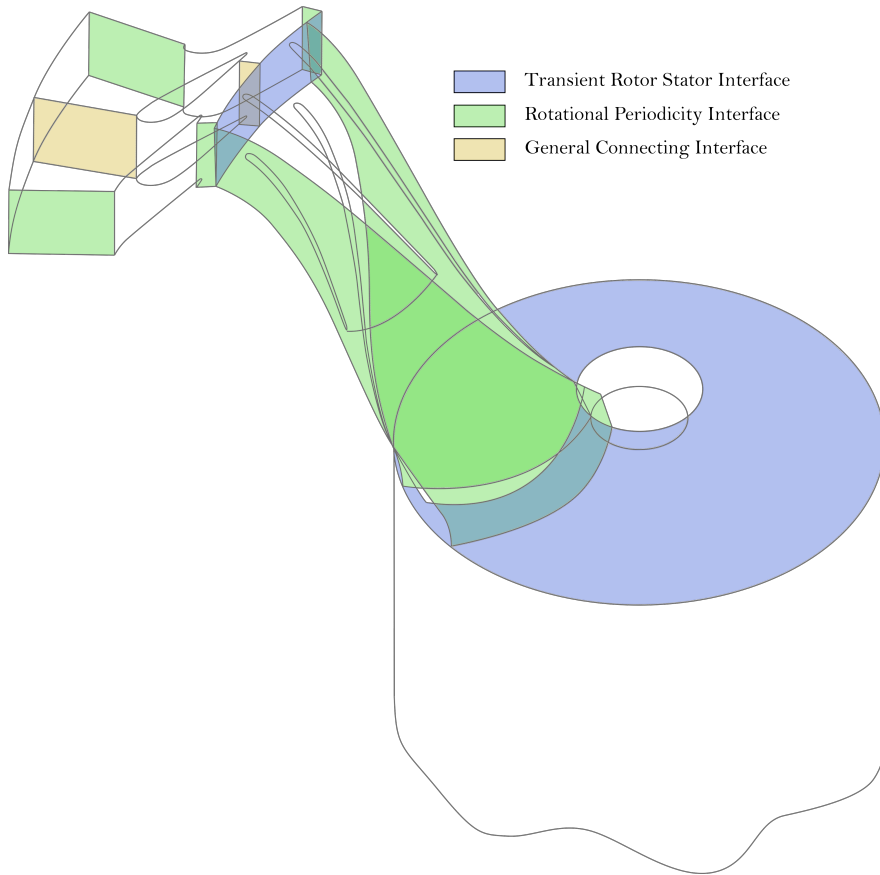


**Figure C.10:** Overview of interface models used in simulation setup



---

## Appendices

---

### Appendix D – Remesh script

#### D.1 - Geometry Modification Script

```
1 #Created by: Fabian Camillo Eitzen
2 #New script created: 04.04.2022.
3
4
5 # MODIFICATON LOG:
6 # - [date] "modification"
7
8
9 # Set Geometry Topo Tolerance
10 set ::geo_cad(toptol_userset) 1 ;# use user tolerance
11 set ::geo_cad(tolere) 0.0000000000000000001 ;# <--- your own topo tolerance
12 ic_set_meshing_params global 0 gttol 1E-20 gtrrel 1
13 ic_regenerate_tris
14
15
16 # Delete existing curves and surfaces
17
18 ic_delete_geometry surface names {FACE49 FACE58 FACE56 FACE51} 0
19 ic_geo_delete_family SYM_HIGH
20 ic_geo_delete_family SYM_LOW
21 ic_geo_set_dormant_entity curve {crv.04.0 crv.05.0 crv.06.0 crv.07.0 crv.10.0 crv.11.0 crv.08.0 crv.09.0} 1
22 ic_set_dormant_pickable curve 0 {}
23
24
25 # Retrive Monitor Angle
26
27 if [info exists ScalarParam(Angle)] {
28     set NewAngle $ScalarParam(Angle);
29 } else {
30     mess "The angle was not retrieved \n";
31 }
32
33 mess "Measured angle (NewAngle) = $NewAngle \n";
34
35
36 # Set correct angle for rotation
37
38 set GV_Angle ((180*$NewAngle)/(3.14159265359))
39 set GV_init_Angle 9.84
40 set GV_Angle_final $GV_init_Angle-$GV_Angle
41 mess "New GV Angle is set to: $GV_Angle \n";
42 mess "Angle Change is: $GV_Angle_final \n";
43
44
```

```

45 # Rotate Blades
46
47 mess "Rotation Started: \n";
48 ic_move_geometry surface names {FACE61 FACE46 FACE47 FACE48 FACE59 FACE60} rotate $GV_Angle_final
rotate_axis {0 0 1} cent pnt.02
49 ic_move_geometry curve names {EDGE43.3 EDGE43.2 EDGE44.3 EDGE44.2 EDGE67 EDGE65 EDGE69 EDGE35 EDGE38 EDGE41
EDGE68 EDGE4 EDGE37 EDGE40 EDGE64 EDGE42 EDGE39 EDGE6 EDGE70 EDGE66 EDGE5} rotate $GV_Angle_final
rotate_axis {0 0 1} cent pnt.02
50 ic_move_geometry point names {pnt.15.0 pnt.14.0 pnt.13.0 pnt.11.0 pnt.12.0 pnt.09.0 pnt.10.0 pnt.07.0
pnt.06.0 pnt.15 pnt.14 pnt.13 pnt.12 pnt.11 pnt.10 pnt.09 pnt.07 pnt.06 VERT101_2 VERT83_2 VERT87 VERT81
VERT82 VERT93 VERT86 VERT84 VERT100 VERT99 VERT89 VERT102 VERT85 VERT101 VERT88 VERT71} rotate
$GV_Angle_final rotate_axis {0 0 1} cent pnt.02
51 ic_geo_reset_data_structures
52 ic_geo_configure_one_attribute surface shade wire
53 ic_move_geometry surface names {FACE52 FACE53 FACE54 FACE55} rotate $GV_Angle_final rotate_axis {0 0 1} cent
pnt.03
54 ic_move_geometry curve names {EDGE17 EDGE20 EDGE23 EDGE26 EDGE16 EDGE19 EDGE22 EDGE25 EDGE14 EDGE27 EDGE24
EDGE21 EDGE18} rotate $GV_Angle_final rotate_axis {0 0 1} cent pnt.03
55 ic_move_geometry point names {pnt.25.0 pnt.24.0 pnt.23.0 pnt.22.0 pnt.21.0 pnt.20.0 pnt.19.0 pnt.18.0
pnt.17.0 pnt.16.0 pnt.26 pnt.25 pnt.24 pnt.23 pnt.22 pnt.21 pnt.20 pnt.19 pnt.18 pnt.17 pnt.16 VERT75 VERT76
VERT77 VERT78 VERT74 VERT96 VERT95 VERT94 VERT93 VERT92 pnt.26.0} rotate $GV_Angle_final rotate_axis {0 0 1}
cent pnt.03
56 ic_geo_reset_data_structures
57 ic_geo_configure_one_attribute surface shade wire
58 mess "Rotation Ended \n";
59
60
61 # Insert Surfaces
62
63 mess "Creation of Surface Started: \n";
64 ic_delete_geometry curve names crv.04 0
65 ic_curve_point GV_MASTER crv.04 {VERT72 VERT71}
66 ic_delete_geometry curve names crv.05 0
67 ic_curve_point GV_MASTER crv.05 {VERT90 VERT88}
68 ic_delete_geometry curve names crv.06 0
69 ic_curve_point GV_MASTER crv.06 {VERT81 VERT80}
70 ic_delete_geometry curve names crv.07 0
71 ic_curve_point GV_MASTER crv.07 {VERT99 VERT98}
72 ic_delete_geometry curve names crv.08 0
73 ic_curve_point GV_MASTER crv.08 {VERT78 VERT79}
74 ic_delete_geometry curve names crv.09 0
75 ic_curve_point GV_MASTER crv.09 {VERT96 VERT97}
76 ic_delete_geometry curve names crv.10 0
77 ic_curve_point GV_MASTER crv.10 {VERT73 VERT74}
78 ic_delete_geometry curve names crv.11 0
79 ic_curve_point GV_MASTER crv.11 {VERT91 VERT92}
80
81 ic_surface 2-4crvs GV_MASTER srf.01 {1E-20 {crv.04 EDGE5 crv.05 EDGE8}}
82 ic_set_dormant_pickable point 0 {}
83 ic_set_dormant_pickable curve 0 {}
84 ic_surface 2-4crvs GV_MASTER srf.02 {1E-20 {EDGE35 crv.06 EDGE32 crv.07}}
85 ic_set_dormant_pickable point 0 {}
86 ic_set_dormant_pickable curve 0 {}
87 ic_surface 2-4crvs GV_MASTER srf.03 {1E-20 {crv.10 EDGE11 crv.11 EDGE14}}
88 ic_set_dormant_pickable point 0 {}
89 ic_set_dormant_pickable curve 0 {}
90 ic_surface 2-4crvs GV_MASTER srf.04 {1E-20 {EDGE26 crv.08 EDGE29 crv.09}}
91 ic_set_dormant_pickable point 0 {}
92 ic_set_dormant_pickable curve 0 {}
93
94 ic_geo_set_part surface {srf.01 srf.02} SYM_LOW 0
95 ic_delete_empty_parts
96 ic_geo_set_part surface {srf.03 srf.04} SYM_HIGH 0
97 ic_delete_empty_parts
98
99 # Insert Mesh Points:
100 ic_point crv_par GV_MASTER pnt.45 {crv.04 0.745566811026374}
101 ic_point crv_par GV_MASTER pnt.45.0 {crv.05 0.745566811026374}
102 ic_point crv_par GV_MASTER pnt.46 {crv.10 0.745811903594142}
103 ic_point crv_par GV_MASTER pnt.46.0 {crv.11 0.745811903594142}
104
105 mess "Creation of Surface Ended \n";

```

## D.2 - Mesh Replay Script

```
1 #ICEM CFD Mesh Replay Script
2 #Created by: Fabian Camillo Eitzen
3 #New script created: 04.04.2022.
4
5
6 # MODIFICATON LOG:
7 # - [date] "modification"
8
9
10 # Set Work Directory:
11 set DIR env(PATH)
12
13
14 # Set Geometry Topo Tolerance
15 set ::geo_cad(toptol_userset) 1 ;# use user tolerance
16 set ::geo_cad(tolier) 0.00000000000000000001 ;# <--- your own topo tolerance
17 ic_set_meshing_params global 0 gttol 1E-20 gtrrel 1
18 ic_regenerate_tris
19
20 # Meshing:
21 mess "Mesh Initiated \n";
22 ic_geo_new_family FLUID
23 ic_boco_set_part_color FLUID
24 ic_hex_initialize_blocking {} FLUID 0 101
25 ic_hex_unblank blocks
26 ic_hex_multi_grid_level 0
27 ic_hex_projection_limit 0
28 ic_hex_default_bunching_law default 2
29 ic_hex_floating_grid off
30 ic_hex_transfinite_degree 1
31 ic_hex_unstruct_face_type several_tris
32 ic_hex_set_unstruct_face_method uniform_quad
33 ic_hex_set_n_tetra_smoothing_steps 20
34 ic_hex_error_messages off_minor
35 ic_hex_set_piercing 0
36 ic_hex_split_grid 21 25 0.881003 m GV_MASTER SYSTEMPOINTS INLET S_R BLADE_LOW BLADE_HIGH S_HUB S_SHROUD
SYM_LOW SYM_HIGH FLUID
37 ic_hex_split_grid 21 69 0.863861 m GV_MASTER SYSTEMPOINTS INLET S_R BLADE_LOW BLADE_HIGH S_HUB S_SHROUD
SYM_LOW SYM_HIGH FLUID
38 ic_hex_split_grid 21 85 0.287305 m GV_MASTER SYSTEMPOINTS INLET S_R BLADE_LOW BLADE_HIGH S_HUB S_SHROUD
SYM_LOW SYM_HIGH FLUID
39 ic_hex_split_grid 21 101 0.484225 m GV_MASTER SYSTEMPOINTS INLET S_R BLADE_LOW BLADE_HIGH S_HUB S_SHROUD
SYM_LOW SYM_HIGH FLUID
40 ic_hex_split_grid 25 41 0.724897 m GV_MASTER SYSTEMPOINTS INLET S_R BLADE_LOW BLADE_HIGH S_HUB S_SHROUD
SYM_LOW SYM_HIGH FLUID
41 ic_hex_split_grid 25 142 0.29267 m GV_MASTER SYSTEMPOINTS INLET S_R BLADE_LOW BLADE_HIGH S_HUB S_SHROUD
SYM_LOW SYM_HIGH FLUID
42 ic_hex_mark_blocks unmark
43 ic_hex_mark_blocks unmark
44 ic_hex_mark_blocks unmark
45 ic_hex_mark_blocks superblock 29
46 ic_hex_mark_blocks superblock 33
47 ic_hex_mark_blocks superblock 32
48 ic_hex_mark_blocks superblock 31
49 ic_hex_mark_blocks face_neighbors corners { 85 172 101 171 } { 85 101 89 105 } { 89 180 105 179 } { 86 140
102 139 } { 86 102 90 106 } { 90 148 106 147 } { 102 139 118 138 } { 37 137 118 138 } { 37 38 137 145 } { 38
145 122 146 } { 37 118 38 122 } { 106 147 122 146 } { 102 118 106 122 }
50 ic_hex_ogrid 0.5 m GV_MASTER SYSTEMPOINTS INLET S_R BLADE_LOW BLADE_HIGH S_HUB S_SHROUD SYM_LOW SYM_HIGH
FLUID -version 50
```

```

51 ic_hex_mark_blocks unmark
52 ic_hex_mark_blocks unmark
53 ic_hex_mark_blocks unmark
54 ic_hex_mark_blocks superblock 29
55 ic_hex_mark_blocks superblock 13
56 ic_hex_mark_blocks superblock 31
57 ic_hex_mark_blocks superblock 32
58 ic_hex_mark_blocks superblock 33
59 ic_hex_change_element_id VORFN
60 ic_hex_move_node 206 VERT71
61 ic_hex_move_node 205 VERT88
62 ic_hex_move_node 73 pnt.45
63 ic_hex_move_node 69 pnt.45.0
64 ic_hex_move_node 26 VERT72
65 ic_hex_move_node 25 VERT90
66 ic_hex_move_node 182 pnt.50
67 ic_hex_move_node 174 pnt.50.0
68 ic_hex_move_node 181 pnt.43
69 ic_hex_move_node 173 pnt.43.0
70 ic_hex_move_node 142 pnt.49.0
71 ic_hex_move_node 150 pnt.49
72 ic_hex_move_node 41 VERT91
73 ic_hex_move_node 42 VERT73
74 ic_hex_move_node 214 pnt.06
75 ic_hex_move_node 213 pnt.06.0
76 ic_hex_move_node 180 pnt.07
77 ic_hex_move_node 172 pnt.07.0
78 ic_hex_move_node 149 pnt.44
79 ic_hex_move_node 141 pnt.44.0
80 ic_hex_move_node 74 pnt.46
81 ic_hex_move_node 70 pnt.46.0
82 ic_hex_move_node 148 pnt.16
83 ic_hex_move_node 140 pnt.16.0
84 ic_hex_move_node 234 VERT75
85 ic_hex_move_node 233 VERT93
86 ic_hex_move_node 238 VERT74
87 ic_hex_move_node 237 VERT92
88 ic_hex_move_node 230 pnt.23
89 ic_hex_move_node 147 pnt.24
90 ic_hex_move_node 229 pnt.23.0
91 ic_hex_move_node 139 pnt.24.0
92 ic_hex_move_node 226 pnt.25
93 ic_hex_move_node 146 pnt.26
94 ic_hex_move_node 225 pnt.25.0
95 ic_hex_move_node 138 pnt.26.0
96 ic_hex_move_node 222 VERT78
97 ic_hex_move_node 221 VERT96
98 ic_hex_move_node 177 VERT79
99 ic_hex_move_node 169 VERT97
100 ic_hex_place_node 89 surface:srf.00 0.915875615 0.491496904
101 ic_hex_place_node 85 surface:srf.00.0 0.915875615 0.491496904
102 ic_hex_place_node 90 surface:srf.00 0.456835593 0.391907916
103 ic_hex_place_node 86 surface:srf.00.0 0.456835593 0.391907916
104 ic_hex_place_node 145 surface:srf.00 0.0221405165 0.860383238
105 ic_hex_place_node 137 surface:srf.00.0 0.0221405165 0.860383238
106 ic_point {} GV_MASTER pnt.51 0.02736239,0.3145120,0.029803
107 ic_point {} GV_MASTER pnt.52 0.01740772,0.3152197,0.029803
108 ic_geo_duplicate_set_fam_and_data point pnt.52 pnt.52.0 {} _0
109 ic_move_geometry point names (pnt.52.0 pnt.51.0) translate {0 0 -0.059606}
110 ic_geo_reset_data_structures
111 ic_geo_configure_one attribute surface shade wire
112 ic_hex_move_node 178 pnt.51
113 ic_hex_move_node 170 pnt.51.0
114 ic_hex_move_node 121 VERT80
115 ic_hex_move_node 117 VERT98
116 ic_hex_move_node 179 pnt.14
117 ic_hex_move_node 171 pnt.14.0
118 ic_hex_move_node 210 VERT83_2
119 ic_hex_move_node 209 VERT101_2
120 ic_hex_move_node 202 VERT81
121 ic_hex_move_node 201 VERT99
122 ic_hex_place_node 105 surface:srf.00 0.429707183 0.790324545
123 ic_hex_place_node 101 surface:srf.00.0 0.429707183 0.790324545
124 ic_hex_mark_blocks unmark
125 ic_hex_mark_blocks unmark
126 ic_hex_mark_blocks unmark

```

Figure D.1: Mesh Replay Script - Continuation



```

127 ic_hex_mark blocks unmark
128 ic_hex_mark blocks superblock 30
129 ic_hex_mark blocks superblock 84
130 ic_hex_split_grid 121 178 0.596952 m GV_MASTER SYSTEMPOINTS INLET S_R BLADE_LOW BLADE_HIGH S_HUB S_SHROUD
SYM_LOW SYM_HIGH FLUID marked
131 ic_hex_move_node 266 pnt.52
132 ic_hex_move_node 256 pnt.52.0
133 ic_hex_move_node 267 pnt.15
134 ic_hex_move_node 268 VERT83
135 ic_hex_move_node 257 pnt.15.0
136 ic_hex_move_node 258 VERT101
137 ic_hex_split_grid 210 214 0.602015 m GV_MASTER SYSTEMPOINTS INLET S_R BLADE_LOW BLADE_HIGH S_HUB S_SHROUD
SYM_LOW SYM_HIGH FLUID
138 ic_hex_split_grid 210 306 0.4952 m GV_MASTER SYSTEMPOINTS INLET S_R BLADE_LOW BLADE_HIGH S_HUB S_SHROUD
SYM_LOW SYM_HIGH FLUID
139 ic_hex_split_grid 210 342 0.299317 m GV_MASTER SYSTEMPOINTS INLET S_R BLADE_LOW BLADE_HIGH S_HUB S_SHROUD
SYM_LOW SYM_HIGH FLUID
140 ic_hex_move_node 305 pnt.10
141 ic_hex_move_node 306 pnt.09
142 ic_hex_move_node 296 pnt.10.0
143 ic_hex_move_node 297 pnt.09.0
144 ic_hex_move_node 307 pnt.18
145 ic_hex_move_node 308 pnt.17
146 ic_hex_move_node 298 pnt.18.0
147 ic_hex_move_node 299 pnt.17.0
148 ic_hex_move_node 343 pnt.20
149 ic_hex_move_node 344 pnt.19
150 ic_hex_move_node 334 pnt.20.0
151 ic_hex_move_node 335 pnt.19.0
152 ic_hex_move_node 341 pnt.12
153 ic_hex_move_node 342 pnt.11
154 ic_hex_move_node 332 pnt.12.0
155 ic_hex_move_node 333 pnt.11.0
156 ic_hex_move_node 377 pnt.13
157 ic_hex_move_node 378 VERT84
158 ic_hex_move_node 368 pnt.13.0
159 ic_hex_move_node 369 VERT85
160 ic_hex_move_node 379 pnt.22
161 ic_hex_move_node 380 pnt.21
162 ic_hex_move_node 370 pnt.22.0
163 ic_hex_move_node 371 pnt.21.0
164 ic_hex_find_comp_curve EDGE10
165 ic_hex_set_edge_projection 26 272 0 1 EDGE10
166 ic_hex_set_edge_projection 182 150 0 1 EDGE10
167 ic_hex_set_edge_projection 150 42 0 1 EDGE10
168 ic_hex_find_comp_curve EDGE12
169 ic_hex_set_edge_projection 25 262 0 1 EDGE12
170 ic_hex_set_edge_projection 174 142 0 1 EDGE12
171 ic_hex_set_edge_projection 142 41 0 1 EDGE12
172 ic_hex_find_comp_curve EDGE8
173 ic_hex_set_edge_projection 25 26 0 1 EDGE8
174 ic_hex_find_comp_curve EDGE11
175 ic_hex_set_edge_projection 41 42 0 1 EDGE11
176 ic_hex_find_comp_curve crv.04
177 ic_hex_set_edge_projection 73 26 0 1 crv.04
178 ic_hex_set_edge_projection 89 73 0 1 crv.04
179 ic_hex_set_edge_projection 89 206 0 1 crv.04
180 ic_hex_find_comp_curve crv.05
181 ic_hex_set_edge_projection 69 25 0 1 crv.05
182 ic_hex_set_edge_projection 85 69 0 1 crv.05
183 ic_hex_set_edge_projection 85 205 0 1 crv.05
184 ic_hex_find_comp_curve crv.11
185 ic_hex_set_edge_projection 70 41 0 1 crv.11
186 ic_hex_set_edge_projection 86 70 0 1 crv.11
187 ic_hex_set_edge_projection 86 237 0 1 crv.11
188 ic_hex_find_comp_curve crv.10
189 ic_hex_set_edge_projection 74 42 0 1 crv.10
190 ic_hex_set_edge_projection 90 74 0 1 crv.10
191 ic_hex_set_edge_projection 90 238 0 1 crv.10
192 ic_hex_find_comp_curve EDGE5
193 ic_hex_set_edge_projection 205 206 0 1 EDGE5
194 ic_hex_find_comp_curve EDGE14
195 ic_hex_set_edge_projection 237 238 0 1 EDGE14
196 ic_hex_find_comp_curve EDGE37
197 ic_hex_find_comp_curve EDGE40
198 ic_hex_find_comp_curve EDGE43.2

```

Figure D.2: Mesh Replay Script - Continuation

```

199 ic_hex_find_comp_curve EDGE43.3
200 ic_hex_find_comp_curve EDGE64
201 ic_hex_find_comp_curve EDGE68
202 ic_hex_find_comp_curve EDGE4
203 ic_hex_create_composite {EDGE37 EDGE40 EDGE43.2 EDGE43.3 EDGE64 EDGE68 EDGE4}
204 ic_hex_set_edge_projection 206 270 0 1 EDGE37
205 ic_hex_set_edge_projection 306 214 0 1 EDGE37
206 ic_hex_set_edge_projection 342 306 0 1 EDGE37
207 ic_hex_set_edge_projection 210 378 0 1 EDGE37
208 ic_hex_set_edge_projection 268 210 0 1 EDGE37
209 ic_hex_set_edge_projection 202 268 0 1 EDGE37
210 ic_hex_set_edge_projection 378 342 0 1 EDGE37
211 ic_hex_find_comp_curve EDGE39
212 ic_hex_find_comp_curve EDGE42
213 ic_hex_find_comp_curve EDGE44.2
214 ic_hex_find_comp_curve EDGE44.3
215 ic_hex_find_comp_curve EDGE66
216 ic_hex_find_comp_curve EDGE70
217 ic_hex_find_comp_curve EDGE6
218 ic_hex_create_composite {EDGE39 EDGE42 EDGE44.2 EDGE44.3 EDGE66 EDGE70 EDGE6}
219 ic_hex_set_edge_projection 205 260 0 1 EDGE39
220 ic_hex_set_edge_projection 297 213 0 1 EDGE39
221 ic_hex_set_edge_projection 333 297 0 1 EDGE39
222 ic_hex_set_edge_projection 369 333 0 1 EDGE39
223 ic_hex_set_edge_projection 209 369 0 1 EDGE39
224 ic_hex_set_edge_projection 258 209 0 1 EDGE39
225 ic_hex_set_edge_projection 201 258 0 1 EDGE39
226 ic_hex_find_comp_curve EDGE16
227 ic_hex_find_comp_curve EDGE19
228 ic_hex_find_comp_curve EDGE22
229 ic_hex_find_comp_curve EDGE25
230 ic_hex_create_composite {EDGE16 EDGE19 EDGE22 EDGE25}
231 ic_hex_set_edge_projection 222 226 0 1 EDGE16
232 ic_hex_set_edge_projection 226 230 0 1 EDGE16
233 ic_hex_set_edge_projection 230 380 0 1 EDGE16
234 ic_hex_set_edge_projection 380 344 0 1 EDGE16
235 ic_hex_set_edge_projection 344 308 0 1 EDGE16
236 ic_hex_set_edge_projection 308 234 0 1 EDGE16
237 ic_hex_set_edge_projection 234 238 0 1 EDGE16
238 ic_hex_find_comp_curve EDGE27
239 ic_hex_find_comp_curve EDGE24
240 ic_hex_find_comp_curve EDGE21
241 ic_hex_find_comp_curve EDGE18
242 ic_hex_create_composite {EDGE27 EDGE24 EDGE21 EDGE18}
243 ic_hex_set_edge_projection 233 237 0 1 EDGE27
244 ic_hex_set_edge_projection 299 233 0 1 EDGE27
245 ic_hex_set_edge_projection 335 299 0 1 EDGE27
246 ic_hex_set_edge_projection 371 335 0 1 EDGE27
247 ic_hex_set_edge_projection 229 371 0 1 EDGE27
248 ic_hex_set_edge_projection 225 229 0 1 EDGE27
249 ic_hex_set_edge_projection 221 225 0 1 EDGE27
250 ic_hex_find_comp_curve crv.06
251 ic_hex_set_edge_projection 121 105 0 1 crv.06
252 ic_hex_set_edge_projection 105 202 0 1 crv.06
253 ic_hex_find_comp_curve srf.02e71
254 ic_hex_find_comp_curve crv.07
255 ic_hex_find_comp_curve EDGE36
256 ic_hex_set_edge_projection 117 101 0 1 crv.07
257 ic_hex_set_edge_projection 101 201 0 1 crv.07
258 ic_hex_find_comp_curve EDGE35
259 ic_hex_set_edge_projection 201 202 0 1 EDGE35
260 ic_hex_find_comp_curve EDGE32
261 ic_hex_set_edge_projection 117 121 0 1 EDGE32
262 ic_hex_find_comp_curve EDGE31
263 ic_hex_set_edge_projection 121 266 0 1 EDGE31
264 ic_hex_set_edge_projection 266 178 0 1 EDGE31
265 ic_hex_set_edge_projection 177 178 0 1 EDGE31
266 ic_hex_find_comp_curve EDGE33
267 ic_hex_set_edge_projection 117 256 0 1 EDGE33
268 ic_hex_set_edge_projection 256 170 0 1 EDGE33
269 ic_hex_set_edge_projection 169 170 0 1 EDGE33
270 ic_hex_find_comp_curve crv.08
271 ic_hex_set_edge_projection 177 145 0 1 crv.08
272 ic_hex_set_edge_projection 145 222 0 1 crv.08
273 ic_hex_find_comp_curve crv.09
274 ic_hex_set_edge_projection 169 137 0 1 crv.09

```

Figure D.3: Mesh Replay Script - Continuation

```

275 ic_hex_set_edge_projection 137 221 0 1 crv.09
276 ic_hex_find_comp_curve EDGE29
277 ic_hex_set_edge_projection 169 177 0 1 EDGE29
278 ic_hex_find_comp_curve EDGE26
279 ic_hex_set_edge_projection 221 222 0 1 EDGE26
280 ic_coords_dir_into_global { 0 0 1 } global
281 ic_geo_set_periodic data { axis { 0 0 1 } type rot angle 12.85714286 base { 0 0 0 } }
282 ic_hex_make_nodes_periodic { 26 } { 42 }
283 ic_hex_make_nodes_periodic { 25 } { 41 }
284 ic_hex_make_nodes_periodic { 73 } { 74 }
285 ic_hex_make_nodes_periodic { 69 } { 70 }
286 ic_hex_make_nodes_periodic { 89 } { 90 }
287 ic_hex_make_nodes_periodic { 206 } { 238 }
288 ic_hex_make_nodes_periodic { 85 } { 86 }
289 ic_hex_make_nodes_periodic { 205 } { 237 }
290 ic_hex_make_nodes_periodic { 202 } { 222 }
291 ic_hex_make_nodes_periodic { 105 } { 145 }
292 ic_hex_make_nodes_periodic { 121 } { 177 }
293 ic_hex_make_nodes_periodic { 201 } { 221 }
294 ic_hex_make_nodes_periodic { 101 } { 137 }
295 ic_hex_make_nodes_periodic { 117 } { 169 }
296 ic_hex_set_edge_length 89 206 0.0003
297 ic_hex_set_edge_length 85 205 0.0003
298 ic_hex_set_edge_length 105 202 0.000379
299 ic_hex_set_edge_length 101 201 0.000379
300 ic_hex_set_mesh 85 69 n 22 h1rel 1.01533872207e+012 h2rel 1.01533872207e+012 r1 2 r2 2 lmax 1e+10 default
copy_to_parallel unlocked
301 ic_hex_set_mesh 26 272 n 45 h1rel 278932247357.0 h2rel 278932247357.0 r1 2 r2 2 lmax 1e+10 default
copy_to_parallel unlocked
302 ic_hex_set_mesh 150 42 n 20 h1rel 515017922624.0 h2rel 515017922624.0 r1 2 r2 2 lmax 1e+10 default
copy_to_parallel unlocked
303 ic_hex_set_mesh 132 150 n 49 h1rel 268730517038.0 h2rel 268730517038.0 r1 2 r2 2 lmax 1e+10 default
copy_to_parallel unlocked
304 ic_hex_set_mesh 306 214 n 28 h1rel 0.0 h2rel 0.0 r1 2 r2 2 lmax 0 default copy_to_parallel unlocked
305 ic_hex_set_mesh 333 297 n 24 h1rel 0.0 h2rel 0.0 r1 2 r2 2 lmax 0 default copy_to_parallel unlocked
306 ic_hex_set_mesh 378 342 n 28 h1rel 0.0 h2rel 0.0 r1 2 r2 2 lmax 0 default copy_to_parallel unlocked
307 ic_hex_set_mesh 230 380 n 10 h1rel 0.0 h2rel 0.0 r1 2 r2 2 lmax 0 default copy_to_parallel unlocked
308 ic_hex_set_mesh 121 105 n 49 h1rel 695899066799.0 h2rel 695899066799.0 r1 2 r2 2 lmax 1e+10 default
copy_to_parallel unlocked
309 ic_hex_set_mesh 177 178 n 80 h1rel 0.0 h2rel 0.0 r1 2 r2 2 lmax 0 default copy_to_parallel unlocked
310 #ic_hex_set_mesh 89 206 n 17 h1rel 0.0 h2rel 0.00329533678756 r1 2 r2 1.2 lmax 0 default copy_to_parallel
unlocked
311 ic_hex_set_mesh 368 369 n 15 h1rel 0.0 h2rel 0.00563372900453 r1 2 r2 1.2 lmax 0 default copy_to_parallel
unlocked
312 ic_hex_set_mesh 117 256 n 28 h1rel 0.0 h2rel 0.0 r1 2 r2 2 lmax 0 default copy_to_parallel unlocked
313 ic_hex_set_mesh 256 170 n 18 h1rel 0.0 h2rel 0.0 r1 2 r2 2 lmax 0 default copy_to_parallel unlocked
314 ic_hex_set_mesh 25 26 n 84 h1rel 0.00503305036406 h2rel 0.00503305036406 r1 1.2 r2 1.2 lmax 1e+10 default
copy_to_parallel unlocked
315 ic_hex_set_mesh 73 26 n 30 h1rel 333464496035.0 h2rel 333464496035.0 r1 2 r2 2 lmax 1e+10 default
copy_to_parallel unlocked
316 ic_hex_set_mesh 73 26 n 30 h1rel 333464496035.0 h2rel 333464496035.0 r1 2 r2 2 lmax 1e+10 default
copy_to_parallel unlocked
317
318 mess " -- Mesh Refinement Initiated \n";
319 ic_hex_set_mesh 85 69 n 22 h1rel 0.0150982442755 h2rel 1.01533679654e+012 r1 1.5 r2 2 lmax 1e+10 default
unlocked
320 ic_hex_set_mesh 89 73 n 22 h1rel 0.0150982442755 h2rel 1.01533679654e+012 r1 1.5 r2 2 lmax 1e+10 default
unlocked
321 ic_hex_set_mesh 172 173 n 22 h1rel 0.00551809382967 h2rel 1.01534030085e+012 r1 1.5 r2 2 lmax 2.73614e+10
default unlocked
322 ic_hex_set_mesh 180 181 n 22 h1rel 0.00551809382967 h2rel 1.01534030085e+012 r1 1.5 r2 2 lmax 2.73614e+10
default unlocked
323 ic_hex_set_mesh 140 141 n 22 h1rel 0.00779455628189 h2rel 1.01533449039e+012 r1 1.5 r2 2 lmax 1.93702e+10
default unlocked
324 ic_hex_set_mesh 148 149 n 22 h1rel 0.00779455628189 h2rel 1.01533449039e+012 r1 1.5 r2 2 lmax 1.93702e+10
default unlocked
325 ic_hex_set_mesh 86 70 n 22 h1rel 0.0150982442755 h2rel 1.01533679654e+012 r1 1.5 r2 2 lmax 1e+10 default
unlocked
326 ic_hex_set_mesh 90 74 n 22 h1rel 0.0150982442755 h2rel 1.01533679654e+012 r1 1.5 r2 2 lmax 1e+10 default
unlocked
327 ic_hex_set_mesh 206 270 n 45 h1rel 278933430918.0 h2rel 0.00741771895252 r1 2 r2 1.5 lmax 1.12809e+10
default unlocked
328 ic_hex_set_mesh 85 259 n 45 h1rel 278933430918.0 h2rel 0.00741771895252 r1 2 r2 1.5 lmax 1.12809e+10 default
unlocked
329 ic_hex_set_mesh 205 260 n 45 h1rel 278933430918.0 h2rel 0.00741771895252 r1 2 r2 1.5 lmax 1.12809e+10
default unlocked

```

Figure D.4: Mesh Replay Script - Continuation

```

330 ic_hex_set_mesh 89 269 n 45 h1rel 278933430918.0 h2rel 0.00741771895252 r1 2 r2 1.5 lmax 1.12809e+10 default
unlocked
331 ic_hex_set_mesh 306 214 n 28 h1rel 0.0 h2rel 0.00749987812698 r1 2 r2 1.5 lmax 0 default unlocked
332 ic_hex_set_mesh 296 172 n 28 h1rel 0.0 h2rel 0.00749987812698 r1 2 r2 1.5 lmax 0 default unlocked
333 ic_hex_set_mesh 297 213 n 28 h1rel 0.0 h2rel 0.00749987812698 r1 2 r2 1.5 lmax 0 default unlocked
334 ic_hex_set_mesh 305 180 n 28 h1rel 0.0 h2rel 0.00749987812698 r1 2 r2 1.5 lmax 0 default unlocked
335 ic_hex_set_mesh 308 234 n 28 h1rel 0.0 h2rel 0.0148067716302 r1 2 r2 1.5 lmax 0 default unlocked
336 ic_hex_set_mesh 298 140 n 28 h1rel 0.0 h2rel 0.0148067716302 r1 2 r2 1.5 lmax 0 default unlocked
337 ic_hex_set_mesh 299 233 n 28 h1rel 0.0 h2rel 0.0148067716302 r1 2 r2 1.5 lmax 0 default unlocked
338 ic_hex_set_mesh 307 148 n 28 h1rel 0.0 h2rel 0.0148067716302 r1 2 r2 1.5 lmax 0 default unlocked
339 ic_hex_set_mesh 172 140 n 49 h1rel 0.00369946530395 h2rel 0.00369946530395 r1 1.5 r2 1.5 lmax 1.08961e+10
default unlocked
340 ic_hex_set_mesh 180 148 n 49 h1rel 0.00369946530395 h2rel 0.00369946530395 r1 1.5 r2 1.5 lmax 1.08961e+10
default unlocked
341 ic_hex_set_mesh 234 238 n 20 h1rel 0.0264607316128 h2rel 515018449745.0 r1 1.5 r2 2 lmax 3.8927e+09 default
unlocked
342 ic_hex_set_mesh 140 86 n 20 h1rel 0.0264607316128 h2rel 515018449745.0 r1 1.5 r2 2 lmax 3.8927e+09 default
unlocked
343 ic_hex_set_mesh 233 237 n 20 h1rel 0.0264607316128 h2rel 515018449745.0 r1 1.5 r2 2 lmax 3.8927e+09 default
unlocked
344 ic_hex_set_mesh 148 90 n 20 h1rel 0.0264607316128 h2rel 515018449745.0 r1 1.5 r2 2 lmax 3.8927e+09 default
unlocked
345 ic_hex_set_mesh 296 298 n 49 h1rel 0.00721039450472 h2rel 0.00721039450472 r1 1.5 r2 1.5 lmax 5.59049e+09
default unlocked
346 ic_hex_set_mesh 305 307 n 49 h1rel 0.00721039450472 h2rel 0.00721039450472 r1 1.5 r2 1.5 lmax 5.59049e+09
default unlocked
347 ic_hex_set_mesh 332 334 n 49 h1rel 0.00976111302718 h2rel 0.00976111302718 r1 1.5 r2 1.5 lmax 4.12961e+09
default unlocked
348 ic_hex_set_mesh 341 343 n 49 h1rel 0.00976111302718 h2rel 0.00976111302718 r1 1.5 r2 1.5 lmax 4.12961e+09
default unlocked
349 ic_hex_set_mesh 368 370 n 49 h1rel 0.00775903539672 h2rel 0.0116385530951 r1 1.5 r2 1.5 lmax 3.46346e+09
default unlocked
350 ic_hex_set_mesh 377 379 n 49 h1rel 0.00775903539672 h2rel 0.0116385530951 r1 1.5 r2 1.5 lmax 3.46346e+09
default unlocked
351 ic_hex_set_mesh 171 139 n 49 h1rel 0.00475030876904 h2rel 0.0118757323368 r1 1.5 r2 1.5 lmax 3.46346e+09
default unlocked
352 ic_hex_set_mesh 179 147 n 49 h1rel 0.00475030876904 h2rel 0.0118757323368 r1 1.5 r2 1.5 lmax 3.46346e+09
default unlocked
353 ic_hex_set_mesh 170 138 n 49 h1rel 268730321697.0 h2rel 0.0073335288941 r1 2 r2 1.5 lmax 5.49661e+09 default
unlocked
354 ic_hex_set_mesh 178 146 n 49 h1rel 268730321697.0 h2rel 0.0073335288941 r1 2 r2 1.5 lmax 5.49661e+09 default
unlocked
355 ic_hex_set_mesh 169 137 n 49 h1rel 268731384830.0 h2rel 0.0062630480167 r1 2 r2 1.5 lmax 3.86167e+09 default
unlocked
356 ic_hex_set_mesh 177 145 n 49 h1rel 268731384830.0 h2rel 0.0062630480167 r1 2 r2 1.5 lmax 3.86167e+09 default
unlocked
357 ic_hex_set_mesh 117 101 n 49 h1rel 695901183020.0 h2rel 0.0062630480167 r1 2 r2 1.5 lmax 1e+10 default
unlocked
358 ic_hex_set_mesh 256 257 n 49 h1rel 695901183020.0 h2rel 0.0062630480167 r1 2 r2 1.5 lmax 1e+10 default
unlocked
359 ic_hex_set_mesh 266 267 n 49 h1rel 695901183020.0 h2rel 0.0062630480167 r1 2 r2 1.5 lmax 1e+10 default
unlocked

```

Figure D.5: Mesh Replay Script - Continuation

```

360 ic_hex_set_mesh 121 105 n 49 hlrel 695901183020.0 h2rel 0.0062630480167 r1 2 r2 1.5 lmax 1e+10 default
    unlocked
361 ic_hex_set_mesh 170 171 n 49 hlrel 695898318027.0 h2rel 0.00287376376841 r1 2 r2 1.5 lmax 1.69508e+10
    default unlocked
362 ic_hex_set_mesh 178 179 n 49 hlrel 695898318027.0 h2rel 0.00287376376841 r1 2 r2 1.5 lmax 1.69508e+10
    default unlocked
363 ic_hex_set_mesh 201 258 n 28 hlrel 0.0 h2rel 0.00696855183124 r1 2 r2 1.5 lmax 0 default unlocked
364 ic_hex_set_mesh 101 257 n 28 hlrel 0.0 h2rel 0.00696855183124 r1 2 r2 1.5 lmax 0 default unlocked
365 ic_hex_set_mesh 202 268 n 28 hlrel 0.0 h2rel 0.00696855183124 r1 2 r2 1.5 lmax 0 default unlocked
366 ic_hex_set_mesh 105 267 n 28 hlrel 0.0 h2rel 0.00696855183124 r1 2 r2 1.5 lmax 0 default unlocked
367 ic_hex_set_mesh 378 342 n 28 hlrel 0.00459037464015 h2rel 0.0 r1 1.5 r2 2 lmax 0 default unlocked
368 ic_hex_set_mesh 369 333 n 28 hlrel 0.00459037464015 h2rel 0.0 r1 1.5 r2 2 lmax 0 default unlocked
369 ic_hex_set_mesh 368 332 n 28 hlrel 0.00459037464015 h2rel 0.0 r1 1.5 r2 2 lmax 0 default unlocked
370 ic_hex_set_mesh 377 341 n 28 hlrel 0.00459037464015 h2rel 0.0 r1 1.5 r2 2 lmax 0 default unlocked
371 mess " -- Mesh Refinement complete \n";
372
373 mess "Meshing Complete \n";
374
375
376 # Hex Export:
377
378 ic_hex_create_mesh SYSTEMPOINTS INLET S_R BLADE_LOW BLADE_HIGH S_SHROUD S_HUB SYM_LOW SYM_HIGH FLUID proj 2
    dim to_mesh 3
379 ic_hex_write_file (${DIR}) SYSTEMPOINTS INLET S_R BLADE_LOW BLADE_HIGH S_SHROUD S_HUB SYM_LOW SYM_HIGH FLUID
    proj 2 dim to_mesh 3 no boco
380 ic_uns_load (${DIR}) 3 0 {} 1
381 ic_uns_update_family_type visible {SYM_HIGH SYM_LOW INLET SYSTEMPOINTS BLADE_LOW FLUID ORFN S_R S_SHROUD
    BLADE_HIGH S_HUB} {!NODE !LINE_2 QUAD_4 !HEXA_8} update 0
382 ic_boco_solver
383 ic_boco_clear_icons

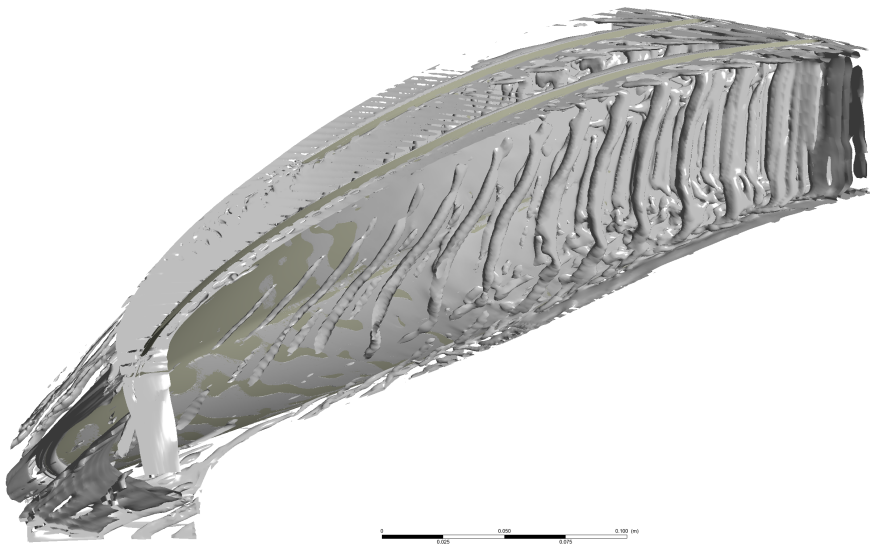
```

Figure D.6: Mesh Replay Script - Continuation



## Appendix E – Results

### E.1 Vortex Structures



**Figure E.1:** Primary and secondary vortex pairs along main blade suction side at BEP.

### E.2 Velocity Contour - Draft Tube

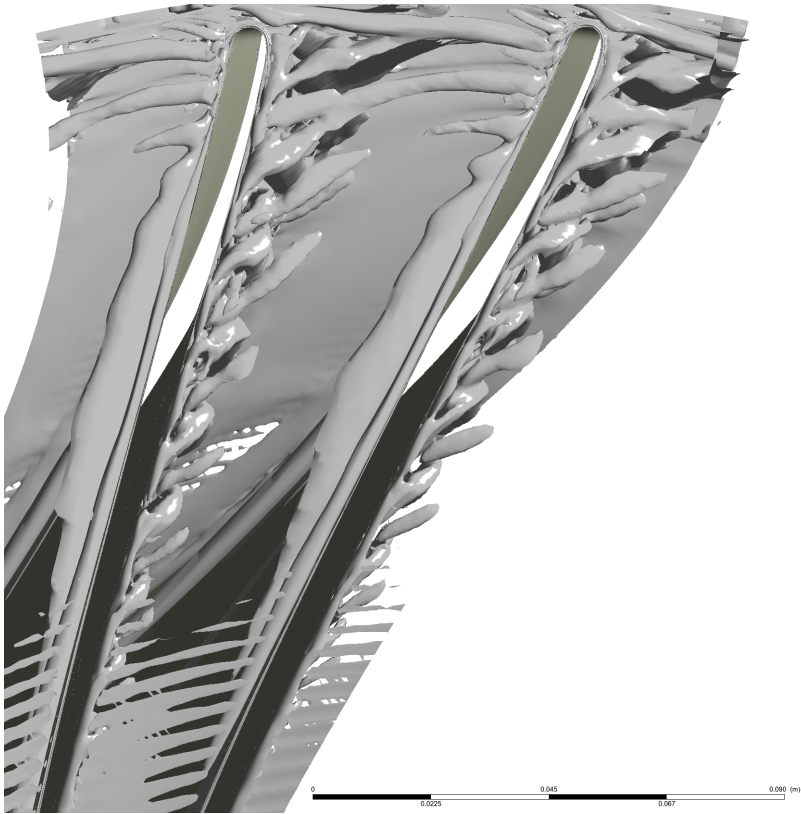


**Figure E.2:** Horizontal vortex structures between main and splitter blade, along Hub at BEP.



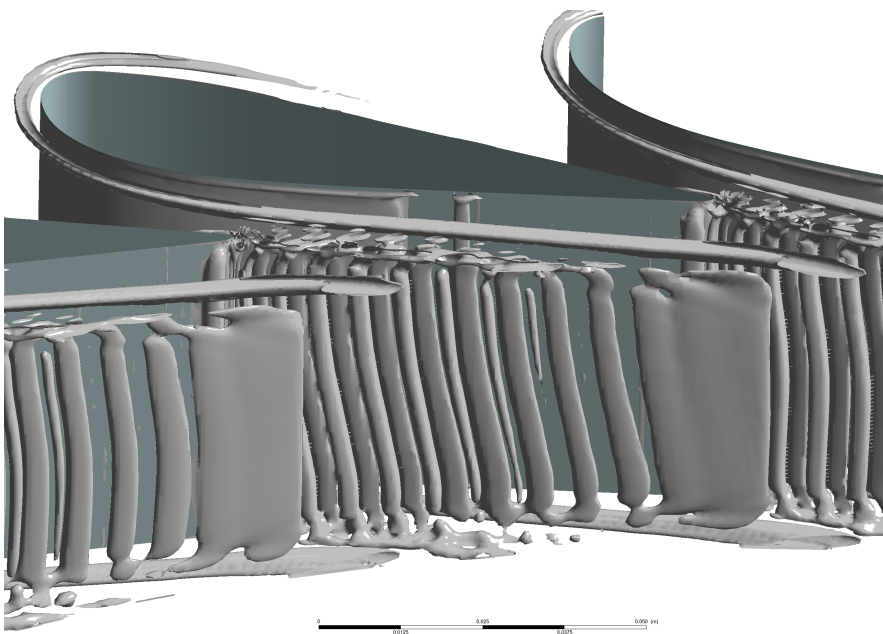


**Figure E.3:** Guide vane Passage vortex and vortex shedding at BEP.

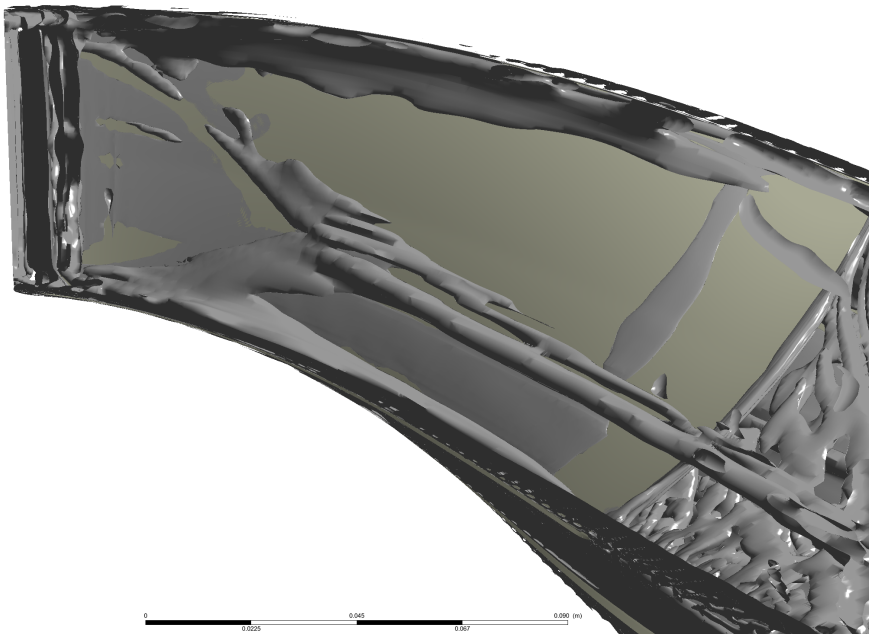


**Figure E.4:** Runner Passage vortex with near mid span merging found at PL.

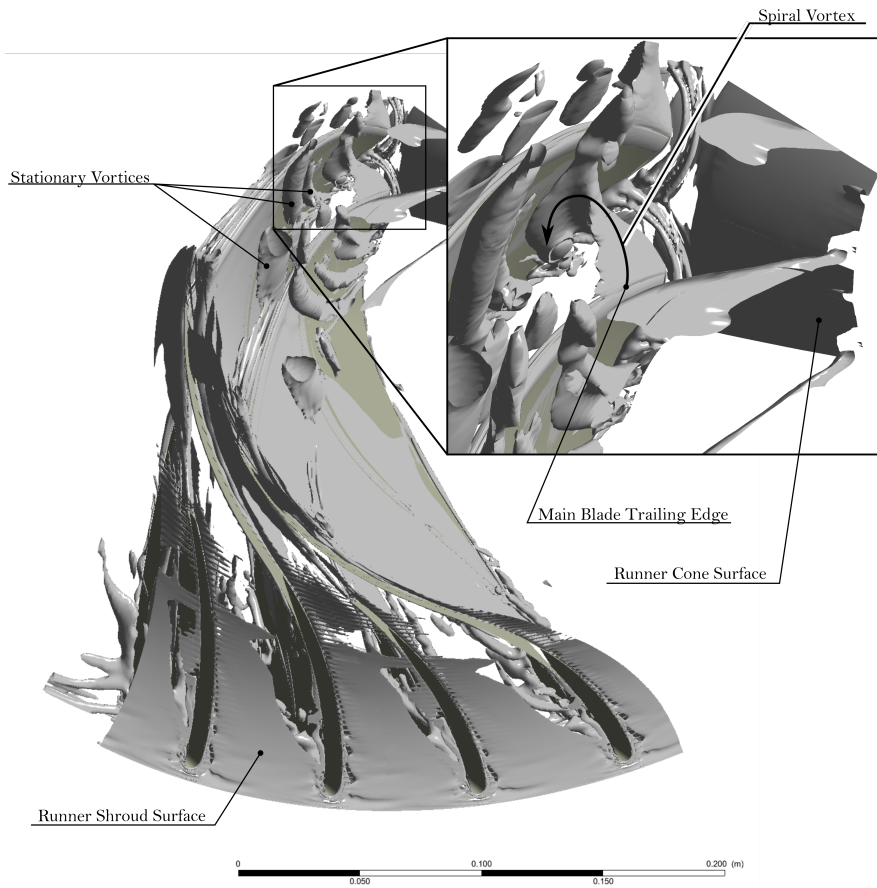


**Figure E.5:** Runner main blade spiral vortex and stationary vortices found at DPL.

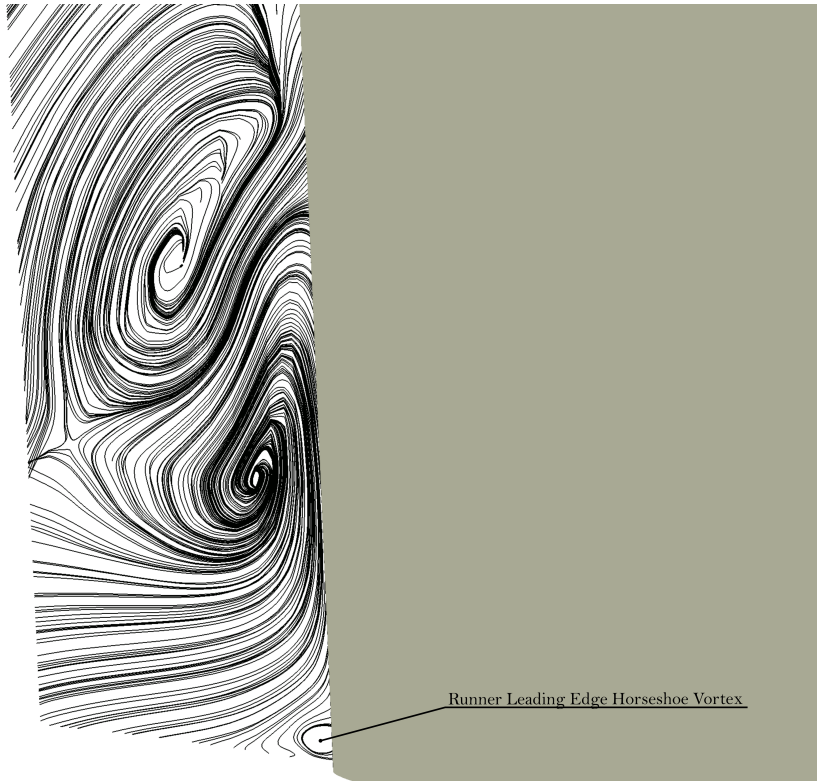


**Figure E.6:** Local vortices interacting with Horseshoe vortex at runner blades leading edge near Shroud, found at ML.

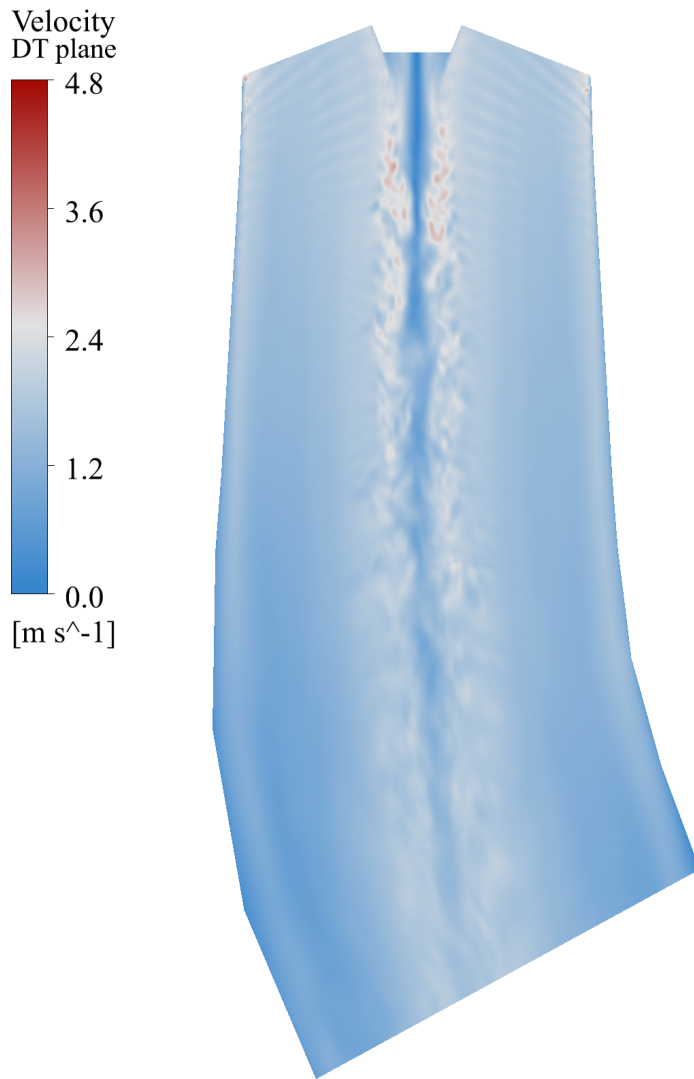


**Figure E.7:** Velocity field in draft tube after 1 second of shutdown showing vortex shedding pattern from runner blades.

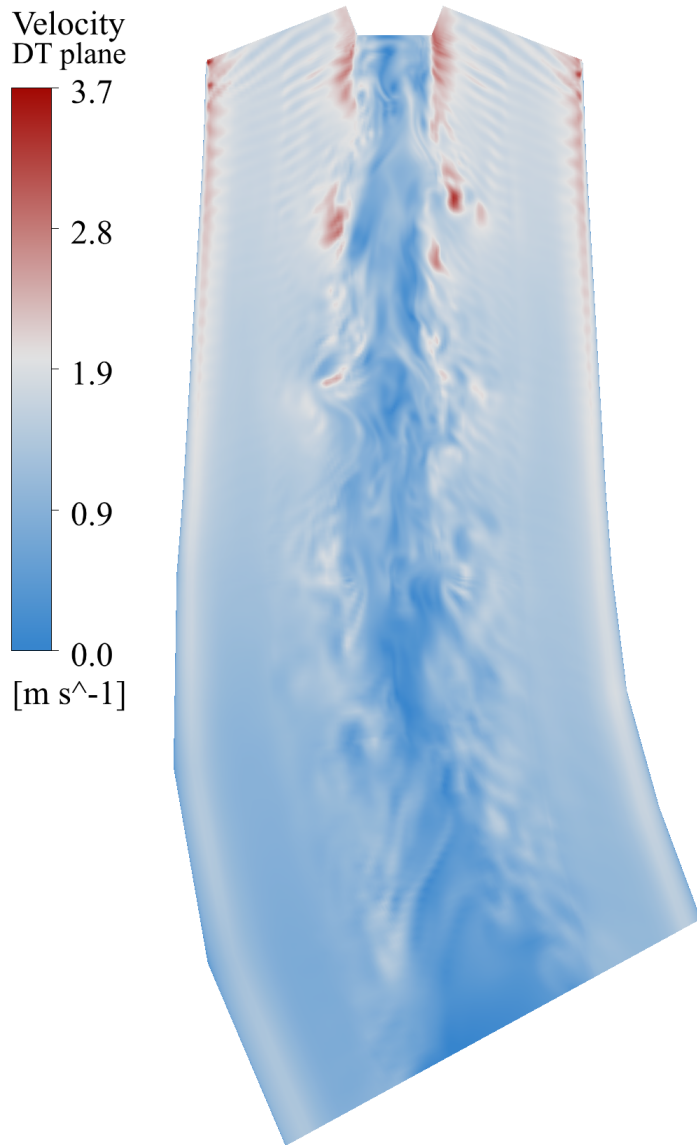


**Figure E.8:** Velocity field in draft tube after 2 second of shutdown showing vortex shedding pattern from runner blades.

---

Appendices

**Appendix F - Master agreement**

## Master`s Agreement / Main Thesis Agreement

<b>Faculty</b>	Faculty of Engineering
<b>Institute</b>	Department of Energy and Process Engineering
<b>Programme Code</b>	MIPROD
<b>Course Code</b>	TEP4925

<b>Personal Information</b>	
<b>Surname, First Name</b>	Eitzen, Fabian Camillo
<b>Date of Birth</b>	19.05.1995
<b>Email</b>	fabiance@stud.ntnu.no

<b>Supervision and Co-authors</b>	
<b>Supervisor</b>	Chirag Trivedi
<b>Co-supervisors (if applicable)</b>	
<b>Co-authors (if applicable)</b>	

<b>The Master`s thesis</b>	
<b>Starting Date</b>	15.01.2022
<b>Submission Deadline</b>	11.06.2022
<b>Thesis Working Title</b>	Investigation of a Francis turbine during start-stop
<b>Problem Description</b>	<p>1. Continue on numerical modelling of Francis turbine with accurate verification and validation. 2. Read literature thoroughly on flow field in Francis turbines, specifically, flow in blade channel, secondary flow, vortex dynamic, rotor stator interactions, flow separation from blade leading edge, inter-blade vortex, turbulence, length scale, eddies, vorticity, blade loading, pressure amplitudes and corresponding frequencies, no-load operation, stochastic loading, guide vane opening and closing rate, etc. 3. Create high quality mesh in the selected Francis turbine. Perform simulations with SAS-SST initially then LES. Improve numerical model based on results of SAS-SST and prepare for high quality LES. Carry out proper verification using (1) Celik, et al. (2005), Index of resolution quality for large eddy simulations. Journal of Fluids Engineering. (2) Pope, S. B. (2004), Ten questions concerning the large-eddy simulation of turbulent flows. New Journal of Physics. (3) Chaouat, B. (2017), The state of the art of hybrid RANS/LES modeling for the simulation of turbulent flows. Flow,</p>



	<p><b>Turbulence and Combustion. (4) Menter et al. (2021), An overview of hybrid RANS-LES models developed for industrial CFD. Applied Sciences. 4. Investigate flow field with specific emphasize on blade loading, rotor stator interaction, vorticity, pressure amplitudes, frequencies, stochastic loading using one selected rate of guide vane closing. 5. Combine all research results and, if time available, aim to write a research article for the possible submission in a selected academic journal. Deliver the master thesis before the deadline in Spring 2022.</b></p>
--	---

Risk Assessment and Data Management	
<b>Will you conduct a Risk Assessment?</b>	No
<b>If “Yes”, Is the Risk Assessment Conducted?</b>	No
<b>Will you Apply for Data Management? (REK*, NSD**)</b>	No
<b>Will You Write a Confidentiality Agreement?</b>	No
<b>If “Yes”, Is the Confidentiality Agreement Conducted?</b>	No

\* REK -- <https://rekportalen.no/>

\*\* Norwegian Centre for Research Data (<https://nsd.no/nsd/english/index.html> )

Topics to be included in the Master`s Degree (if applicable)

## Guidelines – Rights and Obligations

### Purpose

The Master's Agreement/ Main Thesis Agreement is an agreement between the student, supervisor, and department. The agreement regulates supervision conditions, scope, nature, and responsibilities concerning the thesis.

The study programme and the thesis are regulated by the Universities and University Colleges Act, NTNU's study regulations, and the current curriculum for the study programme.

### Supervision

#### The student is responsible for

- Arranging the supervision within the framework provided by the agreement.
- Preparing a plan of progress in cooperation with the supervisor, including a supervision schedule.
- Keeping track of the counselling hours.
- Providing the supervisor with the necessary written material in a timely manner before the supervision.
- Keeping the institute and supervisor informed of any delays.
- Adding fellow student(s) to the agreement, if the thesis has more than one author.

#### The supervisor is responsible for

- Clarifying expectations and how the supervision should take place.
- Ensuring that any necessary approvals are acquired (REC, ethics, privacy).
- Advising on the demarcation of the topic and the thesis statement to ensure that the work is feasible within agreed upon time frame.
- Discussing and evaluating hypotheses and methods.
- Advising on literature, source material, data, documentation, and resource requirements.
- Discussing the layout of the thesis with the student (disposition, linguistic form, etcetera).
- Discussing the results and the interpretation of them.
- Staying informed about the work progress and assist the student if necessary.
- Together with the student, keeping track of supervision hours spent.

#### The institute is responsible for

- Ensuring that the agreement is entered into.
- Find and appoint supervisor(s).
- Enter into an agreement with another department / faculty / institution if there is an external co-supervisor.
- In cooperation with the supervisor, keep an overview of the student's progress, the number of supervision hours spent, and assist if the student is delayed by appointment.
- Appoint a new supervisor and arrange for a new agreement if:
  - The supervisor will be absent due to research term, illness, travel, etcetera.
  - The student or supervisor requests to terminate the agreement due to lack of adherence from either party.
  - Other circumstances where it is appropriate with a new supervisor.
- Notify the student when the agreement terminates.
- Inform supervisors about the responsibility for safeguarding ethical issues, privacy and guidance ethics
- Should the cooperation between student and supervisor become problematic, either party may apply to the department to be freed from the agreement. In such occurrence, the department must appoint a new supervisor

*This Master's agreement must be signed when the guidelines have been reviewed.*

## Signatures

Fabian Camillo Eitzen  
**Student**

14.01.2022  
*Digitally approved*

Chirag Trivedi  
**Supervisor**

14.01.2022  
*Digitally approved*

Anita Yttersian  
**Department**

25.01.2022  
*Digitally approved*

